March 2017

Synthesis of Biopolymer Materials Tailored for Biological Applications

Nathan P. Birch

SYNTHESIS OF BIOPOLYMER MATERIALS TAILORED FOR BIOLOGICAL APPLICATIONS

A Dissertation Presented

by

NATHAN P. BIRCH

Submitted to the Graduate School of the University of Massachusetts Amherst in partial fulfillment of the requirements for the degree of

DOCTOR OF PHILOSOPHY

February 2017

Chemical Engineering

SYNTHESIS OF BIOPOLYMER MATERIALS TAILORED FOR BIOLOGICAL APPLICATIONS

A Dissertation Presented

by

NATHAN P. BIRCH

Approved as to style and content by:

_____
Jessica D. Schiffman, Chair

_____
H. Henning Winter, Member

_____
Vincent M. Rotello, Member

_____
Paul L. Dubin, Member

_____
John Klier, Department Head
Chemical Engineering

ACKNOWLEDGEMENTS

Thanks to Katrina A. Rieger, Kristopher W. Kolewe, Kerianne M. Dobosz, Thomas C. DiGiovanni, and Xiangxi Meng for help with numerous aspects of this research. Thanks to Dr. Jessica D. Schiffman for her mentorship. Thanks to Elena P. Pandres and all the undergraduate researchers who helped collect these data. Thanks to Sualyneth Galarza and Dr. Sam Polio for providing animal tissues and expertise. Thanks to Dr. Paul Dubin in the Chemistry Department at UMass-Amherst for providing access to DLS and for his expertise. Thanks to Dr. H. Henning Winter and Brian Momani for their rheological expertise. Thanks to Dr. Vincent M. Rotello and Riddha Das for help with ICP-MS and nanoparticle synthesis. We acknowledge the use of facilities at the W.M. Keck Center for Electron Microscopy and the MRSEC at UMass Amherst.

ABSTRACT

SYNTHESIS OF BIOPOLYMER MATERIALS TAILORED FOR BIOLOGICAL APPLICATIONS

FEBRUARY 2017

NATHAN P. BIRCH

B.S., MICHIGAN TECHNOLOGICAL UNIVERSITY

Ph.D., UNIVERSITY OF MASSACHUSETTS – AMHERST

Directed by: Professor Jessica D. Schiffman

Biopolymers are able to address a wide variety of medical concerns from chronic wounds to stem cell cultivation to antibacterial and antifouling applications. They are non-toxic, biodegradable, and biocompatible, making them ideal candidates for creating green materials for biological applications. In this thesis, we cover the synthesis of two novel materials from the biopolymers, chitosan and pectin. Chitosan is a biocompatible antibacterial polycation and pectin is an anti-inflammatory polyanion with a strong propensity for hydrogen-bonding. The two chitosan:pectin materials, particles and hydrogels, explore some of the structures that can be created by tuning the electrostatic interactions between chitosan and pectin. Chitosan can spontaneously form polyelectrolyte complexes when mixed with a polyanion in appropriate aqueous conditions. In the first study, chitosan:pectin nanoparticles were synthesized using an aqueous spontaneous ionic gelation method. A number of parameters, polymer concentration, addition order, mass ratio, and solution pH, were then explored and their

effect on nanoparticle formation was determined. The synthesis of chitosan:pectin hydrogels have previously been limited by harsh acidic synthesis conditions, which restricted their use in biomedical applications. In the second study, a zero-acid hydrogel has been synthesized from a mixture of chitosan and pectin at biologically compatible conditions. We demonstrated that salt could be used to suppress long-range electrostatic interactions to generate a thermoreversible biopolymer hydrogel that has temperature-sensitive gelation. We then characterized the hydrogel system's suitability for use as a wound dressing.

An additional theme throughout this work includes using shear rheology as a powerful characterization tool to improve synthesized systems and collect important structural data for the creation of synthetic analogs. An electrospun emulsion system was tuned to maximize the amount of oil that could be spun into defect-free chitosan-based fibers. The Young's modulus and complex viscosity of porcine bone marrow, porcine lung, porcine brain, and muscine brain were determined to enable the development of hydrogels that mimic these characteristics. We also explored the effects of using antifouling dopamine as a crosslinking agent for a poly(ethylene glycol) hydrogel system. Finally, with the goal of returning to green syntheses, we produced a simple self-assembling system for adding antibacterial activity to alkyd paints. Divalent metal naphthenates were used to catalyze oxidative crosslinking that form entrained metal nanoparticles as a byproduct. Overall, we have used a combination of rheology, knowledge of biopolymer interactions, and a desire to make syntheses cheaper and less hazardous to create an array of green biopolymer materials that are tailored for biological applications.

TABLE OF CONTENTS

Page

LIST OF TABLES

LIST OF FIGURES

Figure Page

LIST OF EQUATIONS

LIST OF ABBREVIATIONS

^{1}H-NMR	proton nuclear magnetic resonance
a	transition width
Å	Angstrom
AA	acetic acid
ACS	American Chemical Society
ANOVA	annalysis of variance
BSA	bovine serum albumin
C_e	chain entanglement concentration
C_{eq}	equilibrium concentration
CIN	cinnamaldehyde
COX-2	cyclooxygnase-2
CS	chitosan
CS LMW	low mollecular weight chitosan
CS MMW	medium mollecular weight chitosan
DA	degree of acetylation
Da	Daltons
DCl	deuterium chloride
DE	degree of esterification
DI	deionized
DLS	dynamic light scattering
DN	double-network
DS	degree of substitution
E^{eff}	effective Young's modulus
FTIR	Fourier transform infrared spectroscopy
G'	storage modulus
G"	loss modulus
GFP	green fluorescent protein
H-CIN	hydrocinnamic alchohol
HCl	hydrochloric acid
hTERT	telomerasse modified
ICP-MS	inductively coupled plasma mass spectrometry
IMP	intramedulliary pressure
iNOS	cytokine-inducible nitric oxide synthase
ISA	ionic strength adjuster
k	rate constant
kDa	kilodalton
kPa	kiloPascals
LB	Luria-Bertani broth
mf	mass (final)
MHB	Mueller Hinton broth

mi	mass (initial)
MIC	minimum inhibitory concentrations
MIC	minimum inhibitory concentration
MOD-MMW CS	modified meduim mollecular weight chitosan
MSC	marrow-derrived stem cells
MW	mollecular weight
n	viscoelastic exponent/power law index
NaOH	sodium hydroxide
NMR	nuclear magnetic resonance
NP	nanoparticle
NP	nanoparticle
ns	not significant
p:o	polymer to oil
Pa	Pascals
PBS	phosphate buffered saline
PDA	polydopamine
PEC	poly electrolyte complexes
Pec	pectin
PEG	poly(ethylene glycol)
PEGDMA	poly(ethylene glycol) dimethacrylate
PEO	poly(ethylene oxide)
PI	propidium iodide
pKa	acid dissociation constant
PMPC	poly(2-methacryloyloxyethyl phosphorylcholine)
PTA	phosphotungstic acid hydrate
Q	equilibrium swelling rate:dry polymer weight
RG-I	rhamnogalacturonan I
S	hydrogel strength parameter
SAOS	small amplitude oscillatory shear
SEM	scanning electron microscope
TEM	transmission electron microscopy
TPP	tripolyphosphate
TSB	tryptic soy broth
α	power law
η	apparent viscosity
η^*	complex viscosity
η_0	sero shear viscosity
η_∞	infinite viscosity
λ	relaxation time
ν	Poisson's ratio

CHAPTER 1

INTRODUCTION

1.1 Motivation

1.1.1 Chronic wounds are a serious problem

Chronic wounds are a serious problem in the medical community and diabetes is among the most common causes for these "non-healing" wounds. Currently, 25.8 million U.S. patients suffer from diabetes, while another 79 million individuals are at risk for developing the disease.[1] When the disease allows bacterial biofilms to form[2] or causes metabolic dysregulation in patients[3,4] their wounds can fail to heal.[3,4] These wounds remain perpetually arrested in the inflammatory phase of the healing process.[5,6] As a result, 100,000 diabetic patients undergo limb amputation each year in the U.S. alone.[2] New treatment strategies are needed that can neutralize existing bacterial biofilms, while also addressing metabolic dysregulation, which leads to the chronic inflammation and prevents healing. New materials are desperately needed to address this problem.

1.1.2 Biopolymers as a potent solution

Biopolymers, like chitosan and pectin, are nontoxic, biodegradable, and biocompatible.[7–15] Not only do these polymers safely breakdown in landfill, but they lack the antagonistic immune response that is so common among synthetic polymers. Their biocompatibility makes them potentially ideal for wound dressings.

1.2 Charged and biocompatible materials

1.2.1 Working with charged materials

All of the biopolymers used throughout this work are polyelectrolytes. Polyelectrolytes are polymers with numerous ionizable groups, these polymers acquire a charge in appropriate aqueous conditions.[16] Polyelectrolytes of opposite charges can bind in tight polyelectrolyte complexes (PEC), which are highly sensitive to charge ratio, molecular weight, and concentration.[17,18] Weak polyelectrolytes are only charged within a specific pH range.[19] The charge on polyelectrolytes typically adds additional properties, for example, chitosan is antibacterial due to its positive charge.[13] Of course, not every molecule that polyelectrolytes can complex with is another polyelectrolyte.

The charged nature of polyelectrolytes also enables them to bind to small molecules with charges. The most common charged small molecule encountered is a metal ion, the binding between a polyelectrolyte and a metal ion is a form of chelation.[20] These ions can provide strong antibacterial activity to a polyelectrolyte system.[21–25] These ions can also cause problems in systems meant to be biocompatible as certain ions can be toxic.[24] We will use charged additives in our systems when appropriate and to great effect, but we will also demonstrate when we can go without them for improved biocompatibility.

1.2.2 Chitosan

Chitosan (CS) is a weak polycation derived from chitin.[11,12] Chitosan is composed of *D*-glucosamine and N-acetyl-*D*-glucosamine. The amine groups provided by *D*-glucosamine become positively charged at pH's below 6.5 and enable the polymer to kill

bacteria.[11,12,26] The polyelectrolyte binds to and subsequently disrupts bacterial membranes.[13] Chitosan's key limitation is only being soluble in water when the pH is below 6.5.[11,12] Despite the limited solubility, chitosan is a powerful and useful polycation, expecially in the wound healing field.

1.2.3 Pectin

Pectin (Pec) is a weak polyanion derived from plant cell walls.[27] Its structure is variable and complex but the most important component is galacturonic acid.[27] Galacturonic acid provides a negative charge in solutions with a pH higher than 3.5 and also provides an anti-inflammatory effect.[15,19] Galacturonic acid has been shown to down regulate the expression of iNOS and COX-2, two important inflammatory enzymes.[14,15] The combination of a negative charge and anti-inflammatory activity makes pectin an attractive component for a number of wound healing systems

1.2.4 Poly(ethylene oxide)

Poly(ethylene oxide) (PEO) is a common hydrophilic and biocompatible polymer that can be used to thicken or strengthen a given system.[28–30] This is a neutral charged polymer that is very well-established for use in biomedical applications. We will use PEO as both an entangling agent for electrospinning of nanofibers and as a base synthetic hydrogel that we will strengthen by the addition of polyelectrolytes.

1.3 Materials of Interest

1.3.1 Gels

Hydrogels can be very useful for recreating specific tissue environments *in vitro*, but in order to do that, accurate data on those environments must be collected. Rheology is a powerful tool that can be used on a wide variety of systems. Shear rheology data on many tissues is rather sparse, as it is easier, if less accurate, to characterize tissues via extensional rheology.[31–37] Tissues of particular interest for cell culture are bone marrow, lung, and brain tissue. By collecting data on these tissues, we will enable the synthesis of more accurate mimics.

1.3.2 Electrospun Nanofibers

The electrospinning process fabricates non-woven mats composed of continuous nano- to micro- meter scale diameter fibers.[38,39] This well-established, scalable[40] technique has been utilized to form fibers from over a 100 different polymers including, polyelectrolytes,[41,42] biopolymers,[43–45] and synthetic polymers.[46,47] Additionally, researchers have further tailored the functionality of fibers by loading solid agents into the polymer precursor solutions, including TiO_2/graphene for increased electrical performance,[48] quantum dots for fluorescent detection,[49] and single-walled carbon nanotubes for antibacterial activity.[50] In these cases, the solid agent was suspended in a concentrated polymer solution, which provided the chain entanglement necessary to "carry" the solid agent along the electrospinning process.[44] Alternatively, researchers have synthesized nanoparticles within a fiber mat post-electrospinning, thus avoiding the need to optimize precursor rheology.[51,52] However, much less research has been

conducted on electrospinning nanofibers from polymer solutions that contain immiscible phase liquids.[53–61] A handful of reports used harsh organic solvents to emulsion electrospin fibers, by relying on a surfactant to carry the immiscible phase biological cargo ─ proteins,[58,62] DNA,[63] and water-soluble drugs[54,64] ─ and protect them against coalescence.[53–59] Electrospun systems are potent platforms for biologically active polyelectrolytes.

1.3.3 Nanoparticles

The large surface area per unit volume provided by nanoparticles makes them an ideal platform for antibacterial applications. Metallic nanoparticles, especially copper[22] and silver,[23–25] are long lasting antibacterial agents. These particles are toxic to people as well as bacteria, limiting them to roles were direct contact is limited.[24] Polymer-based nanoparticles, like chitosan-copper and cross-linked chitosan nanoparticles are more biologically friendly options, but tend to have a shorter lifespan than their metal counterparts.[20,65–68] By playing to their strengths we will utilize both types of nanoparticle for different antibacterial applications.

CHAPTER 2

DISSERTATION OBJECTIVES

Over the past 5 years we have synthesized a wide area of biopolymer systems for different biological applications. The initial focus of this research was on chitosan:pectin systems for the treatment of chronic wounds. We synthesized CS:Pec nanoparticles without relying on a metal core or calcium chloride. We developed a method for producing a CS:Pec hydrogel that was thermoreversible without the use of harsh acids. We performed a rheological study on the impact of cinnamaldehyde on CS:poly(ethylene oxide) entanglement in order to improve our labs ability to electrospin the system. A wide array of animal tissues were characterized to provide a data basis for constructing synthetic analogs. A polyethylene glycol dimethacrylate hydrogel system was developed by our lab and the effects of polydopamine crosslinking were explored. Alkyd based paint was used to self-assemble metal naphthenates into antibacterial nanoparticles. All together this research provides a large toolbox of materials for a number of biological applications that we will discuss in depth.

The specific objectives for each project are laid out in the following sections of this chapter. Subsequent chapters provide detailed methods, results, discussion, conclusion and future work for each objective. In each objective below, the specific subsequent chapter containing the work relevant to that objective is stated.

In our first study (Chapter 3), chitosan:pectin (CS:Pec) nanoparticles were synthesized using an aqueous spontaneous ionic gelation method. A number of

parameters - polymer concentration, addition order, mass ratio, and solution pH - were explored and their effect on nanoparticle formation was determined. The size and surface charge of the particles were characterized, as well as their morphology using transmission electron microscopy (TEM). The effect of polymer concentration and addition order on the nanoparticles was found to be similar to that of other chitosan:polyanion complexes. The mass ratio was tuned to create nanoparticles with a chitosan shell and a controllable positive zeta potential. The particles were stable in a pH range from 3.5 to 6.0 and lost stability after 14 days of storage in aqueous media. Due to the high positive surface charge of the particles, the innate properties of the polysaccharides used, and the harmless disassociation of the polyelectrolytes, we suggest that the development of these CS:Pec nanoparticles offers great promise as a chronic wound healing platform.

Previous synthesis of CS:Pec hydrogels has previously been limited by harsh acidic synthesis conditions, which further restricted their use in biomedical applications. We synthesized a zero-acid hydrogel from a mixture of chitosan and pectin at biologically compatible conditions (Chapter 4). We demonstrated that salt could be used to suppress long-range electrostatic interactions to generate a thermoreversible biopolymer hydrogel that has temperature-sensitive gelation. Rheology determined that both the hydrogel and the solution phases are highly elastic, with a power law index of close to −1. When dried hydrogels were placed into phosphate buffered saline solution, they rapidly rehydrated and swelled to incorporate 2.7× their weight. We also removed the salt from our CS:Pec hydrogels, thus, creating thick and easy to cast polyelectrolyte complex hydrogels, which proved to be compatible with human marrow-derived stem

cells. We suggest that our development of an acid-free CS:Pec hydrogel system that has excellent exudate uptake holds potential for wound healing bandages.

Electrospinning hydrophilic nanofiber mats that deliver hydrophobic agents would enable the development of new therapeutic wound dressings. However, the correlation between precursor solution properties and nanofiber morphology for polymer solution electrospun with or without hydrophobic oils had not yet been demonstrated. Cinnamaldehyde (CIN) and hydrocinnamic alcohol (H-CIN) were electrospun in chitosan (CS)/poly(ethylene oxide) (PEO) nanofiber mats as a function of CS molecular weight and degree of acetylation (DA) (Chapter 5). Viscosity stress sweeps determined how the oils affected solution viscosity and chain entanglement (C_e) concentration. The maximum polymer:oil mass ratio able to be electrospun was 1:3 and 1:6 for CS/PEO:CIN and :H-CIN, respectively. A higher DA for chitosan increased the incorporation of H-CIN, but not CIN. The correlations determined for electrospinning plant-derived oils could potentially be applied to other hydrophobic molecules, thus broadening the delivery of therapeutics from electrospun nanofiber mats

Creating a hydrogel with specific properties is relatively easy, but using those gels as a synthetic model for tissue requires data that is often lacking. We explored a range of porcine and muscine tissues in a group of experiments (Chapter 6). We were the first group to explore the mechanics of intact bone marrow,[35,36,69–73] the first group to explore the shear mechanics of porcine lung tissue,[31] and one of the first groups to explore the mechanics of intact brain tissue (muscine and porcine).[32] We found that porcine bone marrow tissue was a benign elastic solid with a Young's modulus of 0.73-135.6 kPa. Bone marrow has high inter-sample variability. The Young's modulus for porcine lung

tissue was found to be 3000 ± 72 Pa with inter-sample variability being much lower than that of porcine bone marrow tissue. Muscine brain tissue was found to be softer with a Young's modulus of 979 ± 786 Pa, the inter-sample variability was on par with the bone marrow samples. Porcine brain tissue was slightly softer than muscine brain tissue with a Young's modulus of 693 ± 374 Pa and a similar level of inter-sample heterogeneity to the muscine brain tissue. Having a good understanding of these data will enable future researchers to synthesize hydrogel tissue mimics to reproduce the conditions in any of these tissues.

It has been shown that a soft surface that expresses ionic surface chemistry should resist bacterial adhesion most effectively. We seek to develop such a surface that is stiff and tough enough to be used in a medical catheter. Poly(ethylene glycol) dimethacrylate (PEGDMA) hydrogels were found to have strong frequency independent elastic moduli (Chapter 7). Their viscous moduli were much weaker and strongly frequency dependent. The gels were also found to be stiffer at higher polymer concentrations. The addition of poly(2-methacryloyloxyethyl phosphorylcholine) (PMPC) was found to increase both moduli in concentrated systems and result in almost no change in dilute systems. PEGDMA hydrogels can easily be coated in polydopamine, which drastically improves their structural characteristics and should improve anti-fouling activity.

Our novel system for self-assembled metal nanoparticle loaded oil-based paints should provide and cheap and effective solution killing potentially harmful bacteria and preventing deleterious buildup of bacterial biofilms (Chapter 8). We found via TEM that copper nanoparticles assembled into large aggregates, while cobalt nanoparticles formed large oblong particles and iron nanoparticles formed small spheroids. Copper was shown

to readily diffuse within 7.5 days with cobalt being similar and zinc having a greater equilibrium concentration but lesser rate constant. Iron was not found to diffuse appreciably. Solution-based minimum inhibitory concentrations (MIC) for the metal salts were also obtained and it was found that zinc and cobalt were marginally more effective than cobalt and iron at killing *E. coli*. Additional work will be done on bacterial interaction with the films under shear flow to fully characterize the films potential for antifouling applications. At the end of all the characterization, we suggest that we will find a highly effective and cheap antibacterial coating.

CHAPTER 3

TUNING CS:PEC INTERACTIONS TO PRODUCE POLYELECTROLYTE COMPLEX NANOPARTICLES

Adapted from Birch, N. P.; Schiffman, J. D. Characterization of Self-Assembled Polyelectrolyte Complex Nanoparticles Formed from Chitosan and Pectin. *Langmuir* **2014**, *30* (12), 3441–3447.

3.1 Introduction

Nanoparticles have previously been formulated to treat chronic wounds. Literature has predominantly investigated metallic nanoparticles, including gold,[21] copper,[22] and silver[23–25] as promising antibacterial agents. Silver nanoparticles have historically been the leading candidate because they have a very low minimum inhibitory concentration, ~3 ug/mL for most bacteria,[23] indicative of their strong antibacterial activity. However, the use of silver is problematic because silver resistance has already been observed in *Pseudomonas aeruginosa* and the continued use of silver as an antimicrobial agent will likely lead to increased silver-resistance in other microorganisms.[74] Additionally, it has been demonstrated that metallic nanoparticles have multiple organ toxicity. As the metallic nanoparticles break down, metal ions are released and must be chelated by the body, resulting in innate toxicity.[24] We suggest that alternative antibacterial nanoparticle treatments be explored. These particles should avoid the spreading of resistance genes, toxic components, and harsh solvents, while offering a patient good biocompatibility and additional functional benefits.

Chitosan, a polycationic derivative of chitin, is nontoxic, antibacterial, biodegradable, and biocompatible.[11,12] Chitosan is composed of 1,4 linked 2-amino-2-deoxy-β-*D*-glucan and 1,4 linked 2-acetamido-2-deoxy-β-*D*-glucan, **Figure 1a**. The degree of acetylation can be defined as the percentage of 2-acetamido-2-deoxy-β-D-glucan present in the polymer chain and determines the number of charges present on the polymer chain.[75] Due to the high positive charge density of chitosan, it is intrinsically antimicrobial. The polyelectrolyte binds to and subsequently disrupts bacterial membranes.[13] One challenge of working with chitosan is that its solubility is limited to mildly acidic aqueous solutions because it has a pKa of 6.5.[26]

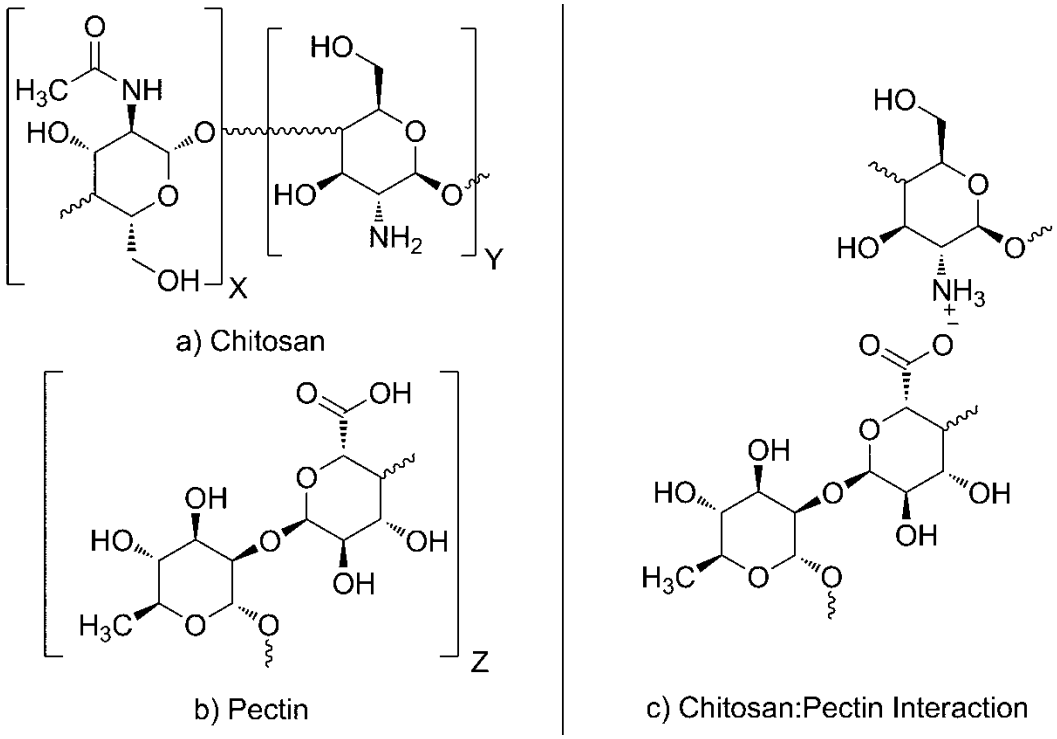

Figure 1: The chemical structure of chitosan:pectin interactions. The chemical structure of (a) the polycation chitosan includes 2-acetamido-2-deoxy-β-D-glucan (X) residues and 2-amino-2-deoxy-β-D-glucan (Y) residues. (b) The chemical structure of the

rhamnogalacturonan I (RG-I) region of the polyanion pectin is also provided. In this study, we have bound chitosan to pectin via (c) the proposed method of electrostatic interactions between 2-amino-2-deoxy-β-D-glucan and the RG-I region of pectin

The antibacterial activity of chitosan-metallic and chitosan nanoparticles formed by ionic gelation have been widely explored.[20,65–68] For example, antibacterial silver, gold, and copper[20,22,66–68] nanoparticles have been capped with chitosan in an attempt to improve their biocompatibility and decrease their toxicity.[20,22] However, this did not avoid the innate toxicity of the dissolved metal ions.[76] Chitosan nanoparticles prepared by the ionic gelation of chitosan with tripolyphosphate (TPP) anions have also demonstrated a high antibacterial activity by virtue of their large positive surface charge. For example, antibacterial "snowflake" shaped particles had a surface charge of 51 mV as determined by zeta potential measurements.[20] However, in this work, the TPP did not provide any additional function to the patient. We aim to develop a system that pairs chitosan with a second active agent, thus circumventing the innate toxicity of metallic nanoparticles and maximizing the functionality of the particles by replacing inactive components with active compounds. Polycations, including chitosan, can spontaneously form polyelectrolyte complexes (PECs) when mixed with polyanions in appropriate aqueous conditions. At nonstoichiometric ratios, weak polyelectrolytes of significantly different molecular weights have long been known to produce soluble PECs.[18] The size of these complexes has been shown to be influenced by the polymer concentration, mixing ratio, charge density, and the presence of low molecular weight ions.[17] The requirement of at least two different polymers opens up the opportunity for us to form chitosan complexes with an additional functional polyanion, rather than relying on a crosslinking anionic salt,

i.e., TPP.[20,77] However, with the exception of heparin,[17] previous investigations[17,18,77,78] into chitosan:polyanion PECs have only relied on the polyanion for their relatively low molecular weight and/or high negative charge ─ properties that facilitate nanoparticle formation.[18,17]

Pectin, our polyanion, is a class of complex hetero-polysaccharides derived from plant cell walls,[27] consisting primarily of 1,4 linked α-*D*-galactopyranosyluronic acid residues with 1,2-linked α-*L*-rhamnopyranose residues interspersed with varying frequency, **Figure 1b**. There is also a large amount of arabinose, galactose, and xylose. The degree of esterification controls the charge density of the pectin backbone.[27] A number of the galacturonic acid residues are methyl or acetyl esterified – the percentage of galacturonic acid residues that are esterified is known as degree of esterification (DE). Pectins are a weak polyanion with a pKa of about 3.5.[19] Pectins have innate anti-inflammatory activity due to their galacturonic acid content[14] and the presence of esterified galacturonic acid residues has been demonstrated to downregulate the expression of cox-2 and iNOS — two enzymes that have a large impact on chronic inflammation and cancer.[15] Elevated levels of iNOS have been found in chronic diabetic wounds and are suspected to play a significant role in delaying wound healing.[4] Previously, large chitosan:pectin microbeads with an average diameter of 118.0 μm have been synthesized by injecting pectin solutions into a crosslinking bath followed by a chitosan bath.[79–81] However, by reducing the size of the chitosan:pectin particles we could potentially treat chronic wounds by providing an enhanced antibacterial activity[20] along with an anti-inflammatory functionality.

In this study, we have synthesized chitosan:pectin (CS:Pec) particles at the nanoscale. Chitosan and pectin bind electrostatically to form soluble aggregates in a solution at the appropriate pH (**Figure 1c**). Systematically, the resultant nanoparticles have been characterized by exploring the effects of polymer concentration, order of addition, mass mixing ratio, storage, and solution pH. These multifunctional polycation−polyanion nanoparticles hold potential to address the multiple root causes of chronic wounds, while also offering excellent biocompatibility and a safe degradation *in vitro*. This work paves the way for biological testing beyond the scope of this work that systematically evaluates these CS:Pec nanoparticles for wound healing applications.

3.2 Experimental

3.2.1 Materials and Chemicals

Low molecular weight chitosan (CS LMW, poly(D-glucosamine)), Medium molecular weight chitosan (CS MMW, poly(D-glucosamine)), pectin from citrus peel (Pec, galacturonic acid content ≥ 74%), ReagentPlus grade acetic acid (AA, ≥99.0%), anhydrous sodium acetate (≥99.0%), deuterium chloride (DCl, ≥99.0%), sodium hexametaphosphate (65−70% P_2O_5), bovine serum albumin (BSA, ≥98.0%), and microscopy-grade phosphotungstic acid hydrate (PTA) were obtained from Sigma-Aldrich (St. Louis, MO). Certified ACS grade sodium chloride (≥99.0%), ACS-grade sodium hydroxide (NaOH, ≥98.9%) and ACS-plus-grade hydrochloric acid (HCl, 12.1 N) were obtained from Fisher Scientific (Fair Lawn, NJ). Deionized (DI) water was obtained from a Barnstead Nanopure Infinity water purification system (Thermo Fisher Scientific, Waltham, MA).

3.2.2 Characterization of Chitosan and Pectin

The intrinsic viscosities of the polymers were determined using a capillary viscometry method. Dilute solutions of CS (0.2 M sodium chloride and 0.l M AA) and Pec (1 wt% sodium hexametaphosphate) were measured at varying concentrations to obtain an intrinsic viscosity.[82] The molecular weight was determined for CS using the Mark−Houwink parameters of K = 1.8 × 10−3 cm3 g−1 and a = 0.93,30 whereas for Pec, K = 9.55 × 10^{-2} cm^3 g^{-1} and a = 0.73.[9]

The degree of acetylation of the CS was analyzed using a proton nuclear magnetic resonance (^{1}H-NMR) method outlined in Fernandez-Megia et al.,[83] which is a modified version of the method originally outlined by Hirai et al.[84] Briefly, CS was solvated in 2% DCl until the solution was clear and then allowed to cool. Spectra were recorded on an Avance 400 NMR spectrometer (Bruker, Billerica, MA) at 27 °C. The integrals of the acetyl groups and H2−H6 protons[84,85] were compared to obtain a degree of acetylation. The degree of esterification of the pectin was analyzed using a titration method outlined in the Food Chemicals Codex.[86] Pectin is titrated to an end point using 100 mM NaOH, saponified, and titrated to the end point again. The ratio of the two titers provides the ratio of esterified galacturonic acid to free galacturonic acid.

3.2.3 Preparation of LMW CS:Pec Nanoparticles

CS LMW were prepared by placing 0.05% w/v chitosan in 100 mM AA, agitated overnight at 70 °C. Pec solutions were prepared by placing 0.05% w/v pectin in DI water and agitating for 24−48 h. Once solvated, the chitosan solution was filtered through a 0.22 μm polyethersulfone filter (Millipore Tullagreen, Carrigtwohill, Co., Cork, Ireland)

and diluted with filtered DI water to the appropriate concentration. The solution was placed under agitation, and slowly the filtered 0.05% w/v pectin was added until the appropriate chitosan-to-pectin ratio was obtained. The solutions were left under agitation at room temperature (~23 °C) for 120 min prior to further testing and analysis of the LMW CS:Pec nanoparticles.

3.2.4 Characterization of LMW CS:Pec Nanoparticles

Measurement of hydrodynamic radius, zeta potential, and polydispersity of all particles were performed using a ZEN3600 Zetasizer (Malvern Instruments, Malvern, Worcestershire, U.K.). Each sample was measured at least 6 times and averages were obtained. In the case of concentration and mass ratio measurements, 3 samples were used for each data point. The morphological characteristics of the nanoparticles were observed using a JEOL 100CX transmission electron microscopy (TEM, Akishima, Tokyo, Japan). Solutions containing the nanoparticles were drop-cast onto carbon/Formvar films supported by a 200 mesh copper grid (Electron Microscopy Sciences, Hatfield, PA) and stained with 0.5% w/v PTA.

3.2.5 Statistical Analysis

Throughout Results and Discussion, results are depicted as mean ± confidence interval. The significance between mean values was determined using Welch's *t* test. Significance was interpreted as the probability below 5%.

3.3 Results and Discussion

3.3.1 Characteristics of Chitosan and Pectin

The first step in maximizing the antimicrobial activity of our particles is characterizing our starting polyelectrolytes. This will help to identify the synthesis conditions that will yield small particles with positive surface charges.[13] The viscosity-average molecular weight of the LMW CS, MMW CS, and Pec were found to be 460 kDa, 1,000 kDa, and 50 kDa, respectively. We determined via NMR that the degree of acetylation (DA) was 13% for LMW CS and 23% for MMW CS.[83–85] The degree of esterification (DE) of the citrus pectin was found to be approximately 60%, which is in good agreement with literature values.[87] The galacturonic acid content was determined to be 85%, which is above the manufacturer's specification of ≥74%. The effect of these factors on particle size and surface charge will be explored in later sections.

3.3.2 Effect of Concentration and Polymer Addition Order on CS:Pec Nanoparticle Formation

Chitosan:pectin (CS:Pec) nanoparticles were successfully synthesized as a function of polymer concentration and polymer addition order (Figure 2). While an equal chitosan-to-pectin mass ratio was maintained, the nanoparticles were synthesized at four different total polymer concentrations. In **Figure 2**, addition order indicates which polymer was added first to the solution. The chitosan was added first in the CS:Pec nanoparticles (black ■), whereas for the Pec:CS nanoparticles (red ●), the pectin was added first. The size of the resultant particles was measured using dynamic light scattering (DLS). A bimodal distribution was returned wherein the smaller peak was the

free polymer and the larger peak was the nanoparticles. **Figure 2a** displays the average value of the dominant peak, which we refer to as the intensity-averaged diameter. The CS:Pec nanoparticles increase in size from 560 ± 10 nm to 1000 ± 40 nm at total polymer concentrations of 0.10 mg/mL and 0.50 mg/mL, respectively. When the polymer addition order was reversed, the Pec:CS nanoparticles' intensity-averaged diameter increased from 460 ± 20 to 1110 ± 30 nm at total polymer concentrations of 0.10 and 0.50 mg/mL, respectively. This trend of particle size increase with increasing concentration is consistent with chitosan nanoparticles formed by crosslinking with sodium tripolyphosphate (TPP).[77] Statistically, there was a significant difference in particle size due to addition order at all concentrations, except for at a polymer concentration of 0.38 mg/mL.

A representative TEM micrograph of the nanoparticles is provided as an inset in **Figure 2b**. Two CS:Pec nanoparticles at a 1:1 mass ratio and 0.5 mg/mL polymer concentration are displayed. Measurements taken from many micrographs of nanoparticles confirm that they are approximately 500 nm in diameter with a roughly spherical morphology. This size corresponds well to the sizes we obtained through DLS when drying effects are taken into account. The sensitivity of PEC systems to concentration changes makes TEM of large populations of particles incredibly challenging. From our experiments, increased concentration significantly altered the size of the nanoparticles and yielded agglomerates of particles. Notably, this is why more attention in this work is paid to the DLS characterization.

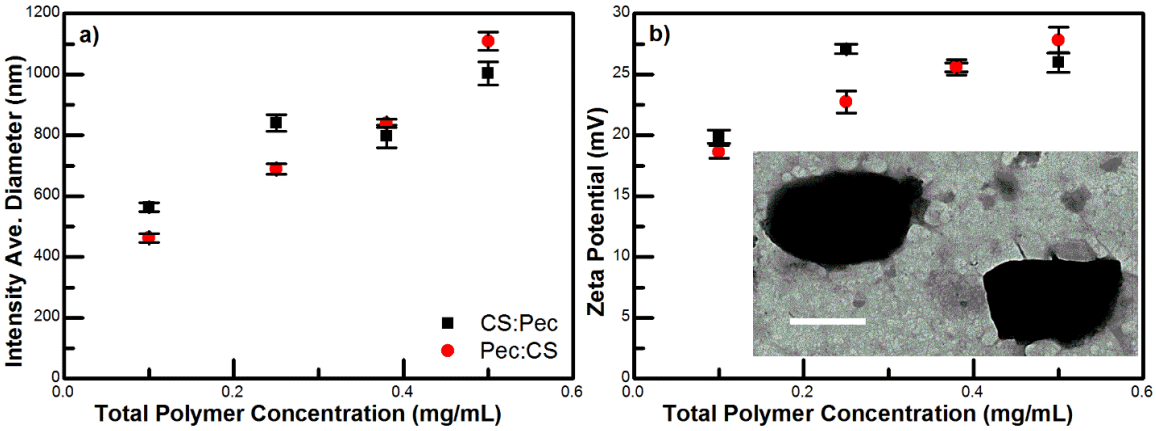

Figure 2: Polymer addition and concentration effects on particle size and charge. Displayed is the effect that polymer addition order and total polymer concentration has on (a) the intensity-averaged diameter and (b) the zeta potential of CS:Pec (black ■) and Pec:CS (red ●) nanoparticles. CS:Pec indicates that pectin was added to chitosan, whereas Pec:CS indicates that the addition order was reversed. All nanoparticles were synthesized in 35 mM acetate buffer solutions (pH of 4). (b) A representative micrograph of CS:Pec nanoparticles is provided. These specific nanoparticles were prepared at a polymer concentration of 0.5 mg/mL with an equal mass ratio. The scale bar is 500 nm.

The zeta potential of the CS:Pec nanoparticles increased from 20 ± 1 mV at 0.10 mg/mL to 26 ± 1 mV at 0.50 mg/mL (**Figure 2b**). This trend was mirrored by the Pec:CS nanoparticles, wherein the zeta potential increased from 19 ± 1 mV at 0.10 mg/mL to 28 ± 1 mV at 0.50 mg/mL. The increase in zeta potential with concentration is likely due to the fact that salt concentration relative to polymer concentration is decreasing as the polymer concentration is increased. Increasing salt concentration has been shown in chitosan:alginate systems to reduce their zeta potential through increased charge screening.[78] The high positive zeta potential suggests a structure whose surface is

dominated by chitosan.[77,78] Similar systems (alginate:chitosan[78] and chitosan:dextran sulphate[18]) have been shown to generate structures with a mixed core and a shell dominated by the polyelectrolyte in excess. No significant difference in zeta potential due to addition order was found, except at a polymer concentration of 0.25 mg/mL. A similar study conducted on chitosan:alginate nanoparticles determined that addition order significantly affected particle size, but not zeta potential.[78] Schatz et al.[18] proposed that polyelectrolyte complex nanoparticles are formed with a charge neutralized core, with excess charge units being segregated to the surface of the particles. This suggests that the differences due to addition order result because the polyelectrolyte added second has to diffuse into a core of the oppositely charged polyelectrolyte.

3.3.3 Impact of Mass Ratio on LMW CS:Pec Nanoparticle Formation

The mass ratio of polycation to polyanion is an important factor in polyelectrolyte complexation and impacts the size and surface charge of the particles.[18,78] **Figure 3a** displays the effect that the mass ratio of chitosan-to-pectin (CS:Pec 1:2, 2:3, 1:1, 3:2, 2:1, and 3:1) has on their Z-average diameter. Z-average diameter is an intensity-averaged measure of the hydrodynamic radius as determined from the cumulants function fit by software to DLS data. Statistically, the average diameter of the particles remain the same with increasing chitosan content for the five CS:Pec nanoparticle formulations. The CS:Pec ratios (1:2, 2:3, 1:1, 3:2, and 2:1) yielded particles with an average diameter of 540 ± 20 nm, 560 ± 30 nm, 600 ± 50 nm, 600 ± 20 nm, and 590 ± 30 nm, respectively. These particles are similar in size to the chitosan:heparin and chitosan:hyaluronic acid nanoparticles found in literature, which were produced from a chitosan of similar molecular weight at various polyelectrolyte ratios.[17] CS:Pec ratios lower than 1:2 produce

cloudy solutions with aggregates above 6 μm, which are too large to measure using DLS. The 1:2 mass ratio nanoparticles are slightly above where negative charges begin to dominate the stoichiometric ratio of positive to negative charges. This ratio can be calculated from the mass ratios, molecular weight of residues, purity, galacturonic acid content, DA, and DE. Our only particles that had a statistically different average diameter, were the large, 730 ± 60 nm CS:Pec nanoparticles that were formed from a 3:1 ratio. CS:Pec ratios higher than 3:1 lacked sufficient pectin to complex with the chitosan to form stable particles.

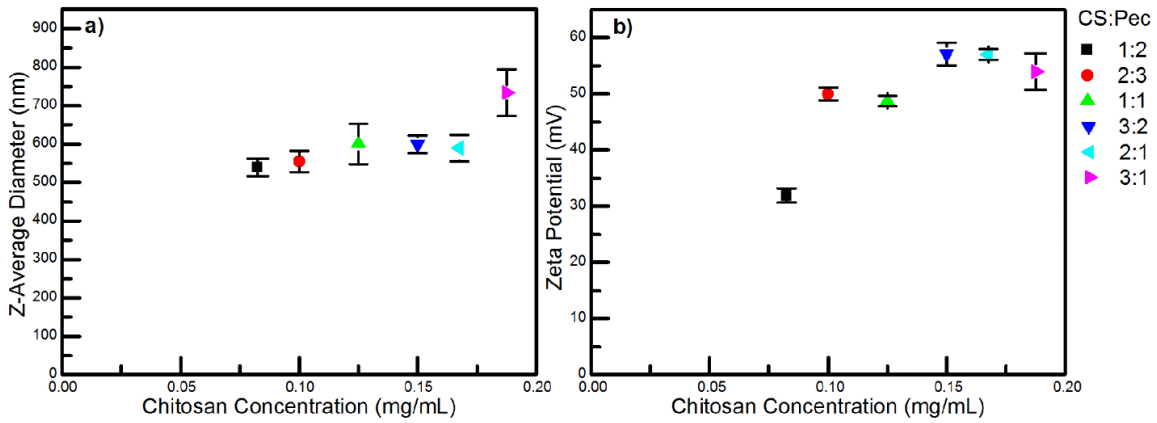

Figure 3: Mass ratio effects on particle size and charge. Displayed is the effect that altering the mass ratio of chitosan to pectin has on the (a) Z-average diameter and (b) zeta potential of the CS:Pec nanoparticles. Six chitosan to pectin ratios, 1:2, 2:3, 1:1, 3:2, 2:1, and 3:1, were explored by holding the total polymer concentration constant at 0.05% w/v in 50 mM AA.

The zeta potential of the particles correlates strongly with their mass ratio (**Figure 3b**). The particles with a 1:2 CS:Pec mass ratio had the lowest zeta potential, ~ 30 mV.

This is likely due to the increased anionic charges of pectin, as well as increased complexation between pectin and chitosan, which leaves fewer positive charges on the surface of the particles. The 2:3 and 1:1 CS:Pec mass ratio particles had statistically equivalent zeta potentials, 50 ± 1 mV and 49 ± 1 mV, respectively. A significantly higher zeta potential was determined for the particles with a 3:2 and 2:1 CS:Pec mass ratio, 57 ± 2 mV and 57 ± 1 mV, respectively. Zeta potential measurements for 3:1 CS:Pec nanoparticles had the highest margin of error, with a zeta potential of 54 ± 3 mV. We suggest that this was due to the increased variability in particle size (**Figure 3a**), as well as the free chitosan present in the solution.

3.3.4 Stability of CS:Pec Nanoparticles at Room Temperature

To evaluate the stability of the CS:Pec nanoparticles for room temperature storage (T = 22 °C), particles were stored and sampled as a function of time over a 30 day period (**Figure 4**). In general, the intensity-averaged diameter of the samples decreased over time. The general trend of this data shows that nanoparticles at all mass ratios have a similar stability. Measurements were acquired for each sample until the level of aggregation reached a threshold where the CS:Pec nanoparticle solution was too polydisperse to accurately measure via DLS. All samples were unsuitable for measurement after 30 days. Previous chitosan-based nanoparticle systems with TPP, hyaluronic acid, or alginate have been found to be stable over a 30 day period.[78,88,89] Therefore, we suggest that a mechanism unique to pectin might be responsible for the instability of these particles. It has been well established[90] that pectin can undergo acid hydrolysis at a pH of 4.0 or lower, with more acidic environments yielding faster hydrolysis. We hypothesize that this is the root cause of the particles' instability.

Lowering the storage temperature or lyophilization could further increase the stable lifespan of our CS:Pec particles.[78,91]

In general, the zeta potential of the samples decreased over the 30 day period (**Figure 4b**). The equal mass ratio particles decreased from 48 ± 1 mV at initial synthesis to 26 ± 1 mV at 15 days and 17 ± 1 mV at 27 days. Previous studies determined that polyelectrolyte complex nanoparticles with zeta potential below 30 mV are especially prone to aggregation.[17,92] Using this as a metric, most of our particles lost stability after about 14 days of storage. After crossing this threshold, the majority of the samples contain aggregates too large and polydisperse to accurately measure using DLS.

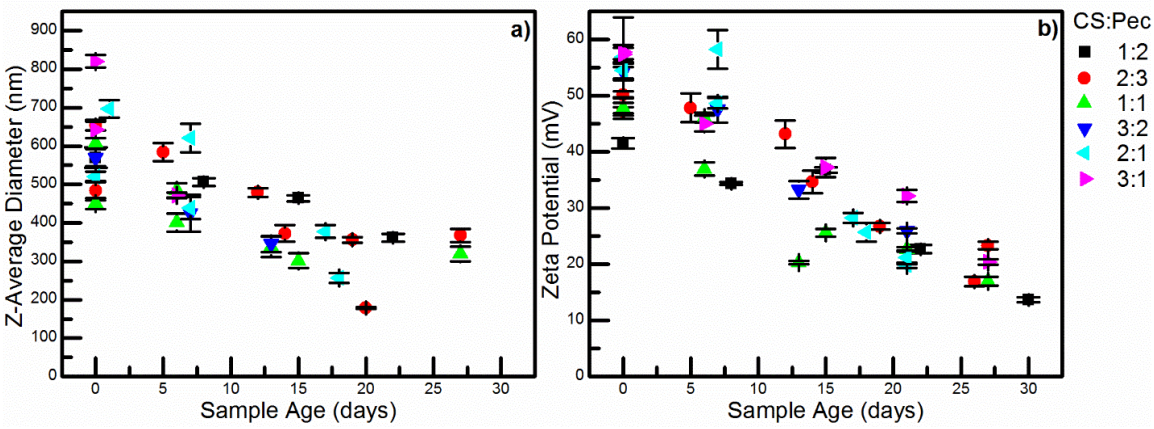

Figure 4: CS:Pec NP stability over 30 days. The stability of CS:Pec nanoparticles formed at various mass ratios was investigated over a 30 day period. The (a) Z-average diameter and (b) zeta potential of CS:Pec nanoparticles are provided. Six chitosan to pectin ratios, 1:2, 2:3, 1:1, 3:2, 2:1, and 3:1, were explored by holding the total polymer concentration constant at 0.05% w/v in 50 mM AA.

3.3.5 pH Mediated CS:Pec Nanoparticle Swelling and Stability

The charge density of the polyelectrolytes depends on the pH of the solution, as well as the DA and DE of the chitosan and pectin, respectively. To study the effect of solution pH on nanoparticle size and zeta potential, CS:Pec nanoparticles were produced at a constant 1:1 mass ratio and titrated to various pH values (**Figure 5a**). All nanoparticles had a total polymer concentration of 0.05% w/v in 50 mM AA, consistent with the nanoparticles displayed in **Figure 4**.

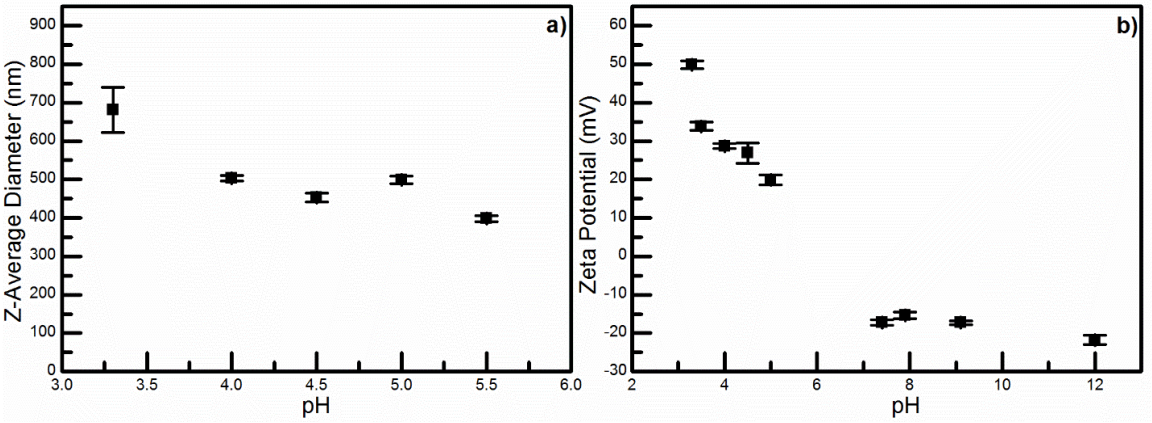

Figure 5: CS:Pec NP pH sensitivity to size and charge changes. Displayed is the effect that pH has on the (a) Z-average diameter and the (b) zeta potential of representative CS:Pec nanoparticles. Shown are CS:Pec nanoparticles with a 1:1 mass ratio synthesized from a 0.05% w/v polymer concentration in 50 mM AA. The pH was adjusted using 100 mM HCl and 100 mM NaOH.

Between pH values of 3.3 and 4.0, the particles underwent a significant decrease in average diameter, from 680 ± 60 nm to 500 ± 10 nm. At these pHs, the zeta potential

also decreased significantly, from 50 ± 1 to 29 ± 1 mV. At pHs between 4.0 and 5.5, the size remained relatively constant, ranging from 500 ± 10 nm to 400 ± 10 nm. Zeta potential over this range slowly decreased to 20 ± 1 mV before becoming unsuitable for zeta potential measurements. At pHs above 6.0, the particles dissociated and the chitosan precipitated out of solution, forming aggregates that were too large to be measured with DLS. At pHs of 6.0 and higher, the zeta potential remained close to −20 mV.

The pKa of the pectin is about 3.5, above which it will deprotonate.[19] Our findings are similar to Zhang et al.,[11] who reported that their CS:TPP nanoparticles deprotonated around a pH of 2.3. As the anions in the particle cross the pKa, the charge density increased and the average size of the particles decreased markedly. Pectin is partially charged at pH values between 3.0 and 3.5 and fully charged at pHs above 3.5. Due to the increased complexation between chitosan and pectin, the zeta potential of the particles decreased with increasing pH. The decrease in zeta potential between 4.0 and 5.5, might be due to the following factors: (i) increasing ionic strength might lead to improved chain flexibility and tighter polyelectrolyte complexation and/or (ii) chitosan might be deprotonating as the pH increases toward 6.0. At a pH of 6, the dissociation of chitosan is expected because chitosan with a DA below 20% have an intrinsic pKa of ~6.5.[75] Thus, the -20 mV zeta potential reported at pH values above 6.0 likely corresponds to free pectin in solution.

3.4 Conclusion

In this work, aqueous solutions of chitosan and pectin were synthesized into polyelectrolyte complexes that were three orders of magnitude smaller than particles

previously reported.[15,79,80] The size, surface charge, and morphology of the LMW CS:Pec nanoparticles were examined using DLS, electrophoretic DLS, and TEM, respectively. Concentration and order of addition effects were similar to those previously reported for other polysaccharide-based polyelectrolyte complex nanoparticles. By adjusting the mass ratio of the respective polymers, zeta potential was shown to be tunable without a significant change in particle size, enabling antibacterial activity optimization. The particles in solution were found to degrade over the course of 30 days, losing stability after 14 days. The particles were found to be stable across a tunable pH range from 3.5 to 6.0. Our "green" particles hold great promise for use in wound healing ointments or bandages, pending future antibacterial and anti-inflammation activity testing. Potential future work could focus on two key areas: proving that the nanoparticles retain antibacterial and anti-inflammatory properties and improving particle stability. The use of metal nanoparticle cores or quaternized chitosan could enhance stability.

CHAPTER 4

TUNING CS:PEC INTERACTIONS TO PRODUCE THERMOREVERSIBLE CS:PEC HYDROGELS

Adapted from: Birch, N. P.; Barney, L. E.; Pandres, E.; Peyton, S. R.; Schiffman, J. D. Thermal-Responsive Behavior of a Cell Compatible Chitosan/Pectin Hydrogel. *Biomacromolecules* **2015**, *16* (6), 1837–1843.

4.1 Introduction

Biopolymer hydrogels are important materials for wound healing and cell culture applications.[6,7] While modern synthetic polymer hydrogels are nontoxic and have excellent biocompatibility, their primary function is usually as a passive support matrix that does not supply any additional bioactivity.[7] Chitosan (CS) is commonly used in hydrogels due to its nontoxic, antibacterial, biodegradable, and biocompatible nature. These factors make CS hydrogels highly desirable products.[7–13] CS requires cross-linking to form structures with sufficient chemical stability and mechanical properties. Unfortunately, most commonly utilized crosslinking agents - glutaraldehyde,[65] carbodiimide,[93] and diphenylphosphoryl azide[94] - are cytotoxic. Greener options, like sodium tripolyphosphate[88,95] and genipin[8,96] are nontoxic but do not contribute any active functionality. Polymer−polymer gelation featuring a polycation and a polyanion has also been utilized to effectively cross-link CS-based wound healing hydrogels.[10,97] However, similar to the small molecules previously noted, most of these hydrogels have relied on passive polyanions. For example, alginate, a biocompatible polysaccharide, is the most

common polyanion because it is hydrophilic and enables good exudate uptake.[97,98] However, alginate has been reported to have a pro-inflammatory effect.[99] This makes finding an alternative active polyanion desirable.

An underexplored polyanion that has promising anti-inflammatory[14,15] properties is pectin (Pec). Pec deprotonates above a pH value of approximately 3.5.[19] The high hydrophilicity of Pec is similar to that of other wound healing polyanions, but it has been reported to have an additional strong anti-inflammatory effect.[15] This effect is very desirable for treating burns and chronic diabetic wounds. The strong anti-inflammatory activity is due to Pec's high level of esterified galacturonic acid residues which suppress the expression of iNOS (cytokine-inducible nitric oxide synthase) and COX-2 (cyclooxygenase-2), two of the most important enzymes in the inflammation process.[14,15]

Previously, the electrostatic interactions between CS and Pec have been used to generate a variety of structures, including millibeads,[100] microbeads,[79–81] nanoparticles,[101] and thin films.[10] Generating flat surfaces through CS:Pec electrostatic interactions requires long coalescence times and yields rough and irregular membranes.[10] To date, only one manuscript, by Norby et al.,[9] has demonstrated that thermoreversible CS:Pec hydrogels could be synthesized. They used 1 M hydrochloric acid (HCl) to protonate the Pec and enable gelation and hydrogen bonding between the two biopolymers.[9] However, the high level of acid used is not conducive to cell culture and wound healing applications. A hydrogel synthesized under physiological conditions would be very desirable.

In this study, we characterized the rheological properties of a new CS:Pec hydrogel system, explored the rehydration of the hydrogels, and demonstrated that the hydrogels are compatible with mammalian cells. By using salt to suppress long-range electrostatic interactions, we generated a thermoreversible hydrogel that has temperature-sensitive gelation. Changing from the previously demonstrated acid-based system[9] to a salt-based system yields hydrogels that are much closer to physiological conditions immediately after synthesis. Using rheology, we analyzed the tan δ, the ratio of the dynamic moduli, and determined the gel point using the Winter-Chambon[102] method. As a proof of concept, we removed the salt from our hydrogels, thus, creating thick and easy to cast polyelectrolyte complex (PEC) hydrogels, whose synthesis was previously limited by phase seperation.[10,79–81] For the first time, we explore the capability of thermoreversible CS:Pec to support human marrow-derived stem cells.

4.2 Experimental

4.2.1 Preparation of CS:Pec Hydrogels

CS MMW and Pec stock solutions were prepared at a polymer concentration of 1.5 wt %. MMW CS stock solutions were prepared by mixing in 0.1 M AA at 60 °C for 12 h. Pec stock solutions were prepared by mixing in DI water at room temperature (25 °C) for 12 h. Samples were stored at 4 °C until use in hydrogel preparation. Hydrogel samples were prepared by mixing 10 mL of MMW CS stock solution with a measured amount of sodium chloride. A 2 mL volume of dilute HCl was added to bring the hydrogel to the desired acid concentration. The solution was then heated until it cleared.

Pec solution (10 mL) was added, and the solution was heated to 97 °C. Samples were stored at 4 °C.

4.2.2 Characterization of Chitosan:Pectin Hydrogels by Rheology

Small amplitude oscillatory shear measurements were performed in a Kinexus Pro rheometer (Malvern Instruments, U.K.) using a concentric cylinder geometry with a diameter of 25 mm and horizontal gap of 1 mm, run with a vertical gap of 1 mm. The sample was injected into the cell at 80 °C, the geometry was lowered into position, and the top of the geometry was sealed using mineral oil to prevent solvent evaporation. A strain amplitude sweep was performed to ensure that experiments were conducted within the linear viscoelastic region and a strain percent of 5% was selected. Oscillation frequency sweeps were conducted over an angular frequency domain. The measuring unit utilizes a temperature control unit (Peltier cylinder cartridge) to achieve rapid temperature changes and ±0.01 °C temperature control. The sample was allowed to gel for 4 h at 25 °C before measurement commenced and was given 20 min to equilibrate at each temperature. Additional samples were run with 1 h thermal equilibration times over a narrower range to corroborate the results from the 20 min runs. There were no signs of degradation over the course of repeated oscillatory shear measurements at varying temperatures. No signs of hysteresis were found when the sample was heated or cooled, which demonstrated the reversibility of the gelation.

4.2.3 Drying and Swell Testing

Samples used for swell testing were reheated until liquid and cast into 13 × 13 mm square petri dishes and allowed to gel. Discs with a diameter of 2.56 cm were then

cut using a Spearhead 130 punch set (Zimmerman Packing and MFG., Cincinnati, Ohio) and placed on parafilm to dry in a fume hood for 6 days. Hydrogels were then removed from parafilm, weighed, and placed in 100 mL of phosphate buffered saline (pH 6.0 or 7.4) for a set period of time and removed, gently wiped dry, and weighed. The hydrogel swelling ratio in percent (%) was calculated using the following equation, (mf − mi)/mi × 100%, where mi and mf were the initial and final weights of the hydrogel, respectively.

4.2.4 Characterization of Cell Compatibility with Chitosan/Pectin Hydrogels

Telomerase-modified (hTERT), human marrow-derived stem cells (MSCs), a generous gift from Linda Griffith (Massachusetts Institute of Technology), were routinely cultured in Dulbecco's modified eagle's medium supplemented with 10% fetal bovine serum, 1% penicillin-streptomycin, 1% nonessential amino acids, 1% L-glutamine, and 1% sodium pyruvate at 37 °C and 5% CO_2. All cell culture supplies were purchased from Life Technologies (Carlsbad, CA).

4.2.5 Cell Viability

Sterile hydrogels were prepared by repeating the hydrogel synthesis protocol under sterile conditions. Each well of a 12-well plate was filled with 1.3 mL of sterile liquid hydrogel precursor by pipet. The plates were left to dry in a laminar flow hood for 2 days. Nonrinsed hydrogels were used immediately. Individual well plates containing rinsed hydrogels were rinsed twice in 500 ml sterile DI water before use. Rattail Collagen 1 (Life Technologies, Carlsbad, CA) was then passively adsorbed to hydrogels at 1 $\mu g/cm^2$ at room temperature overnight. Hydrogels were rinsed 4× in sterile phosphate-buffered saline, UV sterilized for 6-12 h, then incubated with complete cell culture

medium overnight. MSCs were seeded onto the hydrogel surfaces at 10000 cells/cm^2 and the medium was changed every 2 days for 14 days. At days 1, 4, 7, 10, and 14, live cells were stained with 4 μM ethidium homodimer-1 (nuclear stain to indicate dead cells) and 2 μM calcein AM (cytosolic stain to stain all cells; Life Technologies, Carlsbad, CA) in serum -free medium for 30 min. Imaging was performed using a Zeiss Spinning Disc Cell Observer SD (Zeiss, Jenna, Germany) at 20× magnification. Area of cell spheroids was quantified via manual tracing in ImageJ *1.48p* software (National Institutes of Health, Bethesda, MD). N = 2 independent biological replicates were performed and quantified.

Protein Absorption was quantified by pipetting 100 μL of sterile hydrogel precursor into 96 -well plates. These hydrogels were dried and a subset were rinsed, as previously described. BSA concentrations ranging from 0 to 1250 μg/cm^2 were passively absorbed to the hydrogel surfaces at room temperature for 24 h on a rotator. Hydrogels were rinsed 4× with phosphate-buffered saline, 250 μL Bradford reagent (Pierce Biotechnology, Rockford, IL) was added per well, and absorption at 600 nm was read (Biotech ELx800, 783 Winooski, VT, U.S.A.) after 5 min incubation. N = 2 independent replicates were performed and quantified. Data was normalized to the blank for each hydrogel condition.

4.2.6 Statistical Analysis

Statistical analysis was performed using Prism v6.0b. Data are reported as mean ± standard error. Statistical significance was evaluated using an unpaired, two-tailed t-test.

P-values <0.05 are considered significant, where $p<0.05$ is denoted with *, ≤ 0.01 with **, ≤ 0.001 with ***, and ≤ 0.0001 with ****. $p \geq 0.05$ is considered not significant ("ns").

4.3 Results and Discussion

4.3.1 Characterization of Rheology and Swelling of Chitosan/Pectin Hydrogels

After successfully synthesizing CS:Pec hydrogels, samples were physically characterized using three methods. The first of these was bulk rheology to determine the strength and temperature response of the hydrogel systems. Temperature had a strong effect on the viscoelastic properties of the CS:Pec hydrogels at three HCl concentrations (0.00, 0.02, and 0.04 M), a fixed ionic strength of 1.050 M, and a total polymer concentration of 1.5 wt %, **Figure 6**. The elastic moduli dominates throughout, though the gap between the elastic and viscous moduli varies with temperatures. The elastically dominated behavior is common and implies that the material is a fairly elastic pseudo-plastic.[9] The decreasing gap between the elastic and viscous moduli at high temperatures suggests that there is a phase transition that does not overcome the naturally elastic behavior of the heated CS:Pec solution.[9,103]

The rheological properties of hydrogels can also provide important insight into their potential end uses. In cases where a soft solid is involved, small amplitude oscillatory shear provides extensive rheological data without destroying the interior structures. The storage (G′) and loss moduli (G″) of the material help to illuminate the elastic and viscous natures of the hydrogel. The ratio of these moduli, tan δ, is the ratio of lost energy to stored energy, and is a valuable measure of material phase.[9,104]

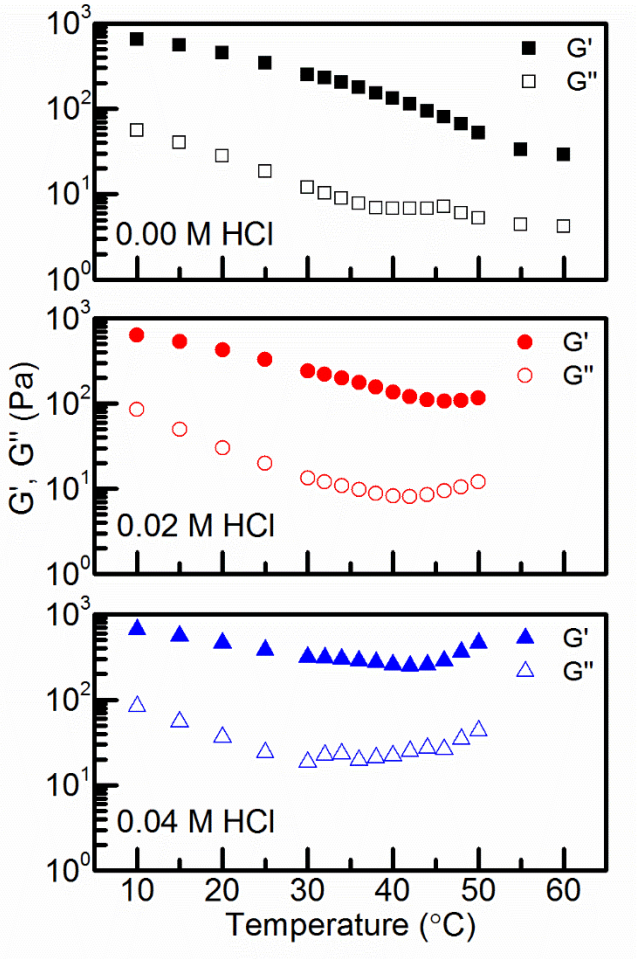

Figure 6: CS:Pec hydrogels have strong temperature dependence. Temperature dependence of the elastic and viscous moduli (at a fixed frequency of 6.28 rad/s) for aqueous mixtures of CS:Pec in (top-to-bottom) 0.0, 0.02, and 0.04 M HCl.

The Winter−Chambon method was utilized to quantify gelation temperatures for increasing acid concentrations.[102] This method defines the gelation point as the point where the tan δ (the viscous modulus over the elastic modulus) values become frequency independent. This phenomenon is demonstrated in **Figure 12**, which shows the increase in the spread of tan δ with temperature. Tan δ does not collapse into total frequency independence, but does exhibit two distinct phases, a hydrogel phase with very low

frequency dependence and a solution phase with higher frequency dependence. The gelation temperature has been found to be accurate (±1 °C) by close inspection of the raw data. The observed gelation temperature displays no sign of hysteresis: cooling and heating produces the same result. Results are independent of temperature change direction and magnitude.

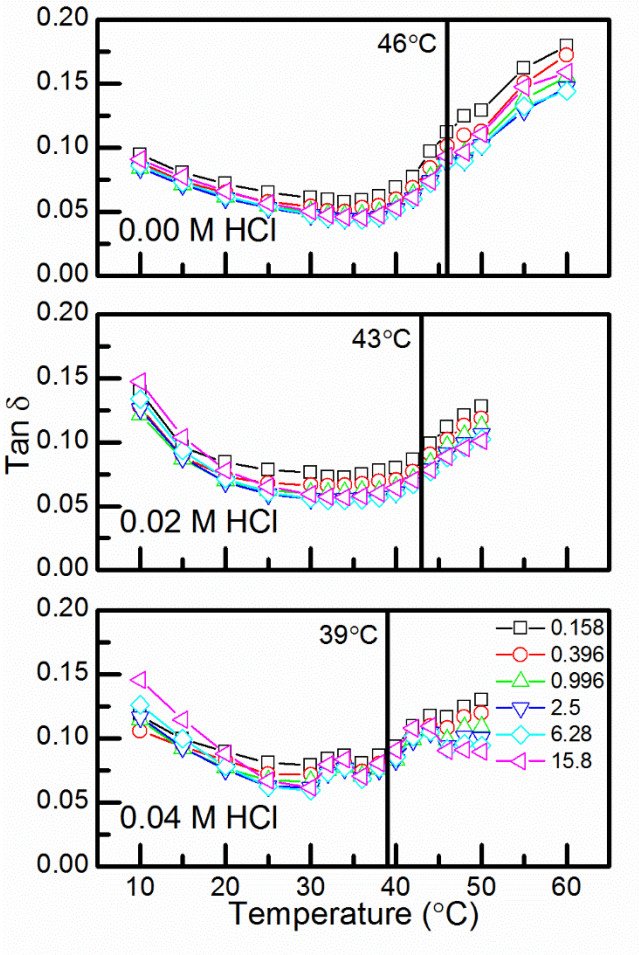

Figure 7: Temperature dependence of CS:Pec gelation. Temperature dependence of tan δ for CS:Pec in (top-to-bottom) 0.0, 0.02, and 0.04 M HCl. Gelation temperatures are shown as vertical black lines.

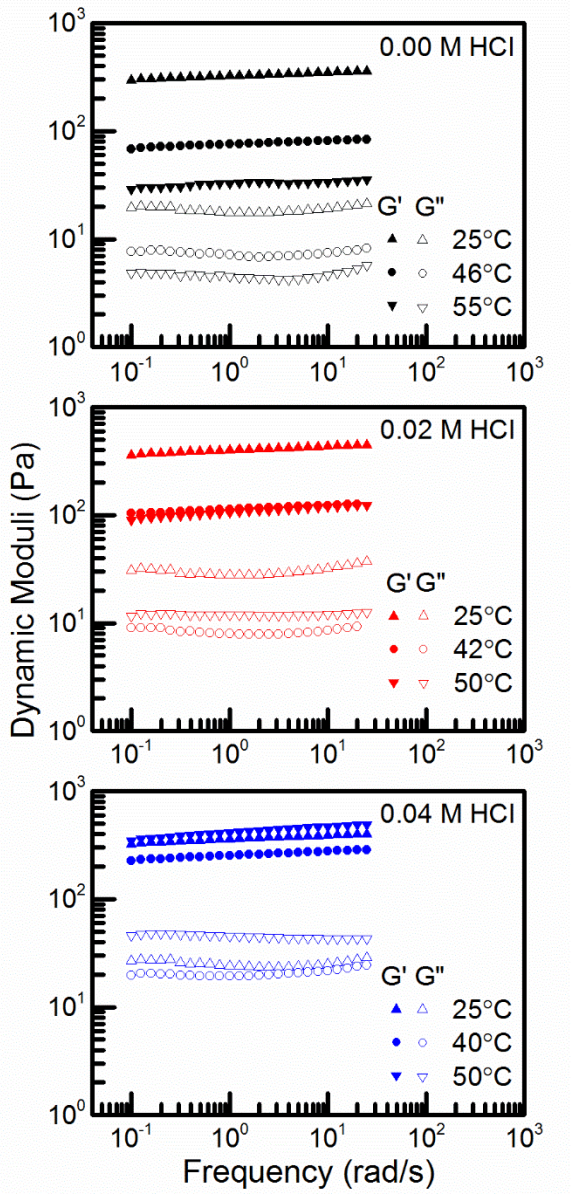

Figure 8: Acid concentration effects on dynamic moduli at relavent temperatures. Frequency dependence of the dynamic moduli for CS:Pec in (top-to-bottom) 0.0, 0.02, and 0.04 M HCl below gelation temperature (25 °C), at gelation temperature (46, 42, 40 °C), and above gelation temperature (55, 50 °C).

Figure 8 further demonstrates the frequency independence of the elastic moduli regardless of temperature or acid concentration. In all cases, the frequency dependence of

the dynamic moduli increases as the temperature is near or above the gelation temperature. G′ remains above G″ at all temperatures and the two lines remain parallel in most cases. When the complex viscosity is analyzed, **Figure 9**, the results are similar to the results from the dynamic moduli. The slope of every line is very close to −1, meaning that even the solution phase is relatively elastic with a low level of viscous deformation. There is a strong temperature dependence in both the hydrogel and solution phases, however this effect is diminished by increasing the acid concentration. The similarity of behavior among the systems means that acid content can be fully minimized to 0.00 M HCl without losing thermoreversibility. Small amounts of acid can also be used to tune the gelation temperature very sensitively.

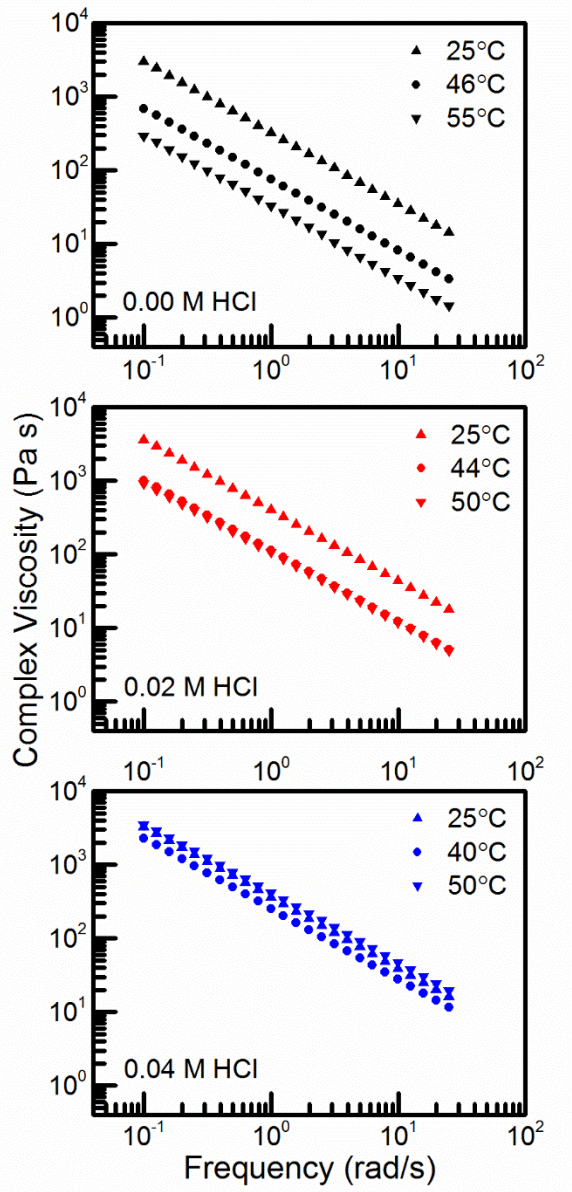

Figure 9: Acid concentration effects on complex viscosity at relavent temperatures. Frequency dependence of complex viscosity for CS:PEC in (top-to-bottom) 0.00, 0.02, and 0.04 M HCl below gelation temperature (25 °C), at gelation temperature (46, 42, 40 °C), and above gelation temperature (55, 50 °C).

The dynamic moduli and complex viscosity of an incipient hydrogel can be described by a simple power law where G′ is described by eq 1, G″ by eq 2, and η* by eq

3.[9,102,103] The dynamic viscosity is defined by the Legendre gamma function (Γ(n)), the viscoelastic exponent (n), and the hydrogel strength parameter (S). The hydrogel strength parameter relates the molecular chain flexibility and the cross-linking density of the hydrogel.[9] As we can see from eqs 1 and 3, when the elastic modulus is frequency independent (n = 0), the complex viscosity should have a slope of -1.

$$G'(\omega) = \frac{S\pi\omega^n}{2\Gamma(n)\sin(n\pi/2)} \qquad \textbf{Equation 1}$$

$$G"(\omega) = \frac{S\pi\omega^n}{2\Gamma(n)\cos(n\pi/2)} \qquad \textbf{Equation 2}$$

$$|\eta^*(\omega)| = \frac{\pi S\omega^{n-1}}{\Gamma(n)\sin(n\pi)} \qquad \textbf{Equation 3}$$

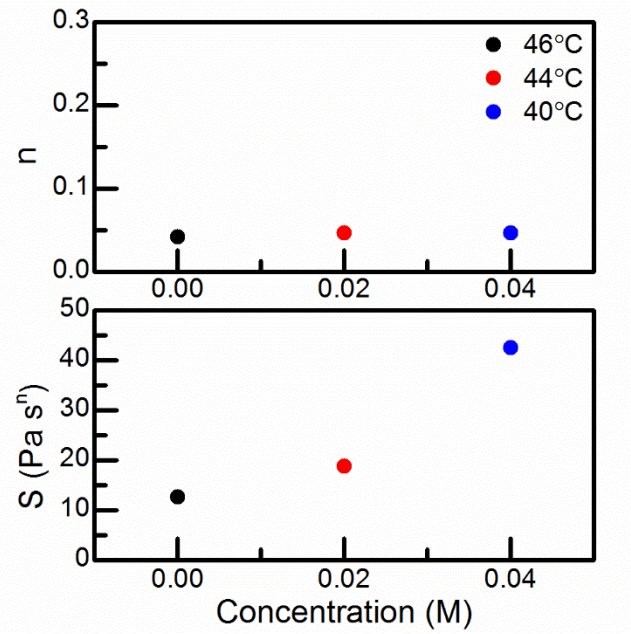

Figure 10: Viscoelastic exponent and hydrogel strength parameter as a function of acid concentration. The viscoelastic exponent, n, and the hydrogel strength parameter,

S, for CS:PEC in (top-to-bottom) 0.00, 0.02, and 0.04 M HCl at gelation temperature (46, 42, 40 °C).

At each CS:Pec acid system's gelation temperature, power law fits were obtained for the complex viscosities in **Figure 9**, and values for n and S were calculated, **Figure 10**. The incipient hydrogels remain almost entirely frequency independent ($n \sim 0.05$), regardless of acid concentration. However, the hydrogel strength changes strongly with acid concentration. This effect could be explained by a decrease in the density of hydrogen-bonding crosslinks as Pec protonates, or the result of the chain stiffness of MMW CS and Pec changing as the pH increases.[9]

4.3.2 Characterization of Swelling of Chitosan/Pectin Hydrogels

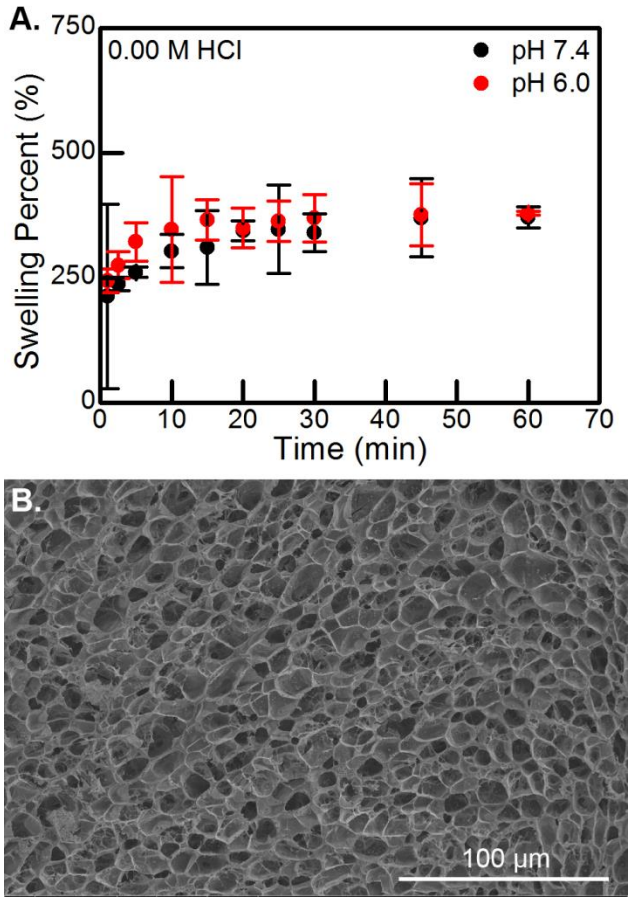

Figure 11: The swelling behavior of CS:Pec hydrogels and the SEM cross-section of the same. (A) Swelling versus time for 0.00 M HCl CS:Pec hydrogels at pH values of 7.4 and 6.0. (B) SEM micrograph displays the cross-section of a lyophilized post-synthesis 0.00 M HCl CS:Pec hydrogel, the scale bar is 100 µm.

Swell testing and scanning electron microscopy (SEM) were performed to gain insight into the ability of the hydrogel to uptake fluid and release loaded agents. The as-synthesized hydrogels had a theoretical swelling ratio of ~6600%. However, when the hydrogels were systematically dried and then swollen, they were not able to take up anywhere near that amount of water. **Figure 11** displays that dried hydrogels absorbed

their maximum amount of phosphate buffered saline solution quickly, within 15 min. This is consistent with previously studied CS:Pec hydrogel systems.[10] The swelling was not affected by pH value: After 1 h, at pH values of 7.4 and 6.0, the CS:Pec hydrogels swelled to 370 ± 20% and 370 ± 4%, respectively, which is consistent with previous CS:Pec hydrogels.[10] The two rehydration curves are statistically identical with the exception of the 5 min time points. SEM micrographs suggest that the hydrogel contains a wide range of pore sizes, some as large as 30 μm. Since the limitations of acquiring micrographs on lyophilized hydrogels are well-known, an average pore size was not quantified. Our micrographs are intended to show comparison to other hydrogels prepared and imaged using a similar method. However, we can hypothesize that the swell testing data was extremely variable due to the observed high variability in pore size. It is likely that the statistical significance in the 5 min time points is not indicative of a real difference. It is likely that, as the swelling ratio decreased with drying and rehydration, the pore size did as well.[105] Even so, these large pores should allow the loading and release of even very large proteins. The rapid swelling, high equilibrium swelling ratio, and large pore size suggest that our hydrogel system may be appropriate for a wound dressing since it can absorb large volumes of exudate.

4.3.3 Characterization of Cell Compatibility with Chitosan/Pectin Hydrogels

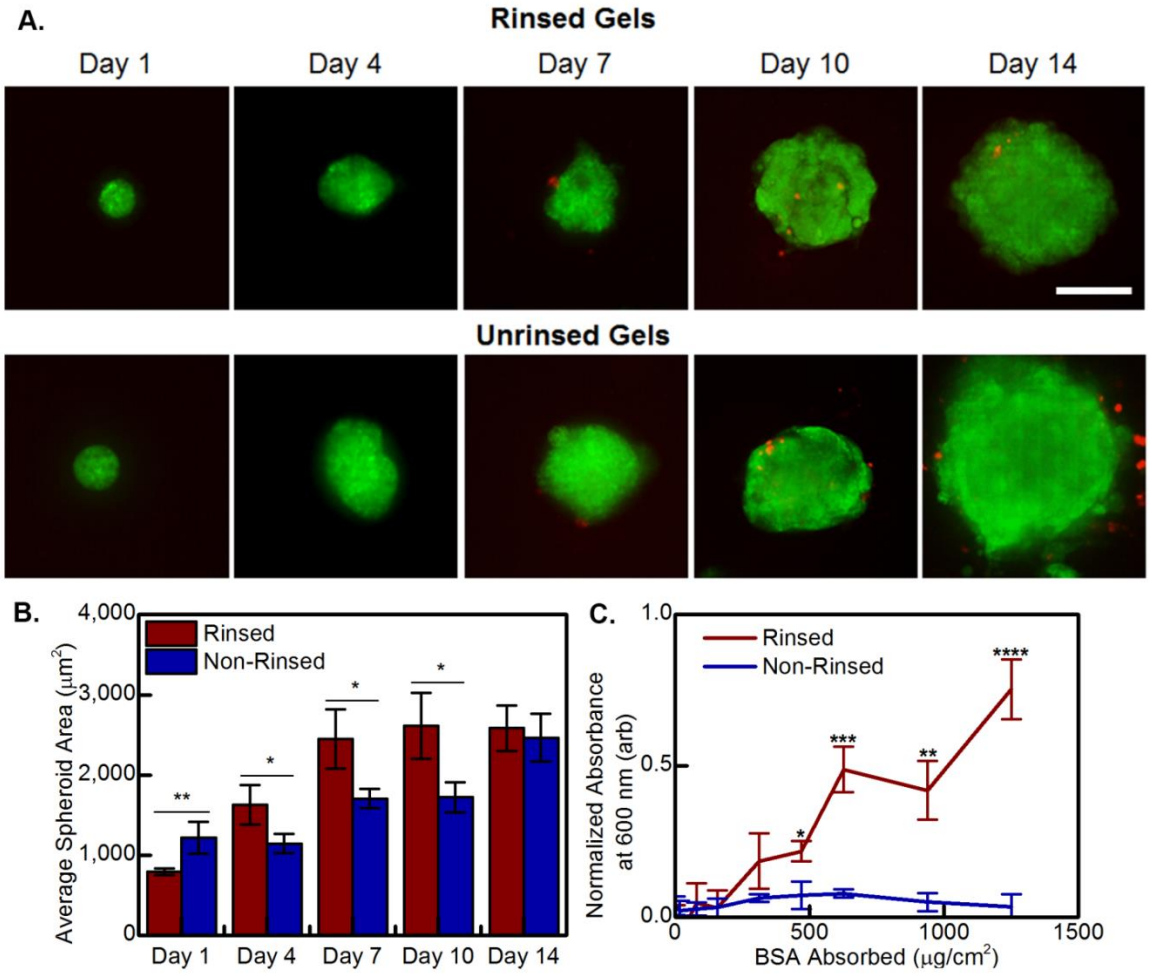

Figure 12: MSC spheroid size, average spheroid size, and the protien abosption of BSA on CS:Pec hydrogels. (A) Representative hTERT MSC spheroids over a 14 day compatibility test on (top) rinsed and (bottom) non-rinsed 0.00 M CS:PEC hydrogels. Cells are stained with live (green, Calcein AM) and dead (red, Ethidium homodimer-1) stains. (B) Average spheroid area as a function of time. (C) The of passive absorption of BSA to the 0.00 M CS:PEC hydrogels, is provided.

After fully characterizing the physical properties of the CS:Pec hydrogels, their compatibility with cells in physiological conditions was explored. Telomerase-modified, human marrow-derived stem cells, were used due to their extensive role in wound healing.[106] We theorized that the high salt level in the dried CS:Pec hydrogels would result in cell death, so a rinsing procedure was implemented. Both rinsed and nonrinsed 0.00 M HCl CS:Pec hydrogels were tested for cell viability. Notably, **Figure 12A** displays that no significant stem cell death occurred as a result of the stem cells contacting either the rinsed or nonrinsed CS:Pec hydrogels over a 14 day period. Even with passive absorption of an adhesive ligand there was a low level of adhesion to the CS:Pec hydrogels.[107] The stem cells did not adhere and spread, but adhered to other cells and formed spheroids. These spheroids have been previously reported for chitosan-based hydrogels.[108] At 1 day after seeding, spheroid size was greater on the non-rinsed CS:Pec hydrogels, but there were fewer of these spheroids (data not shown). This led us to explore the possibility that the CS:Pec hydrogels differed in their ability to absorb proteins, resulting in the differential cell spheroid formation. BSA absorption was quantified, and the results are provided in **Figure 12C**. The nonrinsed CS:Pec hydrogels absorbed less protein, likely resulting in the poor cell adhesion. The increased protein absorption we observed after rinsing is likely due to the removal of charge screening ions. However, these differences were only observed at protein concentrations significantly higher than the passively absorbed collagen or serum we introduced, explaining both the minimal differences in morphology and the lack of cell spreading that we observed in both CS:Pec hydrogel systems.

The ability of CS:Pec hydrogels to promote long-term cell survival and proliferation was also explored. Marrow-derived stem cell spheroids were heterogeneous and increased in size over the 14 day culture period, but initially grew larger more quickly on the rinsed CS:Pec hydrogels, **Figure 12B**. The initial difference in spheroid growth rate tapered off and disappeared by day 14, likely due to salt leaching out from the nonrinsed CS:Pec hydrogels during media replacement. The low level of cell adhesion and lack of cell death over 14 days of culture demonstrate that the CS:Pec hydrogels are both safe for physiological use and likely will not stick to wounds if used as a bandage, thus facilitating the changing of dressings. The difference between the rinsed and nonrinsed CS:Pec hydrogels can be partially explained by the differences in protein uptake, but it is likely that the removal of charge screening ions by rinsing may have some effect on hydrogel stiffness and morphology. While stem cells have been shown to form spheroids on chitosan-based materials,[108,109] keratinocytes, fibroblasts, and epithelial cells usually do not form spheroids and have shown good attachment.[110,111] The physical properties of chitosan materials can induce spheroid formation through a combination of factors,[112] and thus, further study is needed to determine if the spheroid behavior is due to the cell type used in this study or the physical properties of the CS:Pec hydrogels.

4.4 Conclusion

In this work, we have described the synthesis and have fully characterized the physical properties of a biologically compatible thermoreversible CS:PEC hydrogel. We examined the effects of three acid concentrations, 0.00, 0.02, and 0.04 M HCl, before determining that CS:Pec hydrogel strength and temperature were both improved by fully

replacing the acid content with salt. The CS:Pec hydrogels were found to continue to strengthen at lower temperatures. At pH values of 6.0 and 7.4, the dried hydrogels rapidly swelled to ~370% of their initial weight. Our acid-free CS:PEC hydrogels were biocompatible with human marrow-derived stem cells after drying. Notably, protein absorption and cell proliferation were improved by rinsing the hydrogels. By using salt to suppress long-range electrostatic interactions, we have synthesized novel CS:Pec hydrogels with excellent exudate uptake that hold potential as bandages for chronic wound healing. Directions for future work include animal testing with diabetic mice and the diffusion of potential drugs for delivery.

CHAPTER 5

RHEOLOGICAL CHARACTERIZATION OF CS/PEO:CINNAMALDEHYDE EMULSION FOR IMPROVED ELECTROSPINNING

Adapted from: Rieger, K. A.; Birch, N. P.; Schiffman, J. D. Electrospinning Chitosan/poly(ethylene Oxide) Solutions with Essential Oils: Correlating Solution Rheology to Nanofiber Formation. *Carbohydr. Polym.* **2016**, *139*, 131–138.

5.1 Abstract

Solution rheology can be a powerful tool for improving electrospun systems, chain entanglement (C_e) concentration and viscosity can give key insight into whether or not a solution will spin into defect-free fibers. However, the correlation between precursor solution properties and nanofiber morphology for polymer solutions electrospun with or without hydrophobic oils has not yet been demonstrated. Cinnamaldehyde (CIN) and hydrocinnamic alcohol (H-CIN) were electrospun in chitosan (CS)/poly(ethylene oxide) (PEO) nanofiber mats as a function of CS molecular weight and degree of acetylation (DA). Solution viscosity and chain entanglement (C_e) concentration were determined through a battery of stress sweeps with varying polymer concentrations and polymer:oil mass ratios. The maximum polymer:oil mass ratio able to be electrospun was 1:3 and 1:6 for CS/PEO:CIN and :H-CIN, respectively. A higher DA for chitosan increased the incorporation of H-CIN, but not CIN. The correlations determined for electrospinning plant-derived oils could potentially be applied to other

hydrophobic molecules, thus broadening the delivery of therapeutics from electrospun nanofiber mats.

5.2 Introduction

A major class of hydrophobic bioactive agents is essential oils. Due to the rise of antibiotic resistance, research into plant-derived agents has surged because they can inactivate microbes non-specifically.[113,114] Within the past two years, a number of essential oils, including, *Cinnamomum*,[60] *Thymus vulgaris*,[115] *Chamomilla recutita*,[116] *Cymbopogon*,[117] *Mentha piperita*,[117] *Acidum tannicum*,[118] *Eremanthus erythropappus*,[119] and *Centella asiatica*[120] have been electrospun within nanofiber mats as promising drug delivery vehicles. These papers focused on how the essential oil containing nanofiber mats influenced antibacterial activity and/or mammalian cell proliferation. However, the electrospinning parameters that control the quantity of immiscible phase solution that can be incorporated into nanofiber mats has not yet been investigated.

Previously, we electrospun cinnamaldehyde (CIN), a hydrophobic essential oil, using a chitosan (CS)/poly(ethylene oxide) (PEO) solution and quantified the incorporation, release, and antibacterial activity of CIN. CS, a polycationic derivative of chitin, was chosen because it is a non-toxic, antibacterial, biodegradable, and biocompatible biopolymer used for biomedical applications, such as drug delivery.[121] Due to the popularity of this biopolymer, the solution properties needed to electrospin CS/PEO solutions into nanofiber mats, including, total polymer concentration, CS molecular weight, and acid concentration have been experimentally determined.[42,122] However, the previous work was limited in scope. Here, for the first time, we determine

the chain entanglement concentration (C_e) of CS/PEO solutions as a function of CS molecular weight and degree of acetylation (DA). Additionally, we examine the C_e of CS/PEO in the presence of immiscible liquid phase agents. Nearly all essential oils rely on one of three chemical structures – phenols, aldehydes and alcohols – to exhibit biocidal activity.[113] Here two structurally different essential oils, CIN and hydrocinnamic alcohol (H-CIN) (**Figure 13**) were investigated. CIN is a aldehyde that can react with CS to form Schiff bases.[123–126] H-CIN was chosen as a model alcohol that does not Schiff base with CS. Understanding the parameters that enable the electrospinning of solutions containing hydrophobic molecules stabilized by CS-containing solutions provides a platform to broaden the potential biomedical applications of electrospun nanofiber mats.

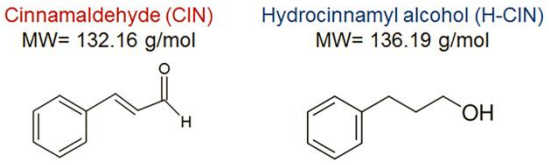

Figure 13: Cinnamaldehyde and hydrocinnamyl alcohol chemical structures. Cinnamaldehyde (CIN) or hydrocinnamyl alcohol (H-CIN) was incorporated into chitosan (CS)/poly(ethylene oxide) (PEO) solutions at a variety of different total polymer:oil (p:o) mass ratios.

5.3 Experimental

5.3.1 Materials and Chemicals

Low molecular weight chitosan (LMW CS, poly(D-glucosamine), Mw=460,000 Da), medium molecular weight chitosan (MMW CS, poly(D-glucosamine), Mw=1,000,000 Da), poly(ethylene oxide) (PEO, Mw=6,00,000 Da), ReagentPlus® grade

acetic acid (AA, ≥99.0%), cinnamaldehyde (CIN, ≥ 93%, FG, Mw = 132.16 g/mol), hydrocinnamic alcohol (H-CIN, ≥ 98%, FCC, Mw= 136.19 g/mol), deuterium oxide, and acetic acid-d4 (AA-d4) were obtained from Sigma-Aldrich (St. Louis, MO). Sodium hydroxide (NaOH) was obtained from Fisher Scientific (Fair Lawn, NJ). Deionized (DI) water was obtained from a Barnstead Nanopure Infinity water purification system (Thermo Fisher Scientific, Waltham, MA).

5.3.2 Modification and Characterization of CS

A modified medium molecular weight chitosan (MOD-MMW CS, M_w=1,000,000 Da) was synthesized to provide a direct comparison of molecular weight and DA. MOD-MMW CS was produced through the deacetylation of the MMW CS by suspending 5.0 g of MMW CS in 100 mL of 45 w/w% NaOH. The solution was heated at 70 °C for 45 min. The MMW CS was then filtered and washed with DI water until a neutral pH was achieved.[127] The resultant powder was then dried for 12 hr in a vacuum oven at 25 °C.

Proton nuclear magnetic resonance (^{1}H NMR, Bruker Avance 400) along with SpinWorks3, an NMR analysis software, were employed to quantitatively determine the DA of the LMW, MMW, and MOD-MMW CS. Solutions for ^{1}H NMR containing 1.0 w/v% LMW, MMW, or MOD-MMW CS were dissolved in 0.5 M AA-d4 (500 µL). To analyze the interactions between CS and CIN or H-CIN, new ^{1}H NMR solutions at the previously mentioned solution parameters and polymer:oil (p:o) mass ratios of 1:0.2 and 1:0.4 were prepared.

5.3.3 Preparation of CS/PEO and Oil Loaded CS/PEO Solutions

A 1:1 weight ratio of LMW, MMW, or MOD-MMW CS/PEO (0.5 g/0.5 g) in 0.5 M AA (20 mL) corresponding to total polymer concentrations ranging from 0.25 to 5.0 w/v% solutions were mixed for 24 hr at 20 rpm using an Arma-Rotator A-1 (Bethesda, MA). CIN or H-CIN (**Figure 13**), was added to a LMW, MMW, or MOD-MMW CS/PEO solution to form an oil loaded solution ranging from 1:0.2 to 1:12 p:o mass ratio. These solutions were mixed for an additional 24 hr, at which point, the solution changed from transparent to opaque. Throughout the mixing process, the solution had a pH value of 4. Within this manuscript, all solutions were prepared in a similar manner using a 1-to-1 CS to PEO weight ratio.

5.3.4 Characterization of CS/PEO and CS/PEO(CIN or H-CIN) Solutions

Oil-loaded solutions with and without PEO were imaged using a Zeiss Optical Microscope (Axio Imager A2) to qualitatively examine (i) the polydisperisty of the oil droplets and (ii) the effect of PEO addition on oil droplet size for 1:0.5, 1:1, 1:2 and 1:5 p:o mass ratios. The contact angle of the CS/PEO and oil-loaded CS/PEO solutions were determined using a home-built digital Olympus camera imaging setup to capture solution droplets. Solutions for contact angle analysis had a total polymer concentration of 2.5 w/v% for MMW and MOD-MMW CS/PEO, and a total polymer concentration 5.0 w/v% for LMW CS/PEO. All oil loaded solutions were mixed with a 1:1 p:o mass ratio. *Image J* 1.45 software (National Institutes of Health, Bethesda, MD) was used to measure the contact angle. The average contact angle along with the standard deviation for each solution was obtained by measuring three droplets.

LMW, MMW, and MOD-MMW CS/PEO solutions with total polymer concentrations ranging from 0.25 – 5.0 w/v% were used for rheology. The oil (CIN or H-CIN) was added at a 1:1 p:o mass ratio. Viscosity measurements were performed using a Kinexus Pro rheometer (Malvern, UK) using a concentric cylinder geometry, with a diameter of 25 mm, horizontal gap of 1 mm, run with a vertical gap of 1 mm. A viscosity stress sweep was conducted from 0.1 to 10 Pa. There were no signs of phase separation over the course of measurement. Measurements were conducted at 25 ºC. A Newtonian plateau was observed within this range, and the average value of the plateau was reported. The resulting data was fit using a two-phase power regression to determine the change over from the untangled regime to the entangled regime.[100,122] Viscosity stress sweeps were conducted from 0.1 to 1,000 Pa. Solutions contained a fixed total polymer concentration of 2.5 w/v% MMW CS/PEO and were loaded with CIN and H-CIN p:o mass ratios ranging from 1:0 to 1:12. A Carreau-Yasuda model was fit to the data and plotted to compare both the raw and fitted data.

5.3.5 Electrospinning of CS/PEO and CS/PEO(CIN or H-CIN) Solutions

LMW, MMW, and MOD-MMW CS/PEO solutions were electrospun at total polymer concentrations ranging from 0.25 - 5.0 w/v%. CIN or H-CIN was added to the LMW, MMW, and MOD-MMW CS/PEO solutions at p:o mass ratios between 1:1 and 1:12. If the CIN or H-CIN was fully incorporated into the CS/PEO solution (i.e., no large bubbles/macrophase separation was observed), then the solution was electrospun.

Electrospinning solutions were loaded into a 5 mL Luer-Lock tip syringe capped with a Precision Glide 18 gauge needle (Becton, Dickinson & Co. Franklin Lakes, NJ), which was secured to a PHD Ultra syringe pump (Harvard Apparatus, Plymouth Meeting, PA). Alligator clips were used to connect the positive anode of a high-voltage supply (Gamma High Voltage Research Inc., Ormond Beach, FL) to the needle and the negative anode to a copper plate wrapped in aluminium foil. The assembled electrospinning apparatus was housed in an environmental chamber (CleaTech, Santa Ana, CA) with a desiccant unit (Drierite, Xenia, OH) to maintain a temperature of 22 ± 1 ºC and a relative humidity of 24-28%. All solutions were electrospun at a constant feed rate of 60 μL/min, a separation distance of 120 mm and an applied voltage of 35 kV.

5.3.4 Characterization of Electrospun CS/PEO and CS/PEO(CIN or H-CIN) Nanofiber Mats

Micrographs of electrospun nanofibers were acquired using a FEI-Magellan 400 scanning electron microscope (SEM). A Gatan high resolution ion beam coater model 681 was used to sputter coat samples with ~5 nm of platinum. To confirm that the electrospun nanofiber mats released the oils, LMW CS/PEO solutions containing either CIN or H-CIN at a 1:0.2 p:o mass ratio were spun for 60 min. Nanofiber mats were then punched into circles with a 0.9525 cm diameter using a Spearhead® 130 Power Punch MAXiSET before being submerged in a 1.5 mL centrifuge vial containing 1 mL of DI water. The vials were mixed for 48 hrs at 20 rpm using an Arma-Rotator A-1. At 3, 24, and 48 hr, the 1 mL of solution from each film sample was tested via UV-Vis spectroscopy (Model 8453, Agilent Diode Array, Santa Clara, CA) at an absorbance of

293 and 288 nm for CIN and H-CIN, respectively.[128,129] The absorbance of each aliquot was averaged and related to a concentration based on a standard calibration curve. Total CIN or H-CIN release, μg per nanofiber mat, is reported based on triplicate tests.

5.4 Results and Discussion

5.4.1 Characteristics of Chitosan (CS) Solutions

The ^{1}H-NMR spectra of LMW CS is displayed on **Figure 2** and is representative of the spectra acquired for LMW, MMW, and our in-house modified MOD-MMW CS. By taking the relative integrals of 1.7 – 2.4 ppm over 2.7 – 4.4 ppm, we calculated the degree of acetylation (DA) values for the three CSs.[83,85,130] The MMW CS had a molecular weight of 1,000,000 Da and a DA of 23%. The LMW and our MOD-MMW CS had molecular weights of 460,000 and 1,000,000 Da, respectively, and an identical DA value of 13%. This indicates that we have three CSs that will allow us to study the role that molecular weight and DA have on electrospinning immiscible phase oils.

5.4.2 Characteristics of CS:CIN and CS:H-CIN Solutions

The interactions between CS and each oil, CIN and H-CIN, were also characterized using ^{1}H-NMR, **Figure 14**. Peaks roughly around 7 ppm corresponding to aromatics are present for both CIN and H-CIN. Highlighted in grey are peaks at 9.0 ppm from unreacted aldehydes present on CIN and a peak at 9.5 ppm from reacted CIN, which is indicative of a Schiff base reaction.[123–126] The imine proton can be seen around 8.2 ppm as a small peak. No peaks are present at 9.0 or 9.5 ppm in the ^{1}H NMR spectra of CS:H-CIN because there is no aldehyde within the H-CIN chemical structure and thus, no Schiff base or substitution reactions. The degree of substitution (DS) values were

calculated from the ratio of the integrated resonances of reacted CIN (9.25 - 9.6 ppm) over glucosamine residues on chitosan (2.7 - 4.4 ppm).[123,131] The DSs for CS:CIN at 1:0.2 and 1:0.4 p:o mass ratios for the LMW, MMW, and MOD-MMW CSs were determined and are compiled in **Figure 14B**. The DS for the MMW and MOD-MMW CS are approximately equivalent and are two times greater than the DS of LMW CS.

A

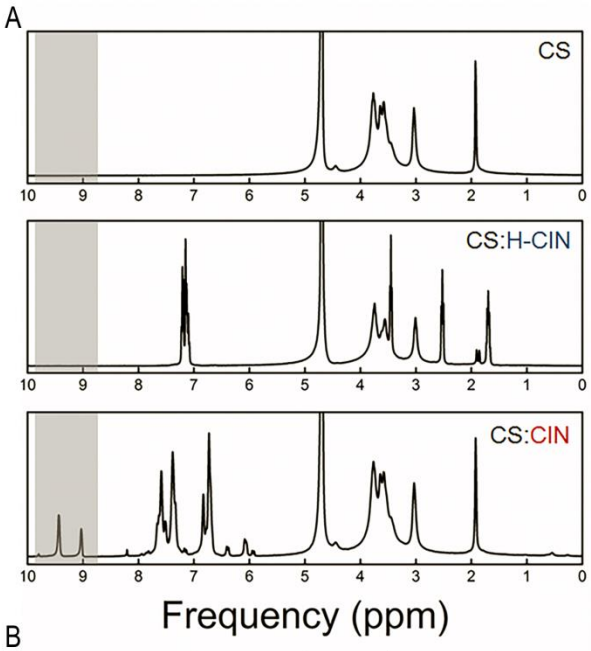

B

CS	MW (Da)	DA (%)	DS (%) 1:0.2 p:o CS:CIN	DS (%) 1:0.4 p:o CS:CIN
LMW CS	460,000	13	15	16
MMW CS	1,000,000	23	34	32
MOD-MMW CS	1,000,000	13	30	30

Figure 14: NMR spectra for the determination of degree of substitution. ^{1}H NMR spectra (a) of (top-to-bottom) CS, as well as CS:H-CIN and CS:CIN at a 1:0.2 p:o mass ratio. Section in grey highlights peaks due to CIN. Summary of the molecular weight (MW), degree of acetylation (DA), and degree of substitution (DS) (b) for CS:CIN solutions at 1:0.2 and 1:0.4 p:o mass ratios. H-CIN does not react with CS and therefore, no DS values are provided.

5.4.3 Characteristics of CS/PEO:(CIN or H-CIN) Solutions

CS has been suggested to act as a stabilizer[132–135] because it is composed of two blocks, 1,4-linked 2-amino-2-deoxy-β-*D*-glucan and 1,4 linked 2-acetamido-2-deoxy-β-*D*-glucan. To better understand how CIN and H-CIN were stabilized by CS within the electrospinning precursor solutions, images of the solutions with and without PEO were acquired. Qualitatively, the addition of PEO had little effect on the dispersion of oil. Due to the challenges of capturing enough representative images containing a statistically relevant number of oil droplets, we offer these images only as a qualitative characterization of the oil dispersion. The CIN droplets appeared larger and more polydispersed, while H-CIN droplets had a bimodal distribution featuring two smaller droplet sizes. As the mass ratio increases, both types of oil droplets appeared to increase in size and CIN became more polydispered, consistent with literature.[136]

Contact angle measurements were obtained for 5.0 w/v% LMW CS/PEO solutions, as well as for 2.5 w/v% MMW and MOD-MMW CS/PEO solutions, **Table 1**. These polymer concentrations were chosen because when electrospun, they yielded defect-free nanofibers (Section 3.2.1). MMW and MOD-MMW CS/PEO had similar contact angles of 28° and 31°, respectively, while LMW CS/PEO had a much higher contact angle of 37°. The difference in contact angle is likely due to the polymer concentration difference between the testing solutions. MMW and MOD-MMW CS/PEO solutions could not be prepared at 5.0 w/v% because they were too viscous. The contact angle for the LMW, MMW, MOD-MMW CS/PEO solutions after the addition of CIN and H-CIN at a 1:1 p:o mass ratio was also measured. Notably, the addition of CIN and

H-CIN at a 1:1 p:o mass ratio significantly decreased the contact angle to 20-25° for all CS/PEO solutions.

Table 1: Summary of CS/PEO and CS/PEO:(CIN or H-CIN) solution characteristics.

CS	Contact Angle (°)			Viscosity (Pa s)			C_e (%)		
	No Oil	CIN	H-CIN	Oil	CIN	H-CIN	No Oil	CIN	H-CIN
LMW CS	37.2±2.3	23.7±0.8	25.8±0.7	0.14	0.10	0.18	3.0	1.8	2.2
MMW CS	31.5±2.4	25.3±1.9	25.4±0.3	3.31	3.35	3.16	0.8	0.8	1.2
MOD-MMW CS	28.2±2.2	20.4±3.0	23.6±0.7	1.92	2.11	1.70	1.3	1.0	1.1

*All solutions were prepared at a 1/1 CS/PEO mass ratio. For solutions containing an oil, a 1:1 p:o mass ratio was used. The viscosity measurements were taken using 2.5 w/v% solutions.

5.4.4 Electrospinning of CS/PEO Nanofibers and Solution Rheology

CS (LMW, MMW, and MOD-MMW) solutions as a function of molecular weight and DA were successfully electrospun at a 1:1 weight ratio with PEO. As the total polymer concentration increased, the resulting nanofibers changed from exhibiting a bead-on-string to a defect-free nanofiber morphology, **Figure 15**. The MMW and MOD-MMW CS/PEO solutions, which have the same CS molecular weight but different DAs produced defect-free nanofibers at the same total polymer concentration of 2.0 w/v%. The LMW CS/PEO solution, which has a lower CS molecular weight but the same DA as the MOD-MMW CS needed a higher polymer concentration of 3.5 w/v% to electrospin into defect-free nanofibers.

While CS/PEO solutions have previously been electrospun, the polymer chain entanglement concentration (C_e) of the solutions has not yet been reported, **Figure 15** and **Table 1**. This is surprising seeing how the use of PEO enables CS to be spun using greener solvents. [121] The C_e predicts the "spinnability" of a precursor solution and the minimal polymer concentration needed to electrospin fibers with a bead-on-string morphology.[137–139] The LMW CS/PEO solution had a C_e of 3.0 w/v%, a slightly lower concentration than where defect free fibers were experimentally observed. The MMW CS/PEO and MOD-MMW CS/PEO solutions had C_e of 0.8 and 1.3 w/v%, respectively. Molecular weight had a strong impact on C_e because entanglement is a directly correlated with the length of the polymer backbone.[140] That the DA did not affect the C_e is an encouraging finding. This may suggest that despite the batch-to-batch variation that biopolymers experience,[121] electrospinning CS-containing solutions does offer some flexibility in terms of operational space. Experimentally, for LMW, MMW, and MOD-MMW CS/PEO solutions, defect free nanofibers were observed at 1.2-2.5 times C_e which corroborates well with previous rheological studies that have electrospun biopolymer solutions.[42,45,122,137] Klossner *et al.*[122] reported that the C_e of CS (148,000 Da, DA:15-25%) in aqueous acetic acid was 2.9 wt%. However, this CS concentration was notably too viscous to be electrospun.[122] Another study examined how PEO improves the "spinnability" of CS, however, they explored the C_e of the polymers separately and found results similar to our MMW and MOD-MMW CS/PEO mixtures.[42]

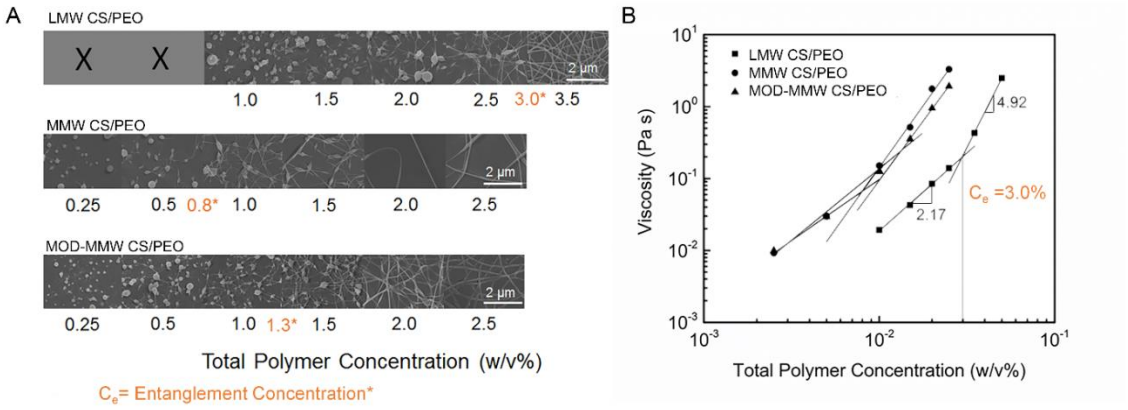

Figure 15: SEM morphology and rheological measurement at each polymer concentration. (a) SEM micrographs display the morphology of LMW, MMW, and MOD-MMW CS/PEO nanofibers electrospun with increasing total polymer concentration (left to right). On the LMW CS/PEO samples, an "X" indicates that there was no observable collection during electrospinning. The entanglement concentrations as estimated via rheology are also provided. All scale bars are 2 μm. (b) Specific viscosity versus total polymer concentration for LMW, MMW, and MOD-MMW CS/PEO solutions. A representative extrapolation of the entanglement concentration (C_e) is provided for LMW CS/PEO.

5.4.5 CS/PEO:(CIN or H-CIN) Solution Rheology

The addition of CIN or H-CIN at a 1:1 p:o mass ratio to the LMW CS/PEO solution had a strong impact on the C_e, **Figure 16** and **Table 1**. The addition of CIN and H-CIN reduced the C_e from 3.0 to 1.8 and 2.2 w/v%, respectively. The C_e of the MMW and MOD-MMW CS/PEO solutions remained relatively constant regardless of oil addition, varying overall from 0.8-1.2 and 1.0-1.3 w/v%, respectively. The type of oil had little effect on the C_e for all CS/PEO solutions.

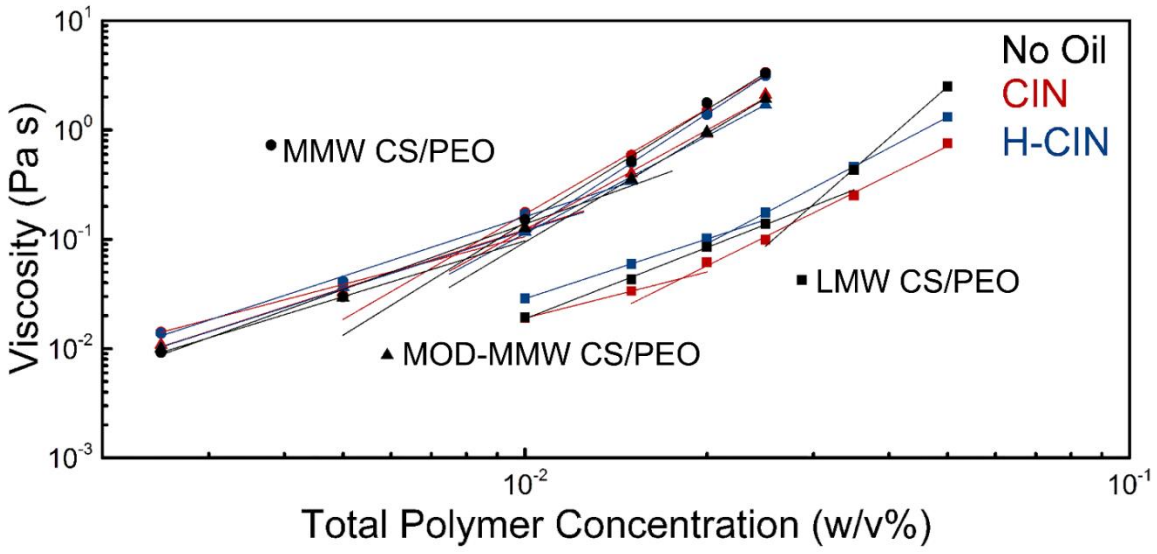

Figure 16: Specific viscosity of oil-loaded CS/PEO systems across a range of concentrations. Specific viscosity versus total polymer concentration for LMW, MMW, and MOD-MMW CS/PEO solutions, with CIN and H-CIN. The data is shown with a two-phase power regression. CIN and H-CIN were added at a 1:1 p:o mass ratio.

CS/PEO solution viscosity with and without CIN or H-CIN at a 1:1 p:o mass ratio was determined, **Table 1**. The viscosity of the LMW, MMW, and MOD-MMW CS/PEO solutions at 2.5 w/v% remained ~0.14, 3.3, and 1.9 Pa s, respectively, regardless of oil loading. The similar behavior between MMW and MOD-MMW CS/PEO solutions loaded with CIN or H-CIN suggests that the effect of DA on solution viscosity was small. A similar observation on viscosity was previously reported by the addition of surfactants to CS/PEO solutions.[141] As the polymer concentration of the LMW CS/PEO solution increased above its C_e (3.0 w/v%), the addition of oil strongly decreased the solution viscosity. At 5.0 w/v% the LMW CS/PEO solution viscosity decreased from 2.5 Pa s to 0.8 Pa s with CIN addition, and to 1.3 Pa s with H-CIN addition. Similar to C_e, the solution viscosity was only oil sensitive for the LMW CS/PEO solution.

Figure 17 displays how the MMW CS/PEO solution behavior changed due to the addition of CIN and H-CIN at p:o mass ratios from 1:0 to 1:10 and 1:12, respectively. A Carraeu-Yasuda fit (Equation 1) was applied to further analyze the data.

$$\eta = \eta_\infty + (\eta_0 - \eta_\infty)[1 + (\lambda\dot{\gamma})^a]^{\frac{n-1}{a}} \qquad \textbf{Equation 4}$$

Wherein the apparent viscosity (η) is described by an infinite shear viscosity (η_∞), a zero shear viscosity (η_0), a relaxation time (λ), a transition width (a), and a power law index (n).[142]

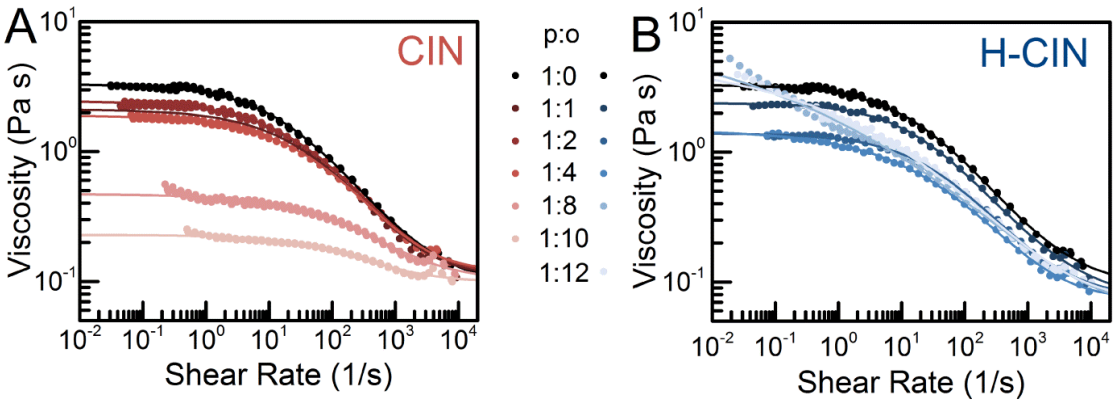

Figure 17: Viscosity curves for MMW CS/PEO systems with varying p:o mass ratios. Viscosity curves of MMW CS/PEO solutions with increasing p:o mass ratios from 1:0 to 1:12 for (**A**) CIN and (**B**) H-CIN. A p:o mass ratio above 1:10 for CIN was not possible due to phase separation.

Both the infinite shear viscosity and the zero shear viscosity decreased as the amount of CIN or H-CIN increased, which was expected based on the LMW CS results from **Figure 16**. At the 1:1 p:o mass ratio, the viscosity curves are almost identical, but as the amount of oil increased the behavior of CIN and H-CIN start to diverge. At the

middle loadings (1:2 and 1:4 p:o mass ratios), CIN has a slightly weaker negative effect on the viscosities. At the highest two oil loadings (1:8 and 1:12 p:o mass ratios), H-CIN begins to thicken again and the zero shear viscosity shifts far to the left. By contrast, at the two highest CIN loadings (1:8 and 1:10 mass ratios), the zero shear viscosity drops substantially and by a p:o mass ratio of 1:10, the curve is nearly flat. When a higher loading of CIN at p:o mass ratio of 1:12 was attempted, we observed severe phase splitting. Additionally, loadings of CIN above a 1:12 p:o mass ratio resulted in the formation of a dynagel, which has been reported by Marin *et al*.[125] Within their work, the minimum CIN:amine group ratio needed to obtain CS gelation was a 22:1 molar ratio, which matches well with our findings of a 21:1 molar ratio. The abnormal behavior of the CIN-loaded solutions can be attributed to the chemical bonding that takes place with CS, this shifts the behavior away from that of a non-interacting oil like H-CIN.

5.4.6 CS/PEO:(CIN or H-CIN) Nanofiber Characteristics

Nanofiber mats containing CIN or H-CIN were successfully electrospun from LMW, MMW, and MOD-MMW CS/PEO solutions as a function of the CS molecular weight, DA, polymer concentration, and p:o mass ratio, **Figure 18**. The polymer concentrations 3.5 and 5.0 w/v% for LMW CS/PEO solutions, as well as 2 and 2.5 w/v% for MMW and MOD-MMW CS/PEO were chosen because they formed smooth cylindrical nanofiber mats without any oil addition, **Figure 15**.

After adding CIN or H-CIN to any CS/PEO solution, an increase in polymer concentration was needed to yield smooth and cylindrical nanofibers. This is expected as the contact angle, **Table 1**, decreased after the addition of CIN or H-CIN, hence leading

to a lower surface tension. Previous studies have reported that a decrease in surface tension leads to nanofibers with bead-on-string morphology.[42] Additionally, as shown in **Figure 16**, both the infinite shear viscosity and the zero shear viscosity decreased as the amount of CIN or H-CIN increased. While the solution properties, such as, polymer concentration and surface tension, can be confounding, viscosity has been reported to be a dictating parameter for electrospinning.[143]

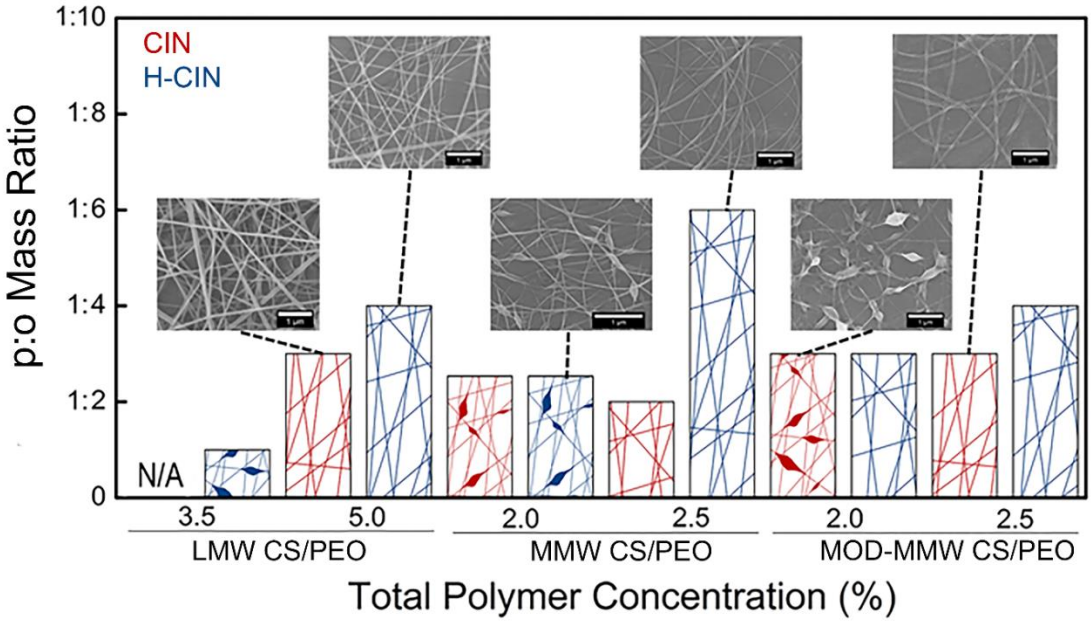

Figure 18: Compilation of nanofiber morphology at varying concentration and p:o ratio. Compilation of the morphology of nanofibers electrospun from LMW, MMW, and MOD-MMW CS/PEO:(CIN or H-CIN) at various p:o mass ratios. N/A indicates that solutions did not form nanofibers when electrospun, cartoons represent that nanofibers with a bead-on-string or cylindrical morphology was formed. SEM micrographs provide representative morphology, all scale bars are 1 μm.

A direct comparison of DA was conducted by electrospinning MMW and MOD-MMW CS/PEO solutions. The 2.5 w/v% MMW CS/PEO solution led to the highest loadings of H-CIN (1:6 p:o mass ratio) suggesting that higher DA improves the stability and electrospinability of H-CIN solutions. A previous report stated that a high DA of 39% increased the stability of carbon nanotubes dispersed in CS, as compared to CS DA values of 7 to 29%.[132] For CIN solutions, the change in DA did not have as large of an effect as on H-CIN solutions. This might be due to the presence of a Schiff base reaction between CIN and CS. Additionally, CIN is 10 times less soluble than H-CIN, which could influence the ability of CS to disperse the oil. In fact, the highest loading of CIN (1:3 p:o mass ratio) that could be electrospun into defect-free nanofibers was achieved using either a 5.0 w/v% LMW CS/PEO solution or a 2.5 w/v% MOD-MMW CS/PEO solution. As expected, the effect of molecular weight on the ability to electrospin oil loaded CS/PEO solutions appeared to be relatively small because all of the polymer concentrations tested were above the C_e. Overall, for successful electrospinning, the DA and molecular weight of CS are parameters that must be tuned based on the oil structure.

5.4.7 Release Characteristics of CS/PEO(CIN or H-CIN) Nanofiber Mats

As a final proof-of-concept, we confirmed that CIN and H-CIN were incorporated into the electrospun nanofiber mats by examining the release of the oils post-electrospinning. A low, 1:0.2 p:o mass ratio, was chosen because both oils could be electrospun for 1 hr from a 5% LMW CS/PEO solution to form robust nanofiber mats that could be handled and tested. UV-Vis quantified that $8.58 \times 10^{-3} \pm 3.8 \times 10^{-3}$ μg of CIN and 1.5 ± 0.5 μg of H-CIN were released from the CS/PEO nanofiber mats after 3 hr. After 48 hr, there was no further release of CIN or H-CIN. The release of CIN is

consistent with our previous work[60] and the difference in release between the two oils is likely due to their unique properties, namely, solubility and/or their chemical interaction with CS. For example, the CIN that has Schiff base reacted with CS likely will not be released from the nanofiber mats within the timeframe of our experiment.

5.5 Conclusion

In this study, the correlation between precursor solution properties and the morphology of CS/PEO and CS/PEO:(CIN or H-CIN) nanofibers was investigated by focusing on CS molecular weight and DA, as well as p:o mass ratio. We have demonstrated that CS/PEO solutions containing a range of CIN and H-CIN p:o mass ratios form nanofibers. An increase in polymer concentration caused a transition from bead-on-string to cylindrical nanofiber morphology, indicating that the addition of oil reduced the solution viscosity. This was corroborated through viscosity stress sweeps. A low DA improved the electrospinning of solutions that contained CIN, while the opposite was observed for solutions that contained H-CIN. When the same p:o mass ratio of CS/PEO to CIN or H-CIN was electrospun into nanofiber mats, there was a 57% higher release of H-CIN than CIN, which was likely a result of oil properties. We suggest that insights gained from electrospinning CIN and H-CIN could be applied to hundreds of additional bioactive essential oils, as well as a variety of small hydrophobic molecules, thus significantly broadening the delivery of therapeutics from electrospun nanofiber mats.

CHAPTER 6

RHEOLOGICAL CHARACTERIZATION OF ANIMAL TISSUES

Adapted from: Jansen, L. E.; Birch, N. P.; Schiffman, J. D.; Crosby, A. J.; Peyton, S. R. Mechanics of Intact Bone Marrow. *J. Mech. Behav. Biomed. Mater.* **2015**, *50*, 299–307.

With excerpts from two additional articles currently in preparation:

Polio, S. R., Aurian-Blajeni, D. E., Birch, N. P., Schiffman, J. D., Crosby, A. J., Peyton, S. R. "Comparative mechanical testing of lung parenchyma" In Preparation

Galarza, S., Mijailovic, A. S., Birch, N. P., Schiffman, J. D., Crosby, A. J., Peyton S. R., Van Vliet, K. J., "Measurement of brain tissue mechanical properties by cavitation rheology" In Preparation

6.1 Abstract

The current knowledge of bone marrow mechanics is limited to its viscous properties, neglecting the elastic contribution of the extracellular matrix. To get a more complete view of the mechanics of marrow, we characterized intact yellow porcine bone marrow using rheology. Porcine lung tissue, muscine brain tissue, and porcine brain tissue were also examined as these tissue also have a gap in their literature values around their response to shear stress. Our analysis shows that all four tissues are primarily elastic. Porcine bone marrow and both brain tissues were found to have a large amount of inter-sample heterogeneity. We found that lung tissue was stiffer than bone marrow and

that the brain tissues were the least stiff. We anticipate the knowledge of the elastic properties of these tissues will elucidate mechanisms involved in disease progression and regenerative medicine.

6.2 Introduction

Bone marrow plays a significant role in body homeostasis by regulating immune and stromal cell trafficking. Researchers have characterized the matrix content and the role of local cells in bone physiology, but capturing the mechanics of bone marrow tissue has been limited in scope. The elastic modulus of engineered substrates is well known to influence cell shape, proliferation, migration and differentiation.[73,144–146] While significant effort has gone into recapitulating the hematopoietic microenvironment *in vitro* for both regenerative medicine and to improve drug screening, there is no physiological measurement of the modulus of intact bone marrow.[147–151] Though some of these model systems incorporate controlled mechanics, there is little validation for the stiffness choices, even though bone marrow stromal and progenitor cells are mechanically responsive to both engineered substrates, and the viscosity of the surrounding fluid.[70–73] Knowing the modulus of *in vivo* tissue is critical for regenerative medicine as well. For example, the Blau lab found that the regenerative capacity of muscle stem cells is enhanced when cultured on surfaces mechanically similar to mouse muscle.[152] This highlights the need for methods that can appropriately characterize the heterogeneous mechanics of bone marrow tissue to understand its role in driving the behaviors of the cells within.

Marrow tissue has hematopoietic-rich and adipose-rich regions, which are referred to as red and yellow marrow, respectively. Yellow marrow is enriched in the

medullary cavity and red marrow in the spongy, trabecular bone.[153–155] Cell content in the marrow is a dynamic process, and yellow marrow can expand and contract as haematopoiesis occurs.[153–155] Unfortunately, the difficulty of harvesting red marrow has limited the ability to isolate and test its mechanics using conventional methods. Yellow marrow has been shown to be mechanically heterogeneous in studies where samples are homogenized and centrifuged to remove cell and bone debris.[35,37] Prepping samples in this manner removes many of the inconsistencies caused when harvesting marrow, but ignores the elastic contribution of the bone marrow extracellular. The most robust study on yellow marrow mechanics measured the viscosity of the marrow from 19 human subjects and found no apparent correlation between age and marrow viscosity, though marrow has been shown to yellow with age.[35,69] Another group found proximal bovine marrow, the tissue close to the trabecular bone, to be more viscous than distal bovine marrow, and they suggest that these changes in viscosity are a function of spatial marrow composition.[36] Though both of these studies are informative, the impact of the surrounding or, potentially inclusive, trabecular bone is neglected because samples were homogenized and filtered.

The anatomical location and surrounding cortical bone poses a unique challenge for researchers interested in mechanically studying bone marrow tissue. Many studies have looked at properties of homogenized marrow, by extracting marrow from the medullary cavity and performing bulk rheology, but these approaches are destructive and create a critical gap in our knowledge of intact marrow mechanics.[33–37] Additionally, researchers have used techniques to measure intramedullary pressure (IMP) to better understand how lifestyle choices, such as loading, disuse, steroid use, and diseases such

as osteoporosis and cancer change marrow content, blood flow, and bone remodeling.[156–160] It is clear that many external factors impact IMP changes, but no work has gone into characterizing the mechanics of the intact matrix, which we suggest plays a stiffness-dependent role in disease progression. Rheology is the dominant method used to characterize bone marrow tissue, with the exception of one group that used ultrasonic wave propagation.[161] However, ultrasonic wave propagation reported that the Young's modulus of bovine marrow is the same order of magnitude as what others have found for the surrounding spongy bone (~2 GPa).[162] The stark differences between marrow and bone likely make it hard to distinguish the marrow mechanics with this type of technique. The characterization of intact bone marrow will improve the understanding of marrow mechanics and make it possible to build more accurate *in vitro* models of marrow tissue.

Alongside our exploration of bone marrow's physical characteristics the same methods were applied to other tissues. Lung tissue has a long history of being characterized with extensional rheology, but very little shear rheology characterization has been done.[31] Mouse and pig brain are much less well explored tissues and even basic data is difficult to find in literature.[32] Characterizing these tissues with shear rheology will render additional insight into the tissues and provide easy comparison to synthetic mimics.

6.3 Materials and Methods

6.3.1 Bone Marrow Rheology

Femurs from grass-fed large black Tamworth Cross pigs, 6-10 months old, were gathered from a local butcher, and mechanical testing was conducted within 2 hrs post-

opening of the bone cavity. Rheology samples were gathered from a bone cut lengthwise down the femur, and tissue samples were biopsy punched out of the medullary cavity and stored in phosphate buffer solution (pH 7.4) for mechanical testing (**Figure 19a**).

Small amplitude oscillatory shear (SAOS) measurements were performed in a Kinexus Pro rheometer (Malvern Instruments, UK) using a plate-plate geometry, with a diameter of 20 mm and gap of 1 mm. Porcine bone marrow punches were placed on the lower plate, the top plate was lowered into position, and excess marrow was trimmed with a razor blade. A solvent trap was placed over the geometry and temperature was maintained at 25 °C. A 0.15% strain was selected from a strain amplitude sweep to ensure that experiments were conducted within the linear viscoelastic region. Oscillatory frequency sweeps were conducted between 0.1 and 16 Hz. To capture temperature variation, samples were heated to 35 °C, and the measurements were repeated. The effective Young's modulus (E^{Eff}) was calculated at a frequency of 0.1 Hz assuming a Poisson's ratio, υ, of 0.5.

$$E^{Eff} = 2G^*(1+\upsilon) \qquad \textbf{Equation 5}$$

6.3.2 Brain Rheology

Muscine and porcine brain samples were obtained from the Peyton research group. SAOS measurements were performed on the Kinexus Pro rheometer using a plate-plate geometry with a plate diameter of 8 mm and a gap of 1 mm. Muscine brain sections were placed on the lower plate, the top plate was lowered into position, and excess tissue was trimmed with a razor blade. Porcine brain sections were punched to 8 mm from a larger sample and then loaded as above. No solvent trap was used due to the small plate

diameter and experiment time was limited to 15 minutes to limit drying. A 0.5% strain was as before and oscillatory frequency sweeps were conducted between 0.1 and 1 Hz.

6.3.3 Lung Rheology

Porcine lung samples were obtained from the Peyton research group. SAOS measurements were performed on the Kinexus Pro rheometer using a plate-plate geometry with a plate diameter of 20 mm and a gap of 2.5 mm. Porcine lung sections were placed on the lower plate, the top plate was lowered into position, and excess tissue was trimmed with a razor blade. A solvent trap was placed over the geometry and temperature was maintained at 25 °C. A 0.5% strain was selected as before and oscillatory frequency sweeps were conducted between 0.1 and 1 Hz.

6.3.4 Statistical Analysis

Statistical analysis was accomplished using Graphpad's Prism v5.0a. Data are reported as mean ± standard error. Statistical significance was determined by a one-way analysis of variance (ANOVA) followed by a Tukey's multiple comparisons test. When noted, a two-tailed t-test was used. P-values <0.05 are considered significant, where $p<0.05$ is denoted with *, ≤ 0.01 with **, ≤ 0.001 with ***, and ≤ 0.0001 with ****.

6.4 Results and Discussion

We harvested intact marrow, with minimal post-mortem time, from 6-10 month old pigs. Pig was chosen as a model organism because of their anatomical similarity to humans, and their widespread use as sources for biological materials and as subjects for medical device testing.[163,164] Further, the pig model allowed us to examine tissue-scale mechanical heterogeneity absent of many convoluting factors, such as age, diet, and race. Samples were prepared by removing biopsy punches from the inner medullary cavity

(**Figure 19a**). SAOS rheology measures the bulk properties of a biopsy punch placed between two oscillating parallel plates (**Figure 19b**).

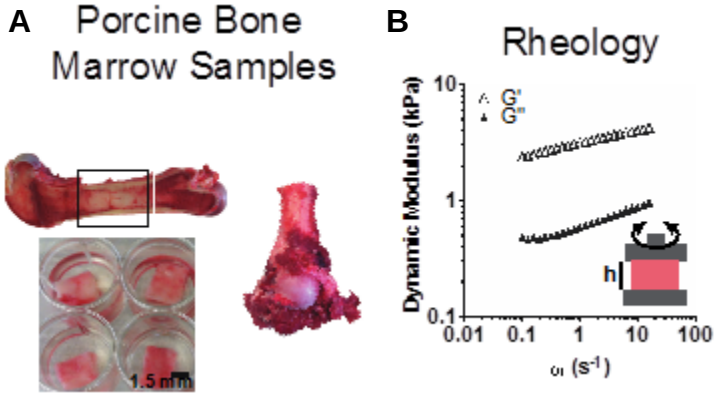

Figure 19: Techinques for characterizing porcine bone marrow and dynamic moduli thereof. Techniques used to characterize porcine bone marrow. **A:** Samples were removed from the medullary cavity of femurs for characterization. **B:** Rheology measurements were done between two parallel plates to obtain a storage (*G'*) and loss (*G''*) modulus with respect to increasing shear.

6.4.1 Bone marrow is a benign tissue with dominant elastic contributions

We used bulk rheology to quantify the viscoelastic properties of bone marrow tissue. The dynamic moduli are frequency dependent, and the dynamic storage modulus is consistently an order of magnitude larger than the dynamic loss modulus (**Figure 20a**). Rheology was the only instrument with temperature control, and, as the temperature was increased to 35 °C, both the dynamic moduli and complex viscosity decreased by an order of magnitude. The complex viscosity decreased as shear rate increased, indicating that bone marrow behaves as a non-Newtonian fluid (**Figure 20b**). Power law indices of

0.15±0.01 for 25 °C and 0.12±0.02 for 35 °C determined that bone marrow is a benign material with dominant elastic contributions to its mechanical response.

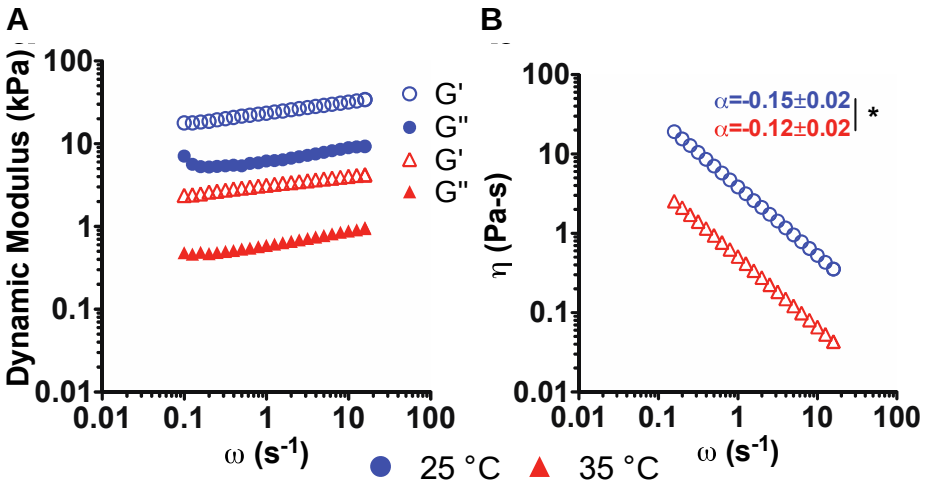

Figure 20: Rheological behaviour of porcine bone marrow. A: Representative rheological data. The storage (*G'*, open symbol) and loss (*G"*, closed symbol) modulus versus strain rate show a weakly frequency dependent material with a dominant elastic modulus. As temperature is increased from 25 °C (blue) to 35 °C (red), both modulus and **B:** complex viscosity decrease, indicating strong temperature dependence. The power law (α) fit of the complex viscosity showed that bone marrow is slightly more elastic at the higher temperature (t-test, *p<0.05).

6.4.2 Porcine bone marrow has inter -sample heterogeneity

The effective Young's modulus of the bone marrow was strongly temperature dependent. The moduli ranged from 0.73-135.6 kPa at 25°C and 0.1-10.9 kPa at 35°C (**Figure 21**). The effect of harvest location in the medullary cavity was explored. There was no significant difference in effective Young's modulus between the samples from the

distal and proximal end of a single bone. This suggests the apparent inter-sample heterogeneity is not due to harvest location.

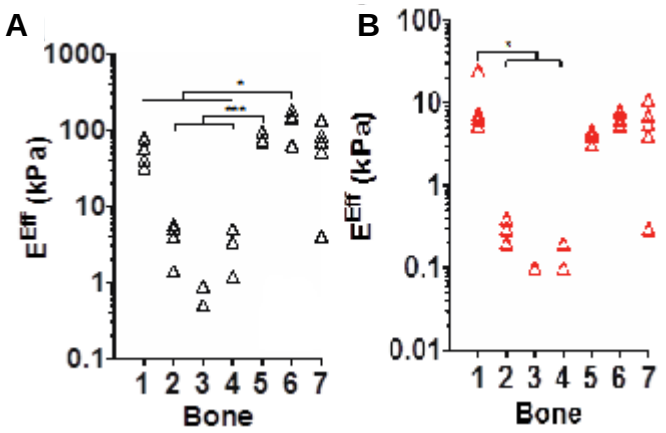

Figure 21: Bone marrow exhibits inter-sample heterogeneity. The effective Young's modulus (E^{Eff}) for **A:** 0.1 Hz at 25°C and **B:** 0.1 Hz at 35°C. The effective Young's Modulus (E^{Eff}), calculated at 0.1 Hz, is an order of magnitude lower than at 25°C, but inter-sample heterogeneity is still present. Data points represent different locations within the same bone sample. Statistical significance was calculated using the mean of the data (*P<0.05, ***P<0.001).

A goal of tissue engineering is to recapitulate key features of tissues *in vitro* in order to better understand *in vivo* phenomena and apply this toward directing tissue function. The mechanical properties of a cell's microenvironment have been shown to dictate the migration and differentiation of marrow-derived mesenchymal stem cells, but little research has been conducted on mechanically characterizing bone marrow tissue.[70,73,165] Here, we report that bone marrow is a benign viscoelastic tissue with a dominant elastic contribution and significant inter-sample heterogeneity.

Our dynamic moduli are much stiffer and encompass a larger range of values than earlier studies. However, as previously noted, other studies have been performed on homogenized tissue samples, so the reported viscosities ranging from of 44.6-142 mPa•s cannot be easily compared to our viscous data (range from 100-500 Pa•s).[33–37] Intact bone marrow tissue has an effective Young's modulus ranging from 0.25-24.7 kPa at physiological marrow temperature (35°C).[166] The only other report of rheology on intact marrow found that bovine marrow has a dynamic storage modulus of ~220 Pa at a frequency of 1.6 Hz and temperature of 37 °C.[167] At this same frequency, but at 35 °C, our porcine samples had a dynamic storage modulus ranging from 23-10,000 Pa (data not shown). This study is consistent with the storage magnitude we report for intact marrow, but because their project was confined to 3 samples from the same bone, this limited their ability to capture biological heterogeneities in marrow samples. We found intact marrow to have a large amount of inter-sample heterogeneity, and this is not surprising because biological tissues are known to be heterogeneous (**Figure 21a**). For example, reports on the elastic modulus of brain and lung tissue can range from 0.1-10, and 1.5-100 kPa, respectively.[35,168–173] While it is more likely that these variations are due to structural components of the tissues, it was also important to validate that the array of mechanical tests used to gather these values was not the source of this heterogeneity, as we have done here. The effective modulus of porcine marrow was strongly temperature-dependent, the tissue remained with a dominant elastic contribution at all temperatures tested (i.e. power law held at ~0.15) (**Figure 21b**).

6.4.3 Lung tissue is a benign elastic material

Bulk rheology was also used to measure the viscoelastic properties of porcine lung tissue (**Figure 22**). The storage modulus is consistently higher than the loss modulus, however the difference is much less than in bone marrow. Initial rheology of samples at 37 °C was performed, but no temperature effects were observed. Complex viscosity decreased as shear rate increased, indicating non-newtonian behavior. 88 samples from 7 lungs were used to calculate an average Young's modulus (at 0.1 Hz and 25 °C) of 3000 ± 72 Pa. While the benign elastic behavior is similar to that of bone marrow, the stiffness of the material is significantly higher. Inter-sample heterogeneity was also markedly lower.

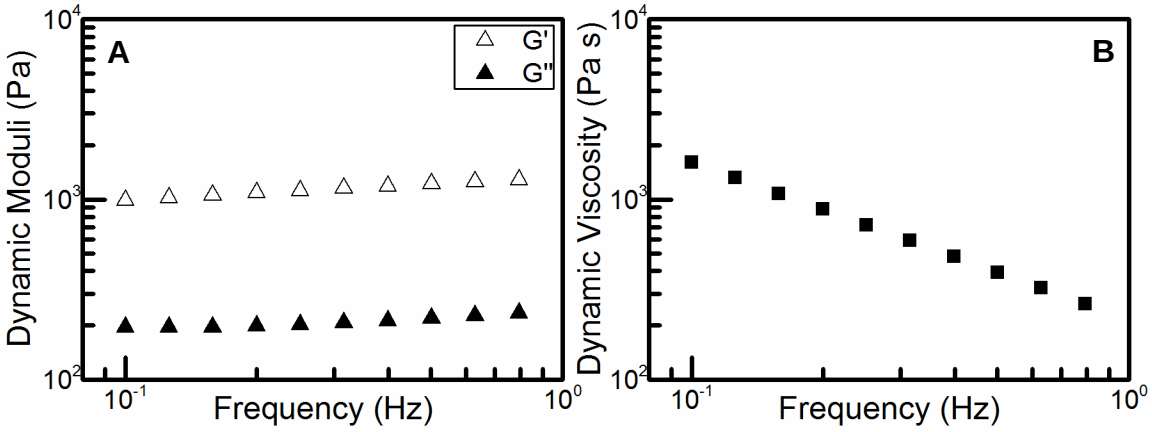

Figure 22: Rheological behavior of porcine lung tissue. A: Representative rheological data. The storage (*G'*, open symbol) and loss (*G"*, closed symbol) modulus versus strain rate show a weakly frequency dependent material with a dominant elastic modulus. **B:** Complex viscosity data shows a similar trend.

6.4.4 Porcine and muscine brain tissue are benign elastic materials

Muscine brain tissue was also characterized with bulk rheology (**Figure 23)**. The dynamic moduli were found to be frequency independent with the storage modulus being slightly higher than the loss modulus. No experiments were conducted at elevated temperature due to the time limits imposed by sample dehydration. The complex viscosity decreased with increasing frequency indicating non-Newtonian behavior. 25 samples from 11 brains were used to calculate an average Young's modulus (at 0.1 Hz and 25°C) of 979 ± 786 Pa. Inter-sample heterogeneity was higher than in the lung tissue but similar to the results from bone marrow. Overall the mouse brain tissue was found to be softer than lung tissue but stiffer than bone marrow.

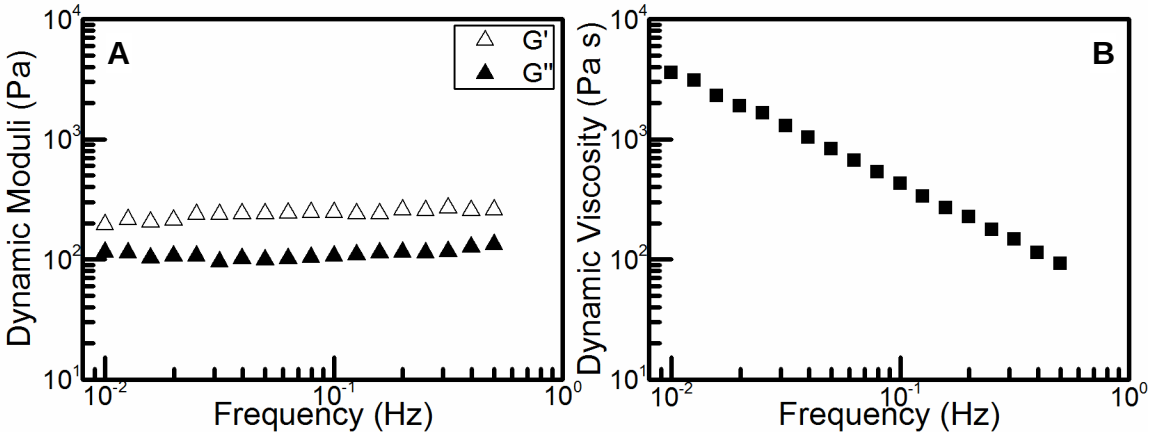

Figure 23: Rheological behavior of muscine brain tissue. A: Representative rheological data. The storage (*G'*, open symbol) and loss (*G"*, closed symbol) modulus versus strain rate show a weakly frequency dependent material with a dominant elastic modulus. **B:** Complex viscosity data shows a similar trend.

Porcine brain tissue was the final tissue examined with rheology (**Figure 24)**. The dynamic moduli were found to be frequency independent and similar in magnitude.

Complex viscosity decreased with increasing frequency similar to the other measured tissues. 24 samples from 5 porcine brains were used to calculate an average Young's modulus (at 0.1 Hz and 25 °C) of 693 ± 374 Pa. Inter-sample heterogeneity was found to be similar to that in muscine brain tissue. Porcine brain tissue was observed to be slightly but not significantly softer than muscine brain. This is likely due to the way samples were obtained and the inclusion of more connective tissue in the mouse brain samples.

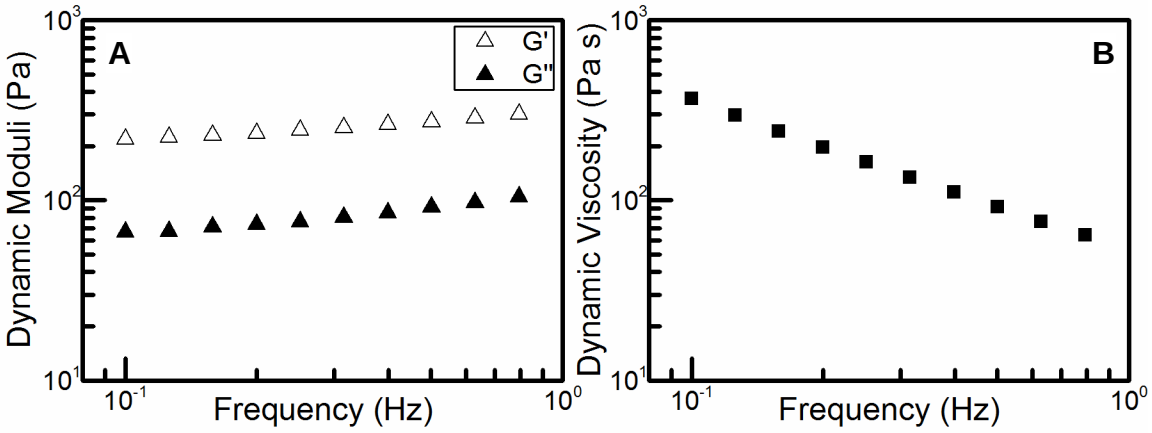

Figure 24: Rheological behavior of porcine brain tissue. A: Representative rheological data. The storage (*G'*, open symbol) and loss (*G"*, closed symbol) modulus versus strain rate show a weakly frequency dependent material with a dominant elastic modulus. **B:** Complex viscosity data shows a similar trend.

6.5 Conclusion

Intact bone marrow, porcine lung tissue, and two types of brain tissue were mechanically characterized and found to be benign viscoelastic materials. Also, we are the first to report that all four tissues have dominant elastic contribution when the tissue is intact. We also stress that all four tissues were heterogeneous, and there may not one,

but a range of appropriate moduli values. Overall, this type of thorough characterization can be used to improve upon current studies of bone marrow tissue elasticity and gain new insights into tissue function and structure.

CHAPTER 7

RHEOLOGICAL CHARACTERIZATION OF ANTIFOULING PEGDMA-POLYDOPAMINE HYDROGELS

Adapted from an article currently in preparation:

Kolewe, K. W., Birch, N. P., Mako N., Schiffman, J.D. "Antifouling hydrogels: Synergy of chemical and mechanical properties" In Preparation.

7.1 Abstract

Bacterial fouling in catheters is a major source of hospital-acquired infections. By depositing proteins onto catheter surfaces, bacteria can travel deep into the body and cause grave harm. Zwitterionic systems are adept at reducing bacterial fouling, however many zwitterionic systems to date have been too soft for effective use. In this section, we seek to prove that we have used a zwitterionic crosslinker to produce gels stiffer than ~1 kPa. We first established a group of three poly(ethylene glycol) dimethacrylate (PEGDMA) systems, the softest barely meeting our goal, the next an order of magnitude stiffer, and the final being two orders of magnitude stiffer than our goal. The three systems were then crosslinked with polydopamine and characterized. Polydopamine did not reduce mechanical properties and, in the stiffest case, improved stiffness. We suggest that these three crosslinked systems could provide a powerful basis for building antifouling catheter coatings.

7.2 Introduction

The materials used in the design of polymeric catheters aim to prevent the fouling of the device through bacteria (infection) and proteins (thrombosis). Catheters are frequently coated with hydrogels to improve patient comfort while delaying bacterial infections through antiadhesive properties. Hydrophilic polymers are class of passive antifouling materials that resist non-specific protein adsorption and limit bacterial adhesion, poly(ethylene glycol) (PEG) is the most widely used of these.[174] The non-specific protein adsorption resistance of PEG is attributed largely to the development of a hydration layer in the presence of water.[175,176] The major drawback of PEG is stability, in the presence of oxygen PEG coatings will auto-oxidize into aldehydes and ethers.[177] Zwitterionic polymers have emerged as a promising class of antifouling polymers with enhanced stability and excellent fouling resistance. Zwitterions, like PEG, resists protein adsorption through the formation of a hydration boundary layer at the surface.[178,179]

Synergistically making a soft surface that expresses zwitterionic surface chemistry should resist bacterial adhesion most effectively, however not all applications can be performed using super soft, ~1 kPa, hydrogels. Therefore incorporating the zwitterion into the hydrogel network as a second crosslinked network could provide chemical functionality without sacrificing mechanical strength. The enhanced strength and stability of double-network (DN) hydrogels are advantageous to conventional single-networks due to enhanced toughness and mechanical strength of the composite hydrogel.[180] In these systems a brittle hydrophillic network forms the backbone of the system that expands when swollen, allowing a second monomer to polymerize in excess within the matrix.[181]

In this work we incorporate a covalently crosslinked polydopamine (PDA) – poly(2-methacryloyloxyethyl phosphorylcholine) (PMPC) network into a poly(ethylene glycol) dimethacrylate (PEGDMA) backbone to create more stable double network hydrogels with enhanced stability and optimal antifouling performance. PEGDMA hydrogels were synthesized over a wide range of storage modulus (2 - 660 kPa) and DN hydrogels were successfully formed through the diffusion of PDA-PMPC. The diffusion and polymerization of the PDA-PMPC complex throughout the PEGDMA backbone was uniform on standard ~150 μm hydrogels creating a homogeneous DN hydrogel. These DN composites showed enhanced, up to 90%, antifouling performance compared to PEGDMA hydrogels when challenged with *Escherichia coli* and *Staphylococcus aureus* over 24 hr incubation periods. We suggest improving the performance of catheter coatings through the inclusion of PDA-PMPC.

7.3 Experimental

7.3.1 Materials

All compounds were used as received. Poly(ethylene glycol) dimethacrylate, (PEGDMA, M_n = 750 Da), dopamine hydrochloride (PDA), 3-(trimethoxysilyl)propyl methacrylate, ampicillin (BioReagent grade), chloramphenicol (BioReagent grade), M9 minimal salts (M9 media), D-(+)-glucose, calcium chloride (anhydrous), phosphate buffered saline (PBS, 1× sterile biograde), tryptic soy broth (TSB), Luria-Bertani broth (LB), and Bradford reagent were purchased from Sigma-Aldrich (St. Louis, MO). Irgacure 2959 was obtained from BASF (Ludwigshafen, Germany). Magnesium sulfate anhydrous and molecular grade agar were obtained from Fisher Scientific (Fair Lawn,

NJ). Deionized (DI) water was obtained from a Barnstead Nanopure Infinity water purification system (Thermo Fisher Scientific, Waltham, MA).

7.3.2 Fabrication of PDA-PMPC-PEGDMA Hydrogels

PEGDMA hydrogels were prepared using previously established protocols.[182] Briefly, 7.5%, 25%, and 50 vol% PEGDMA in 1 M PBS solution was sterile filtered using a 0.2 μm syringe, then degassed using nitrogen gas. For UV-curing the radical photo initiator, 0.8 wt% Irgacure 2959 was added to the polymer precursor solution with induction under a long wave UV light, 365 nm for 10 min. PEGDMA solution (75 μL) was sandwiched between two 22-mm UV-sterilized coverslips (Fisher Scientific) functionalized with 3-(trimethoxysilyl)propyl methacylate.[183] Fabricating the hydrogel between coverslips enabled all hydrogels to have a uniform thickness and limited the oxygen exposure. Following polymerization, the top coverslip was removed using forceps before the PEGDMA hydrogels were swollen in PBS for 48 hr before functionalization via the codeposition of PDA and poly(2-methacryloyloxyethyl phosphorylcholine) (PMPC), which was synthesized as previously described.[184,185] PEGDMA hydrogels were placed in 6-well polystyrene plates containing 5 mL of Tris buffer (10 mM, pH 8.5) containing 2 mg/mL of both PDA and PMPC for 6 h. Next, all hydrogels were washed 3 times with DI water to remove residual polymer before being placed in a fresh multi-well plate with DI water until further testing.

7.3.3 Characterization of Hydrogels

Small amplitude oscillatory shear measurements were performed on PEGDMA and PDA-PMPC PEGDMA hydrogels using a Kinexus Pro rheometer (Malvern

Instruments, UK) using a plate–plate geometry, with a diameter of 20 mm and a gap of 1 mm. All hydrogels were prepared for rheology using 1 mm deep Teflon molds that had a 25 cm diameter. Hydrogel punches were loaded into the rheometer and then trimmed to size with a razor. A strain amplitude sweep was performed to ensure that experiments were conducted within the linear viscoelastic region and a strain percent of 0.01% was selected. Oscillation frequency sweeps were conducted over an angular frequency domain of 0.6 and 315 rad/s.

7.4 Results and Discussion

7.4.1 Characteristics of Surface Functionalized Hydrogels

PEGDMA hydrogels were successfully synthesized over a broad range of mechanical properties as determined through rheology, **Figure 25**. We classified these hydrogels into 3 classes based on storage modulus, soft (7.5% PEGDMA, 1.7 kPa), intermediate (25% PEGDMA, 240 kPa), and stiff (50% PEGDMA, 660 kPa). The gels were dominated by frequency independent elastic moduli. The viscous moduli were significantly lower and showed significant frequency dependence. As expected, the magnitude of all the dynamic moduli were directly related to the polymer concentration. Hydrogel stiffness is intrinsically tied to the crosslink density within the network. Increasing crosslink density limits the diffusivity of solutes through the network. The mesh size, theoretical distance between crosslinks, was characterized for each hydrogel concentration: 34.3 ± 1.5 Å, 19.3 ± 0.4 Å, and 10.0 ± 1.0 Å for 7.5%, 25%, and 50% PEGDMA respectively.

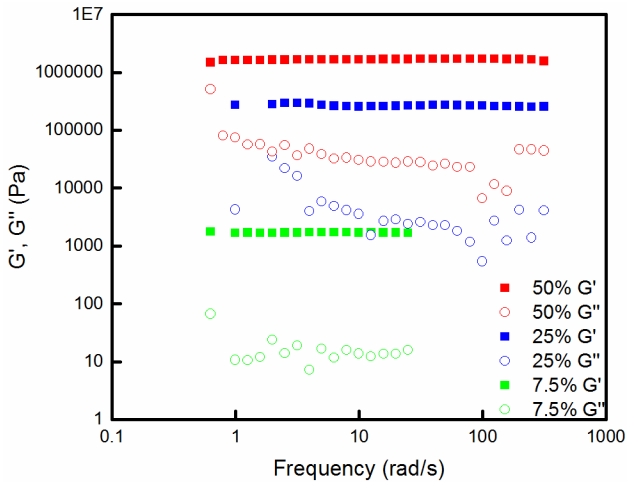

Figure 25: Frequency behavior of the dynamic moduli of three PEGDMA systems. Frequency sweeps determined the elastic (G') and viscous (G") moduli of PEGDMA hydrogels as a function of polymer concentration. Frequency independent G' dominated all three gels, indicating that the hydrogel is highly elastic. G" displayed strong frequency dependence, most likely due to the high water content. The dynamic moduli were strongly correlated with the increasing polymer concentration.

These PEGDMA hydrogels were then functionalized with a self-polymerizing super hydrophilic coating of PDA and PMPC to enhance the functionality of PEGDMA hydrogels without sacrificing mechanical integrity. PDA polymerization is accompanied by a distinct brown pigmentation so solute diffusion experiments can be performed tracking the depth of color penetration. The diffusion of PDA-PMPC throughout the hydrogel was dependent on the mesh size of the hydrogel and the thickness of the sample. Full penetration of PDA polymerization throughout the hydrogel is limited by PDA aggregation during polymerization, oligomers aggregate through π-π stacking into small 1-2 nm particles before continuing to stack into large micron size particles. [186] As expected the low crosslink density of 7.5% PEGDMA, 34 Å, provided no barrier to diffusion while 25% PEGDMA, 19 Å, slowed but didn't prevent complete diffusion. The

dense crosslinking of 50% PEGDMA however creates a theoretical spacing, 10 Å mesh, on the same length scale as the 1-2 nm PDA aggregates. Diffusion experiments on 50% PEGDMA on thick (25 mm diameter, 2 mm height) displayed clear diffusion limitations as a defined dark shell formed. Similar diffusion experiments on thin hydrogels displayed no limitations as these dimensions (22 mm diameter, 125 μm height) effectively led to complete 1D diffusion.

To characterize the mechanical integrity of hydrogels following PDA-PMPC polymerization, rheological studies were performed as before on thick 2 mm hydrogels. Ideally, integrating a second polymer network into the hydrogel will either improve or maintain mechanical strength without sacrificing stability.[181] Soft (7.5%) PEGDMA hydrogels displayed no discernable difference in storage modulus following PDA-PMPC polymerization, **Figure 26A**. Similarly, intermediate (25%) PEGDMA displayed minimal variation in storage modulus over a frequency sweep from 1 to 100 hz, **Figure 26B**. Densely crosslinked stiff (50%) PEGDMA however, displayed a clear increase in storage modulus from 660 kPa to 1700 kPa, **Figure 26C**. This substantial increase is attributed to the shell formation around the hydrogel exterior caused by the dense crosslinking of PEGDMA at this concentration. To understand whether mechanical enhancement occurred without the sacrifice of hydrogel stability, swelling experiments were performed. The degree of swelling was characterized through *Q*, the ratio of equilibrium swelling rate vs dry polymer weight. There was an insignificant loss of hydrogel swelling following PDA-PMPC polymerization likely due to the hydrophilicity of PMPC. The polymerization of PDA-PMPC in PEGDMA hydrogels enhances the mechanical

properties without sacrificing the desirable intrinsic swelling properties of PEGDMA hydrogels.

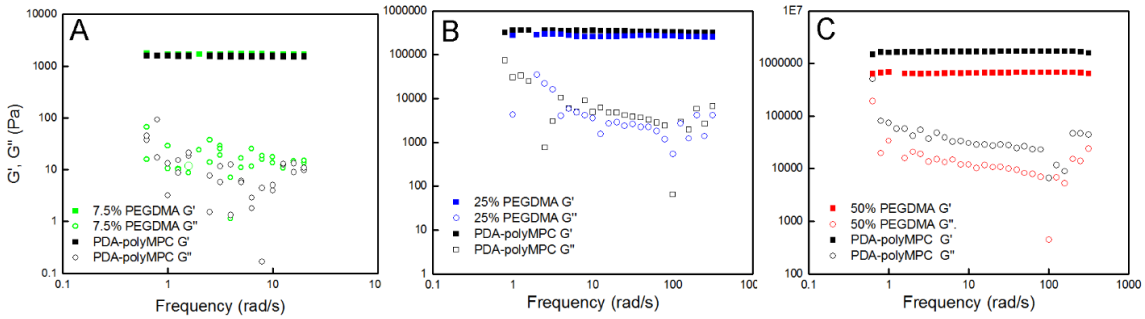

Figure 26: Frequency behavior of three cross-linked PEGDMA-PMPC systems. Bulk mechanical properties of PDA-PMPC hydrogels. The separation of frequency sweeps in storage (G') and loss (G") moduli indicate diffusion induced heterogeneity of highly crosslinked hydrogels. In low (7.5%) polymer concentration (a) the mechanical properties of the hydrogel system are unaffected by the inclusion of coating complex. At intermediate (25%) concentration minimal variation exists between PEGDMA and PDA-PMPC PEGDMA hydrogels. Diffusion limited stiff (50%) hydrogels exhibit a distinct increase in storage and loss modulus across multiple samples indicating the influence of a core-shell coating structure due to limited diffusion of the PDA-PMPC complex through the fine (10.0 ± 1.0 Å) network.

7.5 Conclusion

With a simple oxidation polymerization reaction PDA-PMPC can be easily introduced into PEGDMA hydrogels to form a stable second network that significantly enhances antifouling performance without sacrificing mechanical strength or swelling characteristics. Hydrogels were produced across a wide tunable range from soft (1.7 kPa)

to stiff (660 kPa). We suggest that these hydrogels hold potential as antifouling coatings for catheters and other medical devices.

CHAPTER 8

SELF-ASSEMBLED ANTIBACTERIAL METAL NANOPARTICLES IN ALKYD-BASED PAINTS

Adapted from an article currently in preparation:

Birch, N. P., Kolewe, K. W., Digiovanni, T., Champagne, V. K., Schiffman, J. D. "Self-assembled antibacterial metal nanoparticles in alkyd-based paints" In Preparation

8.1 Introduction

Antibacterial and antifouling coatings have potential applications across many fields. Heavy metals like cobalt, copper, iron, and zinc have long been used as a source of antibacterial properties, with copper and zinc being much more effective antibacterial agents.[66,187] These ions have been used as the core of nanoparticles (NPs), ex. copper-chitosan and zinc-chitosan NPs,[20,66,188] loaded into hydrogels,[189] and coated on films.[190] Recently, pre-synthesized silver nanoparticles have become a popular antibacterial additive.[191] Simplifying this two-step synthesis into a single step would make for a greener process and a more desirable product.

Previously, only one study has explored the notion of self-assembling metal nanoparticles within an alkyd resin. The study only explored gold and silver nanoparticles and conducted minimal antibacterial testing.[192] In our system, one of four common industrial metal naphthenates (Cu, Zn, Co, Fe) is used to catalyze the oxidative crosslinking of fatty acids present in akyld-based paints into a nanoparticle containing

resin (**Figure 27**).[192] We will demonstrate the presence of nanoparticles, effective diffusion of metal ions from the resins, and the antibacterial activity of resin coated surfaces.

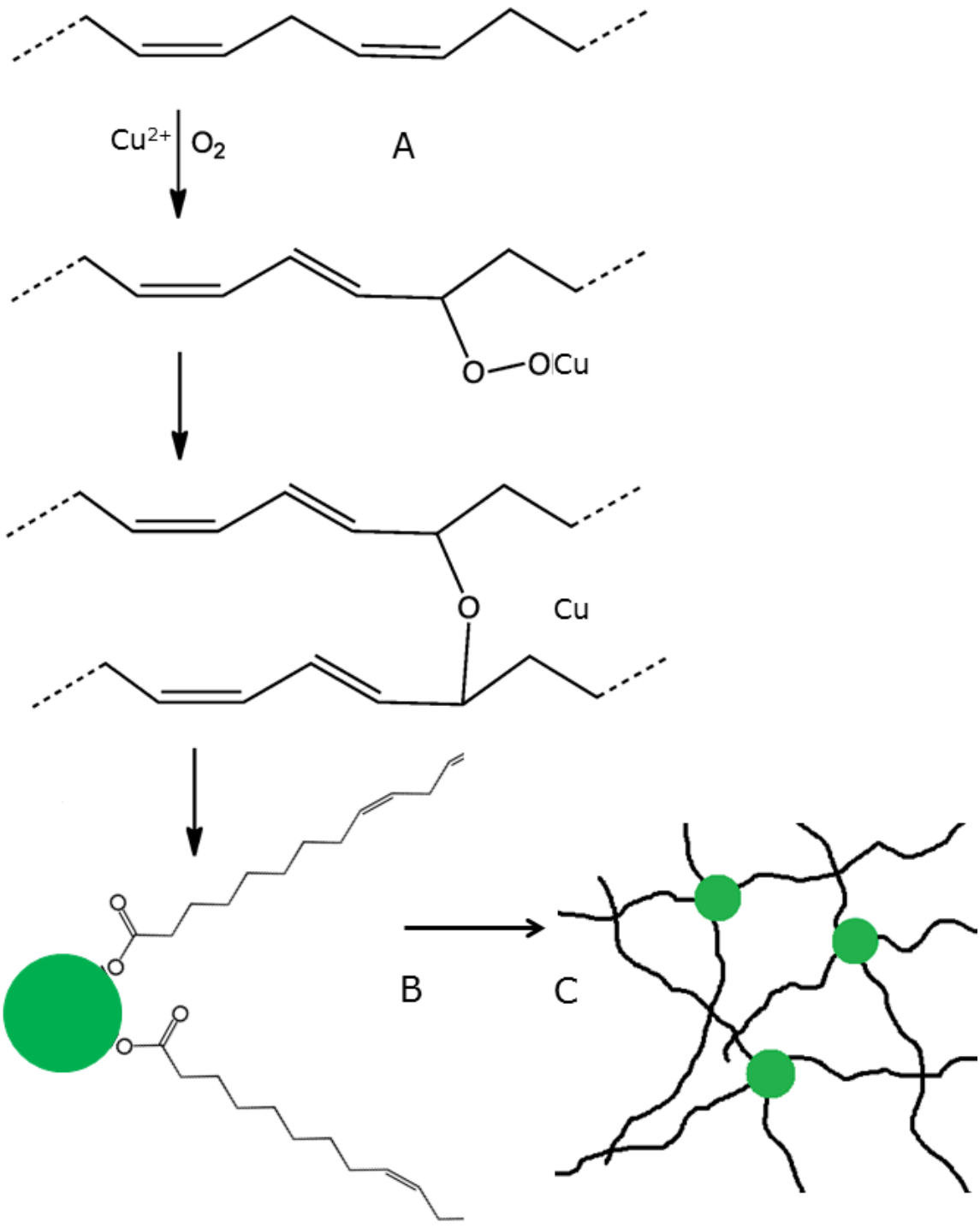

Figure 27: Divalent metal ions catalyze the oxidative crosslinking of linoleic acid and similar fatty acids. (A). The carboxylic acids present on the ends of the fatty acids are able to cap the metal nanoparticles that are a byproduct of the crosslinking (B). The result

is a cross-linked resin with integral metal nanoparticles that can be used to provide antibacterial activity (C).

8.2 Experimental

8.2.1 Materials

Minwax® antique oil finish was used as the base alkyd paint for all experiments. Copper(II) naphthenate (77% in mineral spirits), zinc naphthenate (65% in mineral spirits), cobalt naphthenate (53%), and iron naphthenate (80%) were obtained from Strem Chemicals (Newburyport, MA). Quality control standard 21 was sourced from Perkin Elmer (Waltham, MA). Nitric acid (69.2%) was sourced from Fisher Scientific (Fairlawn, NJ). ReagentPlus grade cobalt(II) sulfate heptahydrate (≥ 99%), copper(II) sulfate pentahydrate (≥98.0%), iron(II) sulfate heptahydrate (≥ 99%), zinc sulfate heptahydrate (≥ 99%) were obtained from Sigma Aldrich (St. Louis, MO). Ionic strength adjuster (ISA) and cupric standard (0.1M) were purchased from Thermo Scientific (Chelmsford, MA). Deionized (DI) water was obtained from a Barnstead Nanopure Infinity water purification system (Thermo Fisher Scientific, Waltham, MA).

8.2.2 Film Preparation

Metal-loaded paint was prepared by mixing 2 g of alkyd paint (Minwax® antique oil finish) with enough metal naphthenate to result in a 0.27 % w/w metal concentration. The solution was mixed until homogenous. 0.5 g of solution was then poured into a 6 cm diameter polystyrene weigh boat and allowed to cure for 2-3 days. Films were removed from the polystyrene and used for subsequent testing.

8.2.3 Copper Diffusion

The diffusion of copper ions into aqueous solution was measured using an Orion Star A214 ISE meter with an ionplus Sure-Flow Cupric probe (Thermo Fisher Scientific, Tewksbury, MA, USA). Samples were submerged in 50 mL of 10^{-5} M nitric acid. 1 mL of ISA was added to keep the ionic strength constant. Three samples were measured over the course of 60 days. The data were fit with an equation described later in the text (**Equation 6**).

8.2.4 ICP-MS

The diffusion of copper, zinc, cobalt, and iron ions into aqueous solution were measured at 7 days, 15 days, and 30 days with inductively coupled plasma mass spectrometry (ICP-MS). Samples were submerged in 50 mL of 10^{-5} M. 1 mL of ISA was added to keep the ionic strength constant. An aliquot of 10 uL were digested with 0.5 mL of fresh aqua regia for 15 min. The digested samples were diluted to 10 mL with de-ionized water. A series of ICP-MS Quality Control standard 21 (QC 21) solutions (0, 0.2, 0.5, 1, 2, 5, 10, 20 ppb) were prepared and digested with 0.5 mL aqua regia. The QC 21 standard solutions and the sample solutions were measured on an Elan 6100 ICP mass spectrometer (PerkinElmer SCIEX, Waltham, MA). A calibration curve was drawn from the results obtained for standard solutions. The amount of the elements Co, Cu, Fe, and Zn in the sample solutions were calculated from the calibration curve and the signal obtained from ICP-MS. The instrument was operated with 1550 W RF power and the nebulizer Argon flow rate was optimized at 0.96 L/min.

8.2.5 Antibacterial Activity

Metal loaded paints and metal-free controls were placed at the base of separate wells in 6-well polystyrene plates (Fisher Scientific) and inoculated with 5 mL of *E. coli* suspension in M9 minimal media to a final concentration of 1×10^8 cells/mL. Plates were incubated at 37 °C for 2 hr under static conditions. Samples were then stained with propidum iodide (PI) for 5 min, washed, and immediately imaged. Live/Dead assessment was performed using established protocols where green fluorescent protein (GFP) containing cells (green) are considered alive and PI stain cells are considered dead (red).

8.2.6 MIC

Minimum inhibitory concentration (MIC) was determined for copper, zinc, cobalt, and iron metal ion solutions based on a previously outlined procedure.[193] An overnight culture of E. coli K12 was prepared in Muller Hinton Broth (MHB). A Fisherbrand polypropylene 96-well plate was filled with an increasing concentration gradient of copper sulfate pentahydrate, zinc sulfate heptahydrate, cobalt sulfate heptahydrate, and iron sulfate heptahydrate. The concentrations of the copper sulfate pentahydrate, zinc sulfate heptahydrate, cobalt sulfate heptahydrate solutions started at 2 µg/mL of metal ion and doubled at each well until 1024 µg/mL. The iron sulfate heptahydrate started from 8 µg/mL of metal ion and doubled until 4096 µg/mL. In the row below each test, metal ion solutions without any bacteria were used as baselines to determine to absorbance of the metal ion solutions. Two columns of the well plate remained controls: the growth control contained MHB and bacteria and the sterile control contained only MHB. After the well

plate incubated (37 °C) for 20 hr, the bacteria concentrations in each well were measured using an absorbance microplate reader at an absorbance of 600 nm.

8.3 Results and Discussion

Transmission electron microscopy was conducted on all four metal-loaded paint types to confirm the successful synthesis of nanoparticles. As expected, the bulk of the particles were smaller than 30 nm, consistent with previous literature.[192] In the copper-loaded system, a large number of sub-100 nm aggregates were observed. We found that the zinc-loaded system was comprised of small spherical and slightly irregular particles, no aggregation was observed. The cobalt-loaded system included larger oblong nanoparticles. The iron nanoparticles that were generated were consistently small and spherical in shape. As smaller nanoparticles have a higher surface area, small stable nanoparticles are desirable to provide a high flux rate of antibacterial metal ions to the surface of the films. To test the magnitude of these effects, diffusion testing was carried out.

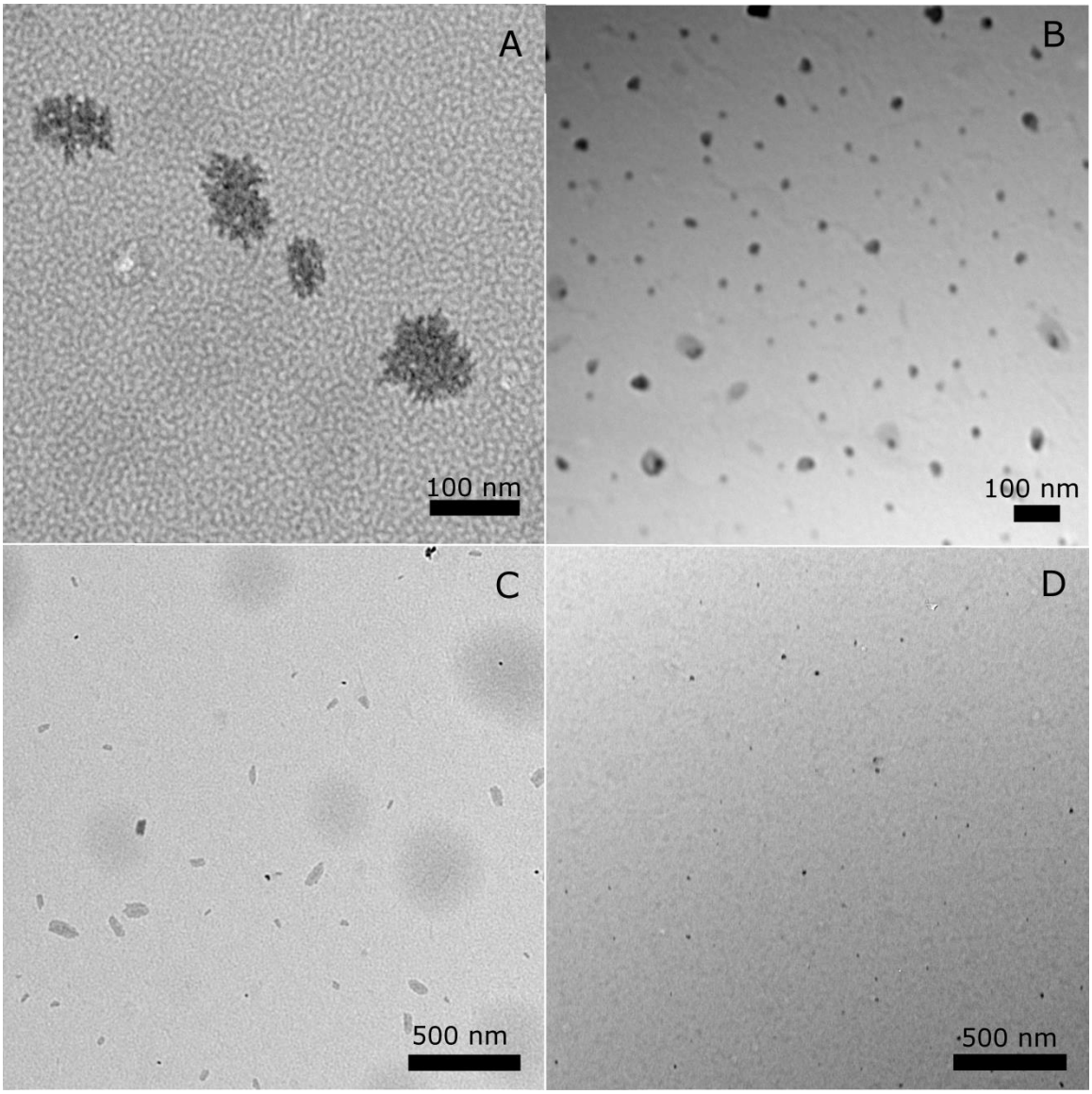

Figure 28: Representative TEM micrographs of each metal nanoparticle type. Copper samples were found to contain large aggregates of smaller nanoparticles (A). Zinc samples for small and regular nanoparticles. (B). Cobalt samples contained larger oblong particles but no large aggregates (C). Iron samples contained no aggregates and nanoparticles were regular and small (D).

8.3.1 Diffusion of metal ions from as-synthesized paints

Copper was the only metal ion of the four used that could be measured using an ion selective electrode. Copper levels were measured every few days with a selective ion probe and were found to rapidly reach an equilibrium metal ion concentration (**Figure 29A**). The data were fit to an empirical formula described below as **Equation 6**. In this equation the concentration is described by the equilibrium concentration (C_{eq}), a rate constant (k), and the elapsed time in days (t). For copper C_{eq} was found to be 6.6*10^{-5} M and k was determined to be 0.093. This gives the diffusion a half-life of 7.5 days.

$$C = C_{eq} * (1 - e^{-kt}) \qquad \textbf{Equation 6}$$

All four metal ions were able to be detected via ICP-MS and their diffusion at 15 and 30 days was measured (**Figure 29B**). While the measured values were slightly different, the trends were identical, with copper and cobalt quickly reaching equilibrium. Iron diffusion was found to be two orders of magnitude below that of the other metals. Zinc diffusion was roughly double that of copper but with a much longer equilibration time.

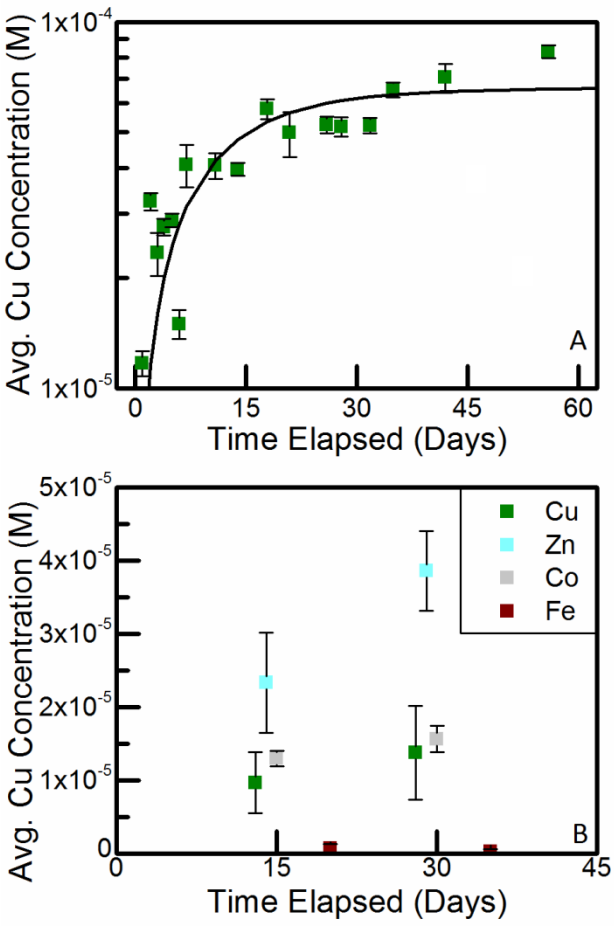

Figure 29: The diffusion over time of all four metal types from freshly synthesized paints. Diffusion of Cu^{2+} over 60 days from freshly synthesized paint measured with a selective ion probe (A). 15 and 30 day diffusion of Cu^{2+} from fresh paint measured via ICP-MS (B). Paint rapidly reaches equilibrium for Cu and Co. Fe does not substantially diffuse. Zn diffusion is greatest in magnitude but also the slowest to reach equilibrium.

8.3.2 Efficacy of metal-loaded paints against *E. coli* bacteria

Antibacterial testing was conducted to determine if diffusion rates were sufficient to kill *E. coli*. All four metal loaded paints were tested alongside a polystyrene and glass control (**Figure 30A**). As expected, the copper and zinc samples were the most effective

at killing bacteria. Cobalt and iron were somewhat effective, but not to a level that would be practical. To ensure that the paint does not rapidly lose efficacy, copper and zinc loaded paints were tested a month after synthesis (**Figure 30B)**. No significant reduction in killing was observed suggesting that the paints will retain efficacy for a long period of time.

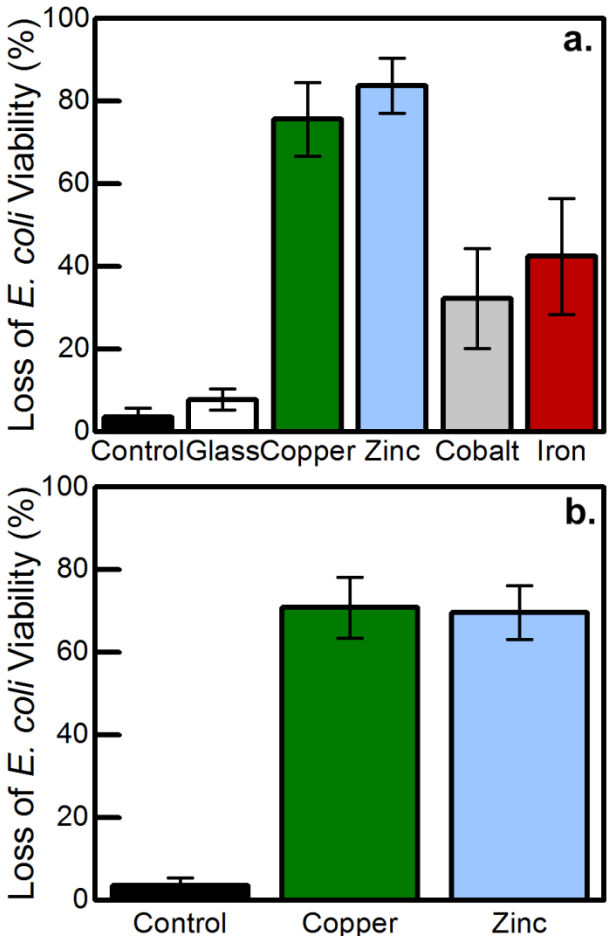

Figure 30: Loss of viability for *E. coli* when exposed to metal loaded paint for 2 hr. (A). Copper and zinc were both similarly effective, while cobalt and iron killed less than half of the bacteria in 2 hr. The experiment was repeated for copper and zinc loaded paints for paints that had been aged in normal conditions for 30 days (B). Copper and zinc retained efficacy after one month and killed nearly 80% of *E. coli* in 2 hrs.

To expound on the results of the antibacterial testing, the relative MICs of the metal salts were measured directly (**Table 2**). All of the MICs were very similar to one another with zinc and cobalt being effective at a quarter of the concentration of copper and iron. We found that our results were similar to literature values.[66] Since the MIC values are so similar, it is likely that diffusion rates are mostly responsible for the different rates of killing shown by the different metal types.

Table 2: MIC values for relevant metal ion salts.

Metal Ion	Copper	Zinc	Cobalt	Iron
MIC (μg/mL)	512	128	128	512

8.4 Conclusion

Our novel system for self-assembled metal nanoparticle loaded oil-based paints should provide and cheap and effective solution killing potentially harmful bacteria and preventing deleterious buildup of bacterial biofilms. We found via TEM that copper nanoparticles assembled into large aggregates, while cobalt nanoparticles formed large oblong particles. Iron and zinc nanoparticles were found to form small spheroids. Copper was shown to readily diffuse within 7.5 days with cobalt being similar and zinc having a greater equilibrium concentration but lesser rate constant. Iron was not found to diffuse in appreciable quantities. Antibacterial testing found that copper and zinc loaded paints were the most effective, with cobalt and iron loaded films being much less effective, and the two controls having no measurable effect. MIC's for the metal salts were also obtained and it was found that zinc and cobalt were marginally more effective than cobalt

and iron at killing *E. coli*. Additional work will be done on bacterial interaction with the films under shear flow to fully characterize the films potential for antifouling applications. At the end of all the characterization, we believe we will find a highly effective and cheap antibacterial coating.

CHAPTER 9

CONCLUSION AND FUTURE WORK

Biopolymer polyelectrolytes are a varied and useful class of materials. They can be combined with each other, metal ions, or neutral polymers to create a wide variety of materials. Utilizing rheology as a major characterization method, we can optimize these materials provide antibacterial properties, antifouling characteristics, or an appropriate substrate for cell culture.

The major portion of this work focused on tuning the interactions between chitosan and pectin. Chitosan and pectin were synthesized into polyelectrolyte complexes that were one thousand times smaller than previous particles.[15,79,80] The size, surface charge, and morphology of the LMW CS:Pec nanoparticles were examined using DLS, electrophoretic DLS, and TEM, respectively. The zeta potential was shown to be tunable, but the particles were found to become unstable after 14 days. While the properties of chitosan and pectin are well known, future testing should be done to confirm the antibacterial and anti-inflammatory properties are still present in the nanoparticles. As the stability of the particles was low, work should be conducted to see if metal nanoparticle cores or the use of quaternized chitosan would enhance stability. We synthesized and characterized a biologically compatible thermoreversible CS:Pec hydrogel whose strength and gelation temperature were improved by replacing the acid with salt. Hydrogels were found to strengthen at lower temperatures. Dried hydrogels rapidly swelled to ~370% of their initial weight. Our acid-free hydrogels were found to be biocompatible and improved by rinsing the salt. There are a number of directions for

future work to proceed. Animal models are a critical phase in demonstrating a new wound dressing and using a diabetic mouse wound model would be an excellent way to prove the dressing. The suitability of the gels for drug delivery, especially wound healing proteins, should also be explored. Our “green” systems hold great promise for future study and use as a wound healing product.

Rheology is a powerful tool for characterizing and improving a wide variety of systems. We used the chain entanglement concentration and viscosity to improve the loading of essential oils in a CS/PEO nanofiber system. MW and DA were optimized for oil incorporation. Future works should examine the storage limitations of these mats and methods of increasing loading, like surfactants. The system could also be adapted to other essential oils in the future. Shear rheology was used to establish average stiffnesses for porcine bone marrow, porcine lung, muscine brain, and porcine brain tissue. The tissues were all elastic with various degrees of inter-sample heterogeneity. This work provides a solid basis for the synthesis of hydrogel mimetics. Future work should focus on active hydrogels that match these properties for accurate cell culture. Zwitterionic systems are antifouling, but usually soft. We used a zwitterionic crosslinker on three sufficiently stiff PEGDMA systems. Polydopamine did not reduce mechanical properties and in one case improved stiffness. In the future, bacterial adhesion tests should be used to characterize the antifouling efficacy of the gels. We will also look at atomic force microscopy (AFM) to characterize roughness and Fourier transform infrared spectroscopy (FTIR) to confirm appropriate crosslinking. We have demonstrated the value of rheology and used it a driving force in three disparate studies.

The final section of this thesis focused on our novel system for self-assembled metal nanoparticle loaded oil-based paints. We found via TEM that copper nanoparticles assembled into large aggregates, while cobalt nanoparticles formed large oblong particles. Iron and zinc nanoparticles were found to form small spheroids. Copper readily diffused within 7.5 days with cobalt being similar and zinc having a greater equilibrium concentration but lesser rate constant. Iron was not found to diffuse in appreciable quantities. Antibacterial testing found that copper and zinc loaded paints were the most effective, with cobalt and iron loaded films being much less effective. Additional work still needs to be done on this system. Shear flow bacterial growth experiments will be conducted to determine if the films have potential in antifouling applications. The drying times of the films are longer than ideal, but could be reduced by decreasing the volume of naphthenate added, developing a drying protocol that includes UV exposure, or adding other drying agents. The long-term antibacterial activity of these paints should also be determined to show that these films are a viable product. At the end of all the characterization and optimization, we believe we will find a highly effective and cheap antibacterial coating.

CHAPTER 10

SCIENTIFIC CONTRIBUTIONS

The work in this thesis has culminated in a number of publications, which are listed in this section. Additionally, dissemination of this work has taken place through various conference presentations.

Rieger, K. A.; Birch, N. P.; Schiffman, J. D. Designing Electrospun Nanofiber Mats to Promote Wound Healing – a Review. *J. Mater. Chem. B* **2013**, *1* (36), 4531–4541.

Birch, N. P.; Schiffman, J. D. Characterization of Self-Assembled Polyelectrolyte Complex Nanoparticles Formed from Chitosan and Pectin. *Langmuir* **2014**, *30* (12), 3441–3447.

Birch, N. P.; Barney, L. E.; Pandres, E.; Peyton, S. R.; Schiffman, J. D. Thermal-Responsive Behavior of a Cell Compatible Chitosan/Pectin Hydrogel. *Biomacromolecules* **2015**, *16* (6), 1837–1843.

Jansen, L. E.; Birch, N. P.; Schiffman, J. D.; Crosby, A. J.; Peyton, S. R. Mechanics of Intact Bone Marrow. *J. Mech. Behav. Biomed. Mater.* **2015**, *50*, 299–307.

Rieger, K. A.; Birch, N. P.; Schiffman, J. D. Electrospinning Chitosan/poly(ethylene Oxide) Solutions with Essential Oils: Correlating Solution Rheology to Nanofiber Formation. *Carbohydr. Polym.* **2016**, *139*, 131–138.

Kolewe, K.W., Birch, N.P., Mako N, Schiffman, J.D. “Antifouling hydrogels: Synergy of chemical and mechanical properties” In Preparation

Birch, N. P., Kolewe, K. W., Digiovanni, T., Champagne, V. K., Schiffman, J. D. “Self-assembled antibacterial metal nanoparticles in alkyd-based paints” In Preparation

Galarza, S., Mijailovic, A.S., Birch, N.P., Schiffman, J.D., Crosby, A.J., Peyton, S.R., and Van Vliet, K.J. “Measurement of Brain Tissue Mechanical Properties by Cavitation Rheology” In Preparation

Polio, S. R., Aurian-Blajeni, D. E., Birch, N. P., Schiffman, J. D., Crosby, A. J., Peyton, S. R. “Comparative mechanical testing of lung parenchyma” In Preparation

REFERENCES

(1) Zhang, J. X. Complexity of Drug Therapy and Its Implications for Quality of Diabetes Care. *World J. Diabetes* **2011**, *2* (7), 105–107.

(2) James, G. A.; Swogger, E.; Wolcott, R.; Pulcini, E. deLancey; Secor, P.; Sestrich, J.; Costerton, J. W.; Stewart, P. S. Biofilms in Chronic Wounds. *Wound Repair Regen.* **2007**, *16* (1), 37–44.

(3) Gurtner, G. C.; Werner, S.; Barrandon, Y.; Longaker, M. T. Wound Repair and Regeneration. *Nature* **2008**, *453* (7193), 314–321.

(4) Blakytny, R.; Jude, E. The Molecular Biology of Chronic Wounds and Delayed Healing in Diabetes. *Diabet. Med.* **2006**, *23* (6), 594–608.

(5) Shai, A.; Maibach, H. I. *Wound Healing and Ulcers of the Skin: Diagnosis and Therapy - The Practical Approach*; Springer: Berlin, 2005.

(6) Rieger, K. A.; Birch, N. P.; Schiffman, J. D. Designing Electrospun Nanofiber Mats to Promote Wound Healing – a Review. *J. Mater. Chem. B* **2013**, *1* (36), 4531–4541.

(7) Varghese, S.; Elisseeff, J. Hydrogels for Musculoskeletal Tissue Engineering. *Polym. Regen. Med.* **2006**, *203* (January), 95–144.

(8) Moura, M. J.; Figueiredo, M. M.; Gil, M. H. Rheological Study of Genipin Cross-Linked Chitosan Hydrogels. *Biomacromolecules* **2007**, *8* (12), 3823–3829.

(9) Nordby, M. H.; Kjoniksen, A. L.; Nystrom, B.; Roots, J. Thermoreversible Gelation of Aqueous Mixtures of Pectin and Chitosan. Rheology. *Biomacromolecules* **2003**, *4* (2), 337–343.

(10) Bernabé, P.; Peniche, C.; Argüelles-Monal, W.; Bernabe, P.; Arguelles-Monal, W. Swelling Behavior of Chitosan/pectin Polyelectrolyte Complex Membranes. Effect of Thermal Cross-Linking. *Polym. Bull.* **2005**, *55* (5), 367–375.

(11) Zhang, H.; Oh, M.; Allen, C.; Kumacheva, E. Monodisperse Chitosan Nanoparticles for Mucosal Drug Delivery. *Biomacromolecules* **2004**, *5* (6), 2461–2468.

(12) Morris, G. A.; Kok, M. S.; Harding, S. E.; Adams, G. G. Polysaccharide Drug Delivery Systems Based on Pectin and Chitosan. *Biotechnol. Genet. Eng. Rev.* **2010**, *27*, 257–283.

(13) Kong, M.; Chen, X. G.; Xing, K.; Park, H. J. Antimicrobial Properties of Chitosan and Mode of Action: A State of the Art Review. *Int. J. Food Microbiol.* **2010**, *144* (1), 51–63.

(14) Markov, P. A.; Popov, S. V.; Nikitina, I. R.; Ovodova, R. G.; Ovodov, Y. S. Anti-Inflammatory Activity of Pectins and Their Galacturonan Backbone. *Russ. J. Bioorganic Chem.* **2011**, *37* (7), 817–821.

(15) Chen, C.-H.; Sheu, M.-T.; Chen, T.-F.; Wang, Y.-C.; Hou, W.-C.; Liu, D.-Z.; Chung, T.-C.; Liang, Y.-C. Suppression of Endotoxin-Induced Proinflammatory Responses by Citrus Pectin through Blocking LPS Signaling Pathways. *Biochem. Pharmacol.* **2006**, *72* (8), 1001–1009.

(16) Bordi, F.; Colby, R. H.; Cametti, C.; de Lorenzo, L.; Gili, T. Electrical Conductivity of Polyelectrolyte Solutions in the Semidilute and Concentrated Regime: The Role of Counterion Condensation. *J. Phys. Chem. B* **2002**, *106*, 6887–6893.

(17) Boddohi, S.; Moore, N.; Johnson, P. A.; Kipper, M. J. Polysaccharide-Based Polyelectrolyte Complex Nanoparticles from Chitosan, Heparin, and Hyaluronan. *Biomacromolecules* **2009**, *10* (6), 1402–1409.

(18) Schatz, C.; Domard, A.; Viton, C.; Pichot, C.; Delair, T. Versatile and Efficient Formation of Colloids of Biopolymer-Based Polyelectrolyte Complexes. *Biomacromolecules* **2004**, *5* (5), 1882–1892.

(19) Opanasopit, P.; Apirakaramwong, A.; Ngawhirunpat, T.; Rojanarata, T.; Ruktanonchai, U. Development and Characterization of Pectinate Micro/nanoparticles for Gene Delivery. *AAPS PharmSciTech* **2008**, *9* (1), 67–74.

(20) Qi, L.; Xu, Z.; Jiang, X.; Hu, C.; Zou, X. Preparation and Antibacterial Activity of Chitosan Nanoparticles. *Carbohydr. Res.* **2004**, *339* (16), 2693–2700.

(21) Leu, J.-G.; Chen, S.-A.; Chen, H.-M.; Wu, W.-M.; Hung, C.-F.; Yao, Y.-D.; Tu, C.-S.; Liang, Y.-J. The Effects of Gold Nanoparticles in Wound Healing with Antioxidant Epigallocatechin Gallate and α-Lipoic Acid. *Nanomedicine* **2012**, *8* (5), 767–775.

(22) Mary, G.; Bajpai, S. K.; Chand, N. Copper (II) Ions and Copper Nanoparticles-Loaded Chemically Modified Cotton Cellulose Fibers with Fair Antibacterial Properties. *J. Appl. Polym. Sci.* **2009**, *113* (2), 757–766.

(23) Jain, J.; Arora, S.; Rajwade, J. M.; Omray, P.; Khandelwal, S.; Paknikar, K. M. Silver Nanoparticles in Therapeutics: Development of an Antimicrobial Gel Formulation for Topical Use. *Mol. Pharm.* **2009**, *6* (5), 1388–1401.

(24) Ahamed, M.; Alsalhi, M. S.; Siddiqui, M. K. J. Silver Nanoparticle Applications and Human Health. *Clin. Chim. Acta* **2010**, *411* (23-24), 1841–1848.

(25) Rai, M.; Yadav, A.; Gade, A. Silver Nanoparticles as a New Generation of Antimicrobials. *Biotechnol. Adv.* **2009**, *27* (1), 76–83.

(26) Wiarachai, O.; Thongchul, N.; Kiatkamjornwong, S.; Hoven, V. P. Surface-Quaternized Chitosan Particles as an Alternative and Effective Organic Antibacterial Material. *Colloids Surfaces. B Biointerfaces* **2012**, *92*, 121–129.

(27) Ovodov, Y. S. Current Views on Pectin Substances. *Russ. J. Bioorganic Chem.* **2009**, *35* (3), 269–284.

(28) Casper, C. L.; Yamaguchi, N.; Kiick, K. L.; Rabolt, J. F. Functionalizing Electrospun Fibers with Biologically Relevant Macromolecules. *Biomacromolecules 6* (4), 1998–2007.

(29) Ojha, S. S.; Stevens, D. R.; Hoffman, T. J.; Stano, K.; Klossner, R.; Scott, M. C.; Krause, W.; Clarke, L. I.; Gorga, R. E. Fabrication and Characterization of Electrospun Chitosan Nanofibers Formed via Templating with Polyethylene Oxide. *Biomacromolecules* **2008**, *9* (9), 2523–2529.

(30) Deitzel, J. M.; Kleinmeyer, J. D.; Hirvonen, J. K.; Tan, N. C. B. Controlled Deposition of Electrospun Poly (Ethylene Oxide) ® Bers. *Polymer (Guildf).* **2001**, *42*, 8163–8170.

(31) Yuan, H.; Kononov, S.; Cavalcante, F. S.; Lutchen, K. R.; Ingenito, E. P.; Suki, B. Effects of Collagenase and Elastase on the Mechanical Properties of Lung Tissue Strips. *J. Appl. Physiol.* **2000**, *89* (1), 3–14.

(32) Pogoda, K.; Chin, L.; Georges, P. C.; Byfield, F. J.; Bucki, R.; Kim, R.; Weaver, M.; Wells, R. G.; Marcinkiewicz, C.; Janmey, P. A. Compression Stiffening of Brain and Its Effect on Mechanosensing by Glioma Cells. *New J. Phys.* **2014**, *16* (7), 075002.

(33) Saito, H.; Lai, J.; Rogers, R.; Doerschuk, C. M. Mechanical Properties of Rat Bone Marrow and Circulating Neutrophils and Their Responses to Inflammatory Mediators. *Blood* **2002**, *99* (6), 2207–2213.

(34) Sobotkova, E.; Hruba, A.; Kiefman, J.; Sobotka, Z. Rhelogocal Behavior of Bone Marrow. *Biorheology* **1988**, 467–469.

(35) Zhong, Z.; Akkus, O. Effects of Age and Shear Rate on the Rheological Properties of Human Yellow Bone Marrow. *Biorheology* **2011**, *48* (2), 89–97.

(36) Bryant, J.; David, T.; Gaskell, P.; King, S.; Lond, G. Rheology of Bovine Bone Marrow. *Proc Instn Mech Engrs* **1988**, *203*, 71–75.

(37) Bryant, J. On the Mechanical Function of Marrow in Long Bones. *Eng. Med.* **1988**, *17* (2), 55–58.

(38) Engel, Y.; Schiffman, J. D.; Goddard, J. M.; Rotello, V. M. Nanomanufacturing of Biomaterials. *Mater. Today* **2012**, *15* (11), 478–485.

(39) Reneker, D. H.; Yarin, A. L.; Fong, H.; Koombhongse, S. Bending Instability of Electrically Charged Liquid Jets of Polymer Solutions in Electrospinning. *J. Appl. Phys.* **2000**, *87* (9), 4531.

(40) Persano, L.; Camposeo, A.; Tekmen, C.; Pisignano, D. Industrial Upscaling of Electrospinning and Applications of Polymer Nanofibers: A Review. *Macromol. Mater. Eng.* **2013**, *298* (5), 504–520.

(41) Ohkawa, K.; Cha, D.; Kim, H.; Nishida, A.; Yamamoto, H. Electrospinning of Chitosan. *Macromol. Rapid Commun.* **2004**, *25* (18), 1600–1605.

(42) Pakravan, M.; Heuzey, M.-C.; Ajji, A. A Fundamental Study of chitosan/PEO Electrospinning. *Polymer (Guildf).* **2011**, *52* (21), 4813–4824.

(43) Chang, J.-J.; Lee, Y.-H.; Wu, M.-H.; Yang, M.-C.; Chien, C.-T. Preparation of Electrospun Alginate Fibers with Chitosan Sheath. *Carbohydr. Polym.* **2012**, *87* (3), 2357–2361.

(44) Saquing, C. D.; Tang, C.; Monian, B.; Bonino, C. A.; Manasco, J. L.; Alsberg, E.; Khan, S. A. Alginate–Polyethylene Oxide Blend Nanofibers and the Role of the Carrier Polymer in Electrospinning. *Ind. Eng. Chem. Res.* **2013**, *52* (26), 8692–8704.

(45) Kong, L.; Ziegler, G. R. Role of Molecular Entanglements in Starch Fiber Formation by Electrospinning. *Biomacromolecules* **2012**, *13* (8), 2247–2253.

(46) Kai, D.; Jin, G.; Prabhakaran, M. P.; Ramakrishna, S. Electrospun Synthetic and Natural Nanofibers for Regenerative Medicine and Stem Cells. *Biotechnol. J.* **2013**, *8* (1), 59–72.

(47) Luo, Y.; Shen, H.; Fang, Y.; Cao, Y.; Huang, J.; Zhang, M.; Dai, J.; Shi, X.; Zhang, Z. Enhanced Proliferation and Osteogenic Differentiation of Mesenchymal Stem Cells on Graphene Oxide-Incorporated Electrospun Poly(lactic- Co -Glycolic Acid) Nanofibrous Mats. *ACS Appl. Mater. Interfaces* **2015**, 150312093657004.

(48) Zhang, X.; Suresh Kumar, P.; Aravindan, V.; Liu, H. H.; Sundaramurthy, J.; Mhaisalkar, S. G.; Duong, H. M.; Ramakrishna, S.; Madhavi, S. Electrospun TiO 2 –Graphene Composite Nanofibers as a Highly Durable Insertion Anode for Lithium Ion Batteries. *J. Phys. Chem. C* **2012**, *116* (28), 14780–14788.

(49) He, X.; Tan, L.; Wu, X.; Yan, C.; Chen, D.; Meng, X.; Tang, F. Electrospun Quantum Dots/polymer Composite Porous Fibers for Turn-on Fluorescent Detection of Lactate Dehydrogenase. *J. Mater. Chem.* **2012**, *22* (35), 18471.

(50) Schiffman, J. D.; Wang, Y.; Giannelis, E. P.; Elimelech, M. Biocidal Activity of Plasma Modified Electrospun Polysulfone Mats Functionalized with Polyethyleneimine-Capped Silver Nanoparticles. *Langmuir* **2011**, *27* (21), 13159–13164.

(51) Persano, L.; Camposeo, A.; Pisignano, D. Active Polymer Nanofibers for Photonics, Electronics, Energy Generation and Micromechanics. *Prog. Polym. Sci.* **2014**, *43*, 48–95.

(52) Persano, L.; Camposeo, A.; Di Benedetto, F.; Stabile, R.; Laera, A. M.; Piscopiello, E.; Tapfer, L.; Pisignano, D. CdS-Polymer Nanocomposites and Light-Emitting Fibers by in Situ Electron-Beam Synthesis and Lithography. *Adv. Mater.* **2012**, *24* (39), 5320–5326.

(53) Sanders, E. H.; Kloefkorn, R.; Bowlin, G. L.; Simpson, D. G.; Wnek, G. E. Two-Phase Electrospinning from a Single Electrified Jet: Microencapsulation of Aqueous Reservoirs in Poly(ethylene- Co -Vinyl Acetate) Fibers. *Macromolecules* **2003**, *36* (11), 3803–3805.

(54) Xu, X.; Yang, L.; Xu, X.; Wang, X.; Chen, X.; Liang, Q.; Zeng, J.; Jing, X. Ultrafine Medicated Fibers Electrospun from W/O Emulsions. *J. Control. Release* **2005**, *108* (1), 33–42.

(55) Xu, X.; Zhuang, X.; Chen, X.; Wang, X.; Yang, L.; Jing, X. Preparation of Core-Sheath Composite Nanofibers by Emulsion Electrospinning. *Macromol. Rapid Commun.* **2006**, *27* (19), 1637–1642.

(56) Angeles, M.; Cheng, H.; Velankar, S. S. Emulsion Electrospinning: Composite Fibers from Drop Breakup during Electrospinning. *Polym. Adv. Technol.* **2008**, *19* (7), 728–733.

(57) Li, Y.; Ko, F. K.; Hamad, W. Y. Effects of Emulsion Droplet Size on the Structure of Electrospun Ultrafine Biocomposite Fibers with Cellulose Nanocrystals. *Biomacromolecules* **2013**, *14* (11), 3801–3807.

(58) Briggs, T.; Arinzeh, T. L. Examining the Formulation of Emulsion Electrospinning for Improving the Release of Bioactive Proteins from Electrospun Fibers. *J. Biomed. Mater. Res. A* **2014**, *102* (3), 674–684.

(59) Qi, H.; Hu, P.; Xu, J.; Wang, A.; Qi; Wang. Encapsulation of Drug Reservoirs in Fibers by Emulsion Electrospinning: Morphology Characterization and Preliminary Release Assessment. *Biomacromolecules* **2006**, *7* (8), 2327–2330.

(60) Rieger, K. A.; Schiffman, J. D. Electrospinning an Essential Oil: Cinnamaldehyde Enhances the Antimicrobial Efficacy of Chitosan/poly(ethylene Oxide) Nanofibers. *Carbohydr. Polym.* **2014**, *113*, 561–568.

(61) Díaz, J. E.; Barrero, A.; Márquez, M.; Loscertales, I. G. Controlled Encapsulation of Hydrophobic Liquids in Hydrophilic Polymer Nanofibers by Co-Electrospinning. *Adv. Funct. Mater.* **2006**, *16* (16), 2110–2116.

(62) Yang, Y.; Li, X.; Cui, W.; Zhou, S.; Tan, R.; Wang, C. Structural Stability and Release Profiles of Proteins from Core-Shell Poly (DL-Lactide) Ultrafine Fibers Prepared by Emulsion Electrospinning. *J. Biomed. Mater. Res., Part A* **2008**, *86* (2), 374–385.

(63) Yang, Y.; Li, X.; Cheng, L.; He, S.; Zou, J.; Chen, F.; Zhang, Z. Core-Sheath Structured Fibers with pDNA Polyplex Loadings for the Optimal Release Profile and Transfection Efficiency as Potential Tissue Engineering Scaffolds. *Acta Biomater.* **2011**, *7* (6), 2533–2543.

(64) Xu, X.; Chen, X.; Ma, P.; Wang, X.; Jing, X. The Release Behavior of Doxorubicin Hydrochloride from Medicated Fibers Prepared by Emulsion-Electrospinning. *Eur. J. Pharm. Biopharm.* **2008**, *70* (1), 165–170.

(65) Xing, K.; Chen, X. G.; Kong, M.; Liu, C. S.; Cha, D. S.; Park, H. J. Effect of Oleoyl-Chitosan Nanoparticles as a Novel Antibacterial Dispersion System on Viability, Membrane Permeability and Cell Morphology of Escherichia Coli and Staphylococcus Aureus. *Carbohydr. Polym.* **2009**, *76* (1), 17–22.

(66) Du, W.-L.; Niu, S.-S.; Xu, Y.-L.; Xu, Z.-R.; Fan, C.-L. Antibacterial Activity of Chitosan Tripolyphosphate Nanoparticles Loaded with Various Metal Ions. *Carbohydr. Polym.* **2009**, *75* (3), 385–389.

(67) Long, D.; Wu, G.; Chen, S. Preparation of Oligochitosan Stabilized Silver Nanoparticles by Gamma Irradiation. *Radiat. Phys. Chem.* **2007**, *76* (7), 1126–1131.

(68) Laudenslager, M. J.; Schiffman, J. D.; Schauer, C. L. Carboxymethyl Chitosan as a Matrix Material for Platinum, Gold, and Silver Nanoparticles. *Biomacromolecules* **2008**, *9* (10), 2682–2685.

(69) Justesen, J.; Stenderup, K.; Ebbesen, E. N.; Mosekilde, L.; Steiniche, T.; Kassem, M. Adipocyte Tissue Volume in Bone Marrow Is Increased with Aging and in Patients with Osteoporosis. *Biogerontology* **2001**, *2*, 165–171.

(70) Engler, A. J.; Sen, S.; Sweeney, H. L.; Discher, D. E. Matrix Elasticity Directs Stem Cell Lineage Specification. *Cell* **2006**, *126* (4), 677–689.

(71) Lee, J.; Abdeen, A. a; Kilian, K. a. Rewiring Mesenchymal Stem Cell Lineage Specification by Switching the Biophysical Microenvironment. *Sci. Rep.* **2014**, *4*, 5188.

(72) Sikavitsas, V. I.; Bancroft, G. N.; Holtorf, H. L.; Jansen, J. a; Mikos, A. G. Mineralized Matrix Deposition by Marrow Stromal Osteoblasts in 3D Perfusion Culture Increases with Increasing Fluid Shear Forces. *Proc. Natl. Acad. Sci. U. S. A.* **2003**, *100* (25), 14683–14688.

(73) Yang, C.; Tibbitt, M. W.; Basta, L.; Anseth, K. S. Mechanical Memory and Dosing Influence Stem Cell Fate. *Nat. Mater.* **2014**, *13* (June), 645–652.

(74) Silver, S.; Phung, L. T.; Silver, G. Silver as Biocides in Burn and Wound Dressings and Bacterial Resistance to Silver Compounds. *J. Ind. Microbiol. Biotechnol.* **2006**, *33* (7), 627–634.

(75) Sorlier, P.; Denuzière, A.; Viton, C.; Domard, A. Relation between the Degree of Acetylation and the Electrostatic Properties of Chitin and Chitosan. *Biomacromolecules* **2001**, *2* (3), 765–772.

(76) Neal, A. L. What Can Be Inferred from Bacterium-Nanoparticle Interactions about the Potential Consequences of Environmental Exposure to Nanoparticles? *Ecotoxicology* **2008**, *17* (5), 362–371.

(77) Gan, Q.; Wang, T.; Cochrane, C.; McCarron, P. Modulation of Surface Charge, Particle Size and Morphological Properties of Chitosan-TPP Nanoparticles Intended for Gene Delivery. *Colloids Surfaces B Biointerfaces* **2005**, *44* (2-3), 65–73.

(78) Sæther, H. V.; Holme, H. K.; Maurstad, G.; Smidsrød, O.; Stokke, B. T. Polyelectrolyte Complex Formation Using Alginate and Chitosan. *Carbohydr. Polym.* **2008**, *74* (4), 813–821.

(79) Yu, C.-Y.; Yin, B.-C.; Zhang, W.; Cheng, S.-X.; Zhang, X.-Z.; Zhuo, R.-X. Composite Microparticle Drug Delivery Systems Based on Chitosan, Alginate and Pectin with Improved pH-Sensitive Drug Release Property. *Colloids Surf. B. Biointerfaces* **2009**, *68* (2), 245–249.

(80) Oliveira, G. F.; Ferrari, P. C.; Carvalho, L. Q.; Evangelista, R. C. Chitosan–pectin Multiparticulate Systems Associated with Enteric Polymers for Colonic Drug Delivery. *Carbohydr. Polym.* **2010**, *82* (3), 1004–1009.

(81) Kim, T. H.; Park, Y. H.; Kim, K. J.; Cho, C. S. Release of Albumin from Chitosan-Coated Pectin Beads in Vitro. *Int. J. Pharm.* **2003**, *250* (2), 371–383.

(82) Qurashi, M. T.; Blair, H. S.; Allen, S. J. Studies on Modified Chitosan Membranes. I. Preparation and Characterization. *J. Appl. Polym. Sci.* **1992**, *46* (2), 255–261.

(83) Fernandez-Megia, E.; Novoa-Carballal, R.; Quiñoá, E.; Riguera, R. Optimal Routine Conditions for the Determination of the Degree of Acetylation of Chitosan by 1H-NMR. *Carbohydr. Polym.* **2005**, *61* (2), 155–161.

(84) Hirai, A.; Odani, H.; Nakajima, A. Determination of Degree of Deacetylation of Chitosan by 1H NMR Spectroscopy. *Polym. Bull.* **1991**, *26*, 87–94.

(85) Vårum, K.; Antohonsen, M.; Grasdalen, H.; Smidsrød, O. Determination of the Degree of N-Acetylation and the Distribution of N-Acetyl Groups in Partially N-Deacetylated Chitins (Chitosans) by High-Field N.m.r. Spectroscopy. *Carbohydr. Res.* **1991**, *211*, 17–23.

(86) Institute of Medicine (U.S.). Committee on Food Chemicals Codex. *Food Chemicals Codex*, 5th ed.; National Academy Press: Washington, DC, 2003.

(87) Monsoor, M. A.; Kalapathy, U.; Proctor, A. Improved Method for Determination of Pectin Degree of Esterification by Diffuse Reflectance Fourier Transform Infrared Spectroscopy. *J. Agric. Food Chem.* **2001**, *49* (6), 2756–2760.

(88) Jonassen, H.; Kjøniksen, A.-L.; Hiorth, M. Stability of Chitosan Nanoparticles Cross-Linked with Tripolyphosphate. *Biomacromolecules* **2012**, *13* (11), 3747–3756.

(89) Umerska, A.; Paluch, K. J.; Inkielewicz-Stępniak, I.; Santos-Martinez, M. J.; Corrigan, O. I.; Medina, C.; Tajber, L. Exploring the Assembly Process and Properties of Novel Crosslinker-Free Hyaluronate-Based Polyelectrolyte Complex Nanocarriers. *Int. J. Pharm.* **2012**, *436* (1-2), 75–87.

(90) Smidsrød, O.; Haug, A.; Larsen, B. The Influence of pH on the Rate of Hydrolysis of Acidic Polysaccharides. *Acta Chem. Scand.* **1966**, *20*, 1026–1034.

(91) Hafner, A.; Dürrigl, M.; Pepić, I.; Filipović-Grčić, J. Short- and Long-Term Stability of Lyophilised Melatonin-Loaded Lecithin/chitosan Nanoparticles. *Chem. Pharm. Bull. (Tokyo).* **2011**, *59* (9), 1117–1123.

(92) Nayak, B.; Parida, P. K.; Routa, P.; Ray, P.; Panda, A. K.; Ray, A. R. Chitosan Micro and Nanoparticles for Delivery of Drugs and Therapeutic Proteins. In *International World Conference, WCN 2011, Second world conference on nanomedicine and drug delivery*; Kottayam, Kerala , India, 2011.

(93) Ulubayram, K.; Aksu, E.; Gurhan, S. I. D.; Serbetci, K.; Hasirci, N. Cytotoxicity Evaluation of Gelatin Sponges Prepared with Different Cross-Linking Agents. *J. Biomater. Sci. Polym. Ed.* **2002**, *13* (11), 1203–1219.

(94) Marinucci, L.; Lilli, C.; Guerra, M.; Belcastro, S.; Becchetti, E.; Stabellini, G.; Calvi, E. M.; Locci, P. Biocompatibility of Collagen Membranes Crosslinked with Glutaraldehyde or Diphenylphosphoryl Azide: An in Vitro Study. *J. Biomed. Mater. Res. A* **2003**, *67* (2), 504–509.

(95) Birch, N. P.; Schiffman, J. D. Characterization of Self-Assembled Polyelectrolyte Complex Nanoparticles Formed from Chitosan and Pectin. *Langmuir* **2014**, *30* (12), 3441–3447.

(96) Yuan, Y.; Chesnutt, B. M.; Utturkar, G.; Haggard, W. O.; Yang, Y.; Ong, J. L.; Bumgardner, J. D. The Effect of Cross-Linking of Chitosan Microspheres with Genipin on Protein Release. *Carbohydr. Polym.* **2007**, *68* (3), 561–567.

(97) Lee, Y.-H.; Chang, J.-J.; Yang, M.-C.; Chien, C.-T.; Lai, W.-F. Acceleration of Wound Healing in Diabetic Rats by Layered Hydrogel Dressing. *Carbohydr. Polym.* **2012**, *88*, 809–819.

(98) Wang, L.; Khor, E.; Wee, A.; Lim, L. Y. Chitosan-Alginate PEC Membrane as a Wound Dressing: Assessment of Incisional Wound Healing. *J. Biomed. Mater. Res.* **2002**, *63* (5), 610–618.

(99) Thomas, a; Harding, K. G.; Moore, K. Alginates from Wound Dressings Activate Human Macrophages to Secrete Tumour Necrosis Factor-Alpha. *Biomaterials* **2000**, *21* (17), 1797–1802.

(100) Barck, K.; Butler, M. F. Comparison of Morphology and Properties of Polyelectrolyte Complex Particles Formed from Chitosan and Polyanionic Biopolymers. *J. Appl. Polym. Sci.* **2005**, *98* (4), 1581–1593.

(101) Birch, N. P.; Schiffman, J. D. Characterization of Self-Assembled Polyelectrolyte Complex Nanoparticles Formed from Chitosan and Pectin. *Langmuir* **2014**, *30* (12), 3441–3447.

(102) Winter, H. H.; Chambon, F. Analysis of Linear Viscoelasticity of a Crosslinking Polymer at the Gel Point. *J. Rheol. (N. Y. N. Y).* **1986**, *30*, 367.

(103) Chambon, F.; Winter, H. Linear Viscoelasticity at the Gel Point of a Crosslinking PDMS with Imbalanced Stoichiometry. *J. Rheol. (N. Y. N. Y).* **1987**, *31* (8), 683–697.

(104) Morrison, F. A. *Understanding Rheology*; Gubbins, K. F., Barteau, M. A., Lauffenburger, D. A., Morari, M., Ray, W. H., Russel, W. B., Tirrell, M. V., Eds.; Oxford University Press: New York, 2001.

(105) Bryant, S. J.; Anseth, K. S. Hydrogel Properties Influence ECM Production by Chondrocytes Photoencapsulated in Poly(ethylene Glycol) Hydrogels. *J. Biomed. Mater. Res.* **2002**, *59*, 63–72.

(106) Maxson, S.; Lopez, E. a.; Yoo, D.; Danilkovitch-Miagkova, a.; LeRoux, M. a. Concise Review: Role of Mesenchymal Stem Cells in Wound Repair. *Stem Cells Transl. Med.* **2012**, *1*, 142–149.

(107) Fennema, E.; Rivron, N.; Rouwkema, J.; van Blitterswijk, C.; De Boer, J. Spheroid Culture as a Tool for Creating 3D Complex Tissues. *Trends Biotechnol.* **2013**, *31* (2), 108–115.

(108) Fukuda, J.; Khademhosseini, A.; Yeo, Y.; Yang, X.; Yeh, J.; Eng, G.; Blumling, J.; Wang, C. F.; Kohane, D. S.; Langer, R. Micromolding of Photocrosslinkable Chitosan Hydrogel for Spheroid Microarray and Co-Cultures. *Biomaterials* **2006**, *27*, 5259–5267.

(109) Hsu, S.; Lin, Y.; Lin, T.; Tseng, T.; Lee, H.; Liao, Y.; Chiu, I. Spheroid Formation from Neural Stem Cells on Chitosan Membranes. *J. Med. Biol. ...* **2012**, *32* (2), 85–90.

(110) Gómez-Mascaraque, L. G.; Méndez, J. A.; Fernández-Gutiérrez, M.; Vázquez, B.; San Román, J. Oxidized Dextrins as Alternative Crosslinking Agents for Polysaccharides: Application to Hydrogels of Agarose-Chitosan. *Acta Biomater.* **2014**, *10* (2), 798–811.

(111) Guan, L.; Tian, P.; Ge, H.; Tang, X.; Zhang, H.; Du, L.; Liu, P. Chitosan-Functionalized Silk Fibroin 3D Scaffold for Keratocyte Culture. *J. Mol. Histol.* **2013**, *44* (5), 609–618.

(112) Peschel, G.; Dahse, H.-M.; Konrad, A.; Wieland, G. D.; Mueller, P.-J.; Martin, D. P.; Roth, M. Growth of Keratinocytes on Porous Films of poly(3-Hydroxybutyrate) and poly(4-Hydroxybutyrate) Blended with Hyaluronic Acid and Chitosan. *J. Biomed. Mater. Res. A* **2008**, *85* (4), 1072–1081.

(113) Bakkali, F.; Averbeck, S.; Averbeck, D.; Idaomar, M. Biological Effects of Essential Oils--a Review. *Food Chem. Toxicol.* **2008**, *46* (2), 446–475.

(114) Kavanaugh, N. L.; Ribbeck, K. Selected Antimicrobial Essential Oils Eradicate Pseudomonas Spp. and Staphylococcus Aureus Biofilms. *Appl. Environ. Microbiol.* **2012**, *78* (11), 4057–4061.

(115) Karami, Z.; Rezaeian, I.; Zahedi, P.; Abdollahi, M. Preparation and Performance Evaluations of Electrospun Poly(ε-Caprolactone), Poly(lactic Acid), and Their Hybrid (50/50) Nanofibrous Mats Containing Thymol as an Herbal Drug for Effective Wound Healing. *J. Appl. Polym. Sci.* **2013**, *129* (2), 756–766.

(116) Motealleh, B.; Zahedi, P.; Rezaeian, I.; Moghimi, M.; Abdolghaffari, A. H.; Zarandi, M. A. Morphology, Drug Release, Antibacterial, Cell Proliferation, and Histology Studies of Chamomile-Loaded Wound Dressing Mats Based on Electrospun Nanofibrous Poly(ε-Caprolactone)/polystyrene Blends. *J. Biomed. Mater. Res. B. Appl. Biomater.* **2014**, *102* (5), 977–987.

(117) Liakos, I.; Rizzello, L.; Hajiali, H.; Brunetti, V.; Carzino, R.; Pompa, P. P.; Athanassiou, A.; Mele, E. Fibrous Wound Dressings Encapsulating Essential Oils as Natural Antimicrobial Agents. *J. Mater. Chem. B* **2015**, *3* (8), 1583–1589.

(118) Xu, F.; Weng, B.; Gilkerson, R.; Materon, L. A.; Lozano, K. Development of Tannic Acid/chitosan/pullulan Composite Nanofibers from Aqueous Solution for Potential Applications as Wound Dressing. *Carbohydr. Polym.* **2015**, *115*, 16–24.

(119) Mori, C. L. S. de O.; dos Passos, N. A.; Oliveira, J. E.; Altoé, T. F.; Mori, F. A.; Mattoso, L. H. C.; Scolforo, J. R.; Tonoli, G. H. D. Nanostructured Polylactic Acid/Candeia Essential Oil Mats Obtained by Electrospinning. *J. Nanomater.* **2015**, *2015*, 1–9.

(120) Yao, C.-H.; Yeh, J.-Y.; Chen, Y.-S.; Li, M.-H.; Huang, C.-H. Wound-Healing Effect of Electrospun Gelatin Nanofibres Containing Centella Asiatica Extract in a Rat Model. *J. Tissue Eng. Regen. Med.* **2015**.

(121) Schiffman, J. D.; Schauer, C. L. A Review: Electrospinning of Biopolymer Nanofibers and Their Applications. *Polym. Rev.* **2008**, *48* (2), 317–352.

(122) Klossner, R. R.; Queen, H. A.; Coughlin, A. J.; Krause, W. E. Correlation of Chitosan's Rheological Properties and Its Ability to Electrospin. *Biomacromolecules* **2008**, *9* (10), 2947–2953.

(123) Guinesi, L. . Influence of Some Reactional Parameters on the Substitution Degree of Biopolymeric Schiff Bases Prepared from Chitosan and Salicylaldehyde. *Carbohydr. Polym.* **2006**, *65* (4), 557–561.

(124) Cordes, E. H.; Jencks, W. P. On the Mechanism of Schiff Base Formation and Hydrolysis. *J. Am. Chem. Soc.* **1962**, *84* (5), 832–837.

(125) Marin, L.; Moraru, S.; Popescu, M.-C.; Nicolescu, A.; Zgardan, C.; Simionescu, B. C.; Barboiu, M. Out-of-Water Constitutional Self-Organization of Chitosan-Cinnamaldehyde Dynagels. *Chemistry* **2014**, *20* (16), 4814–4821.

(126) Marin, L.; Simionescu, B.; Barboiu, M. Imino-Chitosan Biodynamers. *Chem. Commun.* **2012**, *48* (70), 8778.

(127) Yuan, Y.; Chesnutt, B. M.; Haggard, W. O.; Bumgardner, J. D. Deacetylation of Chitosan: Material Characterization and in Vitro Evaluation via Albumin Adsorption and Pre-Osteoblastic Cell Cultures. *Materials (Basel).* **2011**, *4*, 1399–1416.

(128) Yang, J.; Kuang, X.; Li, B.; Zhou, B.; Li, J.; Cui, B.; MA, M. Study on Release Mechanism of Inhibitory Components from Cinnamon and Clove Powders. *J. Food Saf.* **2012**, *32* (2), 189–197.

(129) Talrose, V.; Yermakov, A. N.; Usov, A. A.; Goncharova, A. A.; Leskin, A. .; Messineva, N. A.; Trusova, N. V.; Efimkina, M. V. UV/Visible Spectrum. *NIST Chem. WebBook, NIST Stand. Ref. Database Number 69, Eds. P.J. Linstrom W.G. Mallard, Natl. Inst. Stand. Technol.* **2007**.

(130) Hirai, A.; Odani, H.; Nakajima, A. Determination of Degree of Deacetylation of Chitosan by 1H NMR Spectroscopy. *Polym. Bull.* **1991**, *26*, 87–94.

(131) Ganjian, I.; Baumgarten, R. L.; Valenzuela, R. J. Using Spin-Spin Decoupling NMR for Structure Elucidation in the Extraction of Cinnamaldehyde. *J. Chem. Educ.* **1992**, *69* (6), 511.

(132) Iamsamai, C.; Hannongbua, S.; Ruktanonchai, U.; Soottitantawat, A.; Dubas, S. T. The Effect of the Degree of Deacetylation of Chitosan on Its Dispersion of Carbon Nanotubes. *Carbon N. Y.* **2010**, *48* (1), 25–30.

(133) Rodri-guez, M.; Albertengo, L. A.; Agullo, E. Emulsification Capacity of Chitosan. *Carbohydr. Polym.* **2002**, *48* (3), 271–276.

(134) Schulz, P. C.; Rodríguez, M. S.; Del Blanco, L. F.; Pistonesi, M.; Agulló, E. Emulsification Properties of Chitosan. *Colloid Polym. Sci.* **1998**, *276* (12), 1159–1165.

(135) Yan, L. Y.; Poon, Y. F.; Chan-Park, M. B.; Chen, Y.; Zhang, Q. Individually Dispersing Single-Walled Carbon Nanotubes with Novel Neutral pH Water-Soluble Chitosan Derivatives. *J. Phys. Chem. C* **2008**, *112* (20), 7579–7587.

(136) Dapčević Hadnađev, T.; Dokić, P.; Krstonošić, V.; Hadnađev, M. Influence of Oil Phase Concentration on Droplet Size Distribution and Stability of Oil-in-Water Emulsions. *Eur. J. Lipid Sci. Technol.* **2013**, *115* (3), 313–321.

(137) Mckee, M. G.; Wilkes, G. L.; Colby, R. H.; Long, T. E. Correlations of Solution Rheology with Electrospun Fiber Formation of Linear and Branched Polyesters. *Macromolecules* **2004**, *37* (5), 1760–1767.

(138) Palangetic, L.; Reddy, N. K.; Srinivasan, S.; Cohen, R. E.; McKinley, G. H.; Clasen, C. Dispersity and Spinnability: Why Highly Polydisperse Polymer Solutions Are Desirable for Electrospinning. *Polymer (Guildf).* **2014**, *55* (19), 4920–4931.

(139) Rošic, R.; Pelipenko, J.; Kocbek, P.; Baumgartner, S.; Bešter-Rogač, M.; Kristl, J. The Role of Rheology of Polymer Solutions in Predicting Nanofiber Formation by Electrospinning. *Eur. Polym. J.* **2012**, *48* (8), 1374–1384.

(140) Bordi, F.; Colby, R. H.; Cametti, C.; De Lorenzo, L.; Gili, T. Electrical Conductivity of Polyelectrolyte Solutions in the Semidilute and Concentrated Regime: The Role of Counterion Condensation. *J. Phys. Chem. B* **2002**, *106* (27), 6887–6893.

(141) Kriegel, C.; Arecchi, A.; Arrechi, A.; Kit, K.; McClements, D. J.; Weiss, J. Fabrication, Functionalization, and Application of Electrospun Biopolymer Nanofibers. *Crit. Rev. Food Sci. Nutr.* **2008**, *48* (8), 775–797.

(142) Morrison, F. . *Understanding Rheology*; Gubbins, K. F., Barteau, M. A., Lauffenburger, D. A., Morari, M., Ray, W. H., Russel, W. B., Tirrell, M. V., Eds.; Eds.: Oxford University Press: New York, 2001.

(143) Thompson, C. J.; Chase, G. G.; Yarin, A. L.; Reneker, D. H. Effects of Parameters on Nanofiber Diameter Determined from Electrospinning Model. *Polymer (Guildf).* **2007**, *48* (23), 6913–6922.

(144) Peyton, S. R.; Putnam, A. J. Extracellular Matrix Rigidity Governs Smooth Muscle Cell Motility in a Biphasic Fashion. *J. Cell. Physiol.* **2005**, *209* (July 2004), 198–209.

(145) Marklein, R. a.; Burdick, J. a. Spatially Controlled Hydrogel Mechanics to Modulate Stem Cell Interactions. *Soft Matter* **2010**, *6* (August 2009), 136.

(146) Peyton, S. R.; Kim, P. D.; Ghajar, C. M.; Seliktar, D.; Putnam, A. J. The Effects of Matrix Stiffness and RhoA on the Phenotypic Plasticity of Smooth Muscle Cells in a 3-D Biosynthetic Hydrogel System. *Biomaterials* **2008**, *29*, 2597–2607.

(147) Mahadik, B. P.; Wheeler, T. D.; Skertich, L. J.; Kenis, P. J.; Harley, B. C. Microfluidic Generation of Gradient Hydrogels to Modulate Hematopoietic Stem Cell Culture Environment. *Adv. Healthc. Mater.* **2014**, *3* (3), 449–458.

(148) Lee, J.; Li, M.; Milwid, J.; Dunham, J.; Vinegoni, C.; Gorbatov, R.; Iwamoto, Y.; Wang, F.; Shen, K.; Hatfieeld, K.; et al. Implantable Microenvironments to Attract Hematopoietic Stem / Cancer Cells. *Proc. Natl. Acad. Sci.* **2012**, *109* (48), 19638–19643.

(149) Torisawa, Y.-S.; Spina, C. S.; Mammoto, T.; Mammoto, A.; Weaver, J. C.; Tat, T.; Collins, J. J.; Ingber, D. E. Bone Marrow-on-a-Chip Replicates Hematopoietic Niche Physiology in Vitro. *Nat. Methods* **2014**, *11* (6), 663–669.

(150) Nicholsa, J. E.; Cortiellab, J.; Leee, J.; Nilesa, J. A.; Cuddihy, M.; Wangg, S.; Cantua, A.; Mlcakb, R.; Valdiviaa, E.; Yancy, R.; et al. In Vitro Analog of Human Bone Marrow from 3D Scaffolds with Biomimetic Inverted Colloidal Crystal Geometry. *Biomaterials* **2010**, *30* (6), 1071–1079.

(151) Scotti, C.; Piccinini, E.; Takizawa, H.; Todorov, A.; Bourgine, P.; Papadimitropoulos, A.; Barbero, A.; Manz, M. G.; Martin, I. Engineering of a Functional Bone Organ through Endochondral Ossification. *Proc. Natl. Acad. Sci. U. S. A.* **2013**, *110* (10), 3997–4002.

(152) Gilbert, P.; Havenstrite, K.; Magnusson, K.; Sacco, A.; Leonardi, N.; Kraft, P.; Nguyen, N.; Thrun, S.; Lutolf, M.; Blau, H. Substrate Elasticity Regulates Skeletal Muscle Stem Cell Self- Renewal in Culture. *Science (80-.).* **2011**, *329* (5995), 1078–1081.

(153) Vande Berg, B. C.; Malghem, J.; Lecouvet, F. E.; Maldague, B. Magnetic Resonance Imaging of Normal Bone Marrow. *Eur. Radiol.* **1998**, *8*, 1327–1334.

(154) Parfitt, A.; Mathews, C.; Villanueva, A.; Kleerekoper, M. Relationships between Surface , Volume , and Thickness of Iliac Trabecular Bone in Aging and in Osteoporosis. *J. Clin. Invest.* **1983**, *72*, 1396–1409.

(155) Gimble, J. M.; Robinson, C. E.; Wu, X.; Kelly, K. a. The Function of Adipocytes in the Bone Marrow Stroma: An Update. *Bone* **1996**, *19* (5), 421–428.

(156) Miyanishi, K.; Yamamoto, T.; Irisa, T.; Yamashita, a.; Jingushi, S.; Noguchi, Y.; Iwamoto, Y. Bone Marrow Fat Cell Enlargement and a Rise in Intraosseous Pressure in Steroid-Treated Rabbits with Osteonecrosis. *Bone* **2002**, *30* (1), 185–190.

(157) Bloomfield, S. a. Disuse Osteopenia. *Curr. Osteoporos. Rep.* **2010**, *8* (2), 91–97.

(158) Gurkan, U. A.; Akkus, O. The Mechanical Environment of Bone Marrow: A Review. *Ann. Biomed. Eng.* **2008**, *36* (12), 1978–1991.

(159) Zhang, P.; Su, M.; Liu, Y.; Hsu, A.; Yokota, H. Knee Loading Dynamically Alters Intramedullary Pressure in Mouse Femora. *Bone* **2007**, *40* (2), 538–543.

(160) Lynch, M. E.; Brooks, D.; Mohanan, S.; Lee, M. J.; Polamraju, P.; Dent, K.; Bonassar, L. J.; Van Der Meulen, M. C. H.; Fischbach, C. In Vivo Tibial Compression Decreases Osteolysis and Tumor Formation in a Human Metastatic Breast Cancer Model. *J. Bone Miner. Res.* **2013**, *28* (11), 2357–2367.

(161) Hosokawa, A.; Otani, T. Ultrasonic Wave Propagation in Bovine Cancellous Bone. *J. Acoust. Soc. Am.* **1997**, *101* (1), 558–562.

(162) Morgan, E. F.; Bayraktar, H. H.; Keaveny, T. M. Trabecular Bone Modulus–density Relationships Depend on Anatomic Site. *J. Biomech.* **2003**, *36* (7), 897–904.

(163) Meurens, F.; Summerfield, A.; Nauwynck, H.; Saif, L.; Gerdts, V. The Pig: A Model for Human Infectious Diseases. *Trends Microbiol.* **2012**, *20* (1), 50–57.

(164) Sullivan, T. P.; Eaglstein, W. H.; Davis, S. C.; Mertz, P. The Pig as a Model for Human Wound Healing. *Wound Repair Regen.* **2001**, *9* (2), 66–76.

(165) Peyton, S. R.; Kalcioglu, Z. I.; Cohen, J. C.; Runkle, A. P.; Van Vliet, K. J.; Lauffenburger, D. A.; Griffith, L. G. Marrow-Derived Stem Cell Motility in 3D Synthetic Scaffold Is Governed by Geometry along with Adhesivity and Stiffness. *Biotechnol. Bioeng.* **2011**, *108* (5), 1181–1193.

(166) Petrakis, N. L. Temperature of Human Bone Marrow. *J. Appl. Physiol.* **1952**, *4* (7), 549–553.

(167) Winer, J.; Janmey, P. a.; McCormick, M.; Funaki, M. Bone Marrow-Derived Human Mesenchymal Stem Cells Become Quiescent on Soft Substrates but Remain Responsive to the Chemical or Mechanical Stimuli. *Tissue Eng. Part A* **2009**, *15* (1), 147–154.

(168) Booth, A. J.; Hadley, R.; Cornett, A. M.; Dreffs, A. a.; Matthes, S. a.; Tsui, J. L.; Weiss, K.; Horowitz, J. C.; Fiore, V. F.; Barker, T. H.; et al. Acellular Normal and Fibrotic Human Lung Matrices as a Culture System for in Vitro Investigation. *Am. J. Respir. Crit. Care Med.* **2012**, *186*, 866–876.

(169) Melo, E.; Cárdenes, N.; Garreta, E.; Luque, T.; Rojas, M.; Navajas, D.; Farré, R. Inhomogeneity of Local Stiffness in the Extracellular Matrix Scaffold of Fibrotic Mouse Lungs. *J. Mech. Behav. Biomed. Mater.* **2014**, *37*, 186–195.

(170) Lai-Fook, S. J.; Hyatt, R. E. Effects of Age on Elastic Moduli of Human Lungs. *J. Appl. Physiol.* **2000**, *89* (1), 163–168.

(171) Rashid, B.; Destrade, M.; Gilchrist, M. D. Influence of Preservation Temperature on the Measured Mechanical Properties of Brain Tissue. *J. Biomech.* **2013**, *46*, 1276–1281.

(172) Miller, K.; Chinzei, K.; Orssengo, G.; Bednarz, P. Mechanical Properties of Brain Tissue in-Vivo : Experiment and Computer Simulation. **2000**, *33*, 1369–1376.

(173) Chatelin, S.; Constantinesco, A.; Willinger, R. Fifty Years of Brain Tissue Mechanical Testing: From in Vitro to in Vivo Investigations. *Biorheology* **2010**, *47* (5-6), 255–276.

(174) Banerjee, I.; Pangule, R. C.; Kane, R. S. Antifouling Coatings: Recent Developments in the Design of Surfaces That Prevent Fouling by Proteins, Bacteria, and Marine Organisms. *Adv. Mater.* **2011**, *23* (6), 690–718.

(175) Krishnan, S.; Weinman, C. J.; Ober, C. K. Advances in Polymers for Anti-Biofouling Surfaces. *J. Mater. Chem.* **2008**, *18* (29), 3405.

(176) Herrwerth, S.; Eck, W.; Reinhardt, S.; Grunze, M. Factors That Determine the Protein Resistance of Oligoether Self-Assembled Monolayers - Internal Hydrophilicity, Terminal Hydrophilicity, and Lateral Packing Density. *J. Am. Chem. Soc.* **2003**, *125* (31), 9359–9366.

(177) Hucknall, A.; Rangarajan, S.; Chilkoti, A. In Pursuit of Zero: Polymer Brushes That Resist the Adsorption of Proteins. *Adv. Mater.* **2009**, *21* (23), 2441–2446.

(178) Tegoulia, V. a.; Rao, W.; Kalambur, A. T.; Rabolt, J. F.; Cooper, S. L. Surface Properties, Fibrinogen Adsorption, and Cellular Interactions of a Novel Phosphorylcholine-Containing Self-Assembled Monolayer on Gold. *Langmuir* **2001**, *17* (14), 4396–4404.

(179) Kuang, J.; Messersmith, P. B. Universal Surface-Initiated Polymerization of Antifouling Zwitterionic Brushes Using a Mussel-Mimetic Peptide Initiator. *Langmuir* **2012**, *28* (18), 7258–7266.

(180) Gong, J. P. Why Are Double Network Hydrogels so Tough? *Soft Matter* **2010**, *6* (12), 2583.

(181) Haque, M. A.; Kurokawa, T.; Gong, J. P. Super Tough Double Network Hydrogels and Their Application as Biomaterials. *Polymer (Guildf).* **2012**, *53* (9), 1805–1822.

(182) Kolewe, K.; Peyton, S. R.; Schiffman, J. D. Fewer Bacteria Adhere to Softer Hydrogels. *ACS Appl. Mater. Interfaces* **2015**, *7* (35), 19562–19569.

(183) Liu, V.; Bhatia, S. Three-Dimensional Photopatterning of Hydrogels Containing Living Cells. *Biomed. Microdevices* **2002**, 257–266.

(184) Bhuchar, N.; Deng, Z.; Ishihara, K.; Narain, R. Detailed Study of the Reversible Addition–fragmentation Chain Transfer Polymerization and Co-Polymerization of 2-Methacryloyloxyethyl Phosphorylcholine. *Polym. Chem.* **2011**, *2* (3), 632.

(185) Chang, C.-C.; Kolewe, K. W.; Li, Y.; Kosif, I.; Freeman, B. D.; Carter, K. R.; Schiffman, J. D.; Emrick, T. Underwater Superoleophobic Surfaces Prepared from Polymer Zwitterion/Dopamine Composite Coatings. *Adv. Mater. Interfaces* **2016**, n/a – n/a.

(186) Lynge, M. E.; van der Westen, R.; Postma, A.; Städler, B. PDA39-Polydopamine—a Nature-Inspired Polymer Coating for Biomedical Science. *Nanoscale* **2011**, *3* (12), 4916.

(187) Chohan, Z. H.; Khan, K. M.; Supuran, C. T. Synthesis of Antibacterial and Antifungal cobalt(II), copper(II), nickel(II) and zinc(II) Complexes with Bis-(1,1'-disubstituted Ferrocenyl)thiocarbohydrazone and Bis-(1,1'-disubstituted Ferrocenyl)carbohydrazone. *Appl. Organomet. Chem.* **2004**, *18* (7), 305–310.

(188) Mallick, S.; Sharma, S.; Banerjee, M.; Ghosh, S. S.; Chattopadhyay, A.; Paul, A. Iodine-Stabilized Cu Nanoparticle Chitosan Composite for Antibacterial Applications. *ACS Appl. Mater. Interfaces* **2012**, *4* (3), 1313–1323.

(189) Zhao, L.; Mitomo, H.; Zhai, M.; Yoshii, F.; Nagasawa, N.; Kume, T. Synthesis of Antibacterial PVA/CM-Chitosan Blend Hydrogels with Electron Beam Irradiation. *Carbohydr. Polym.* **2003**, *53* (4), 439–446.

(190) Jia, B.; Mei, Y.; Cheng, L.; Zhou, J.; Zhang, L. Preparation of Copper Nanoparticles Coated Cellulose Films with Antibacterial Properties through One-Step Reduction. *ACS Appl. Mater. Interfaces* **2012**, *4* (6), 2897–2902.

(191) Akbarian, M.; Olya, M. E.; Ataeefard, M.; Mahdavian, M. The Influence of Nanosilver on Thermal and Antibacterial Properties of a 2 K Waterborne Polyurethane Coating. *Prog. Org. Coatings* **2012**, *75* (4), 344–348.

(192) Kumar, A.; Vemula, P. K.; Ajayan, P. M.; John, G. Silver-Nanoparticle-Embedded Antimicrobial Paints Based on Vegetable Oil. *Nat. Mater.* **2008**, *7* (3), 236–241.

(193) Wiegand, I.; Hilpert, K.; Hancock, R. E. W. Agar and Broth Dilution Methods to Determine the Minimal Inhibitory Concentration (MIC) of Antimicrobial Substances. *Nat. Protoc.* **2008**, *3* (2), 163–175.